Electronic Activation and Tuning of Redox-Active Ligand Orbitals

Benjamin Keith Leipzig

A dissertation submitted in partial fulfillment of the requirements for the degree of

Doctor of Philosophy

University of Washington

2017

Reading Committee:
Julie A. Kovacs, Chair
Daniel R. Gamelin
Brandi M. Cossairt

Program Authorized to Offer Degree: Department of Chemistry

University of Washington

Abstract

Electronic Activation and Tuning of Redox-Active Ligand Orbitals

Benjamin Keith Leipzig

Chairperson of the Supervisory Committee:
Professor Julie A. Kovacs
Department of Chemistry

This dissertation focuses upon the synthesis, characterization and reactivity of thiolate-ligated α-(imino)-*N*-heterocycle complexes. Chapter 1 provides an introduction to cysteinate ligated metalloenzymes and synthetic model systems containing redox-active ligands. Chapter 2 discusses the synthesis and characterization of three thiolate ligated iron (II) α-(imino)-*N*-heterocycle complexes displaying unique spectroscopic features. Chapter 3 highlights the unique activation of the α-(imino)-*N*-heterocycles due to the coordinated thiolate through the role of electrochemistry, sulfur K-edge X-ray absorption spectroscopy and computations. Chapter 4 exhibits the role of the geometry around the metal center and the effect of the thiolate through a cobalt, manganese and thioether derivatives. Chapter 5 presents a unique nucleophilic attack of a thiolate forming a thiazolidine ring structure. The results described will highlight the ability to fine tune these redox-active orbitals which have a large role in multi-electron base metal catalysis.

Table of Contents

List of Figures

List of Tables

Page

List of Schemes

Page

Glossary

δ	Isomer shift
Å	Ångström
Ac	Acetate
atm	Atomosphere
BIP	Bis(imino)pyridine
Boc	*tert*-butyloxycarbonyl (protecting group)
Bu	Butyl
CDO	Cysteine Dioxygenase
cm^{-1}	Wavenumbers
Co	Cobalt
Cys	Cysteine
DMF	Dimethylformamide
DMSO	Dimethyl sulfoxide
DFT	Density functional theory
e^-	Electron
EFG	Electric field gradient
EPR	Electron paramagnetic resonance
ΔE_Q	Quadrupole splitting
ESI-MS	Electrospray ionization mass spectrometry
Et	Ethyl
Et_2O	Diethyl Ether

EtOH	Ethanol
eV	Electron volts
EXAFS	Extended X-ray absorption fine structure
Fc	Ferrocene
Fc^+	Ferrocenium
$[Fc]PF_6$	Ferrocenium hexafluorophosphate
g	Gauss
HOMO	Highest occupied molecular orbital
Hz	Hertz
IR	Infrared spectroscopy
LAH	Lithium aluminum hydride
LLCT	Ligand-to-ligand charge transfer
LMCT	Ligand-to-metal charge transfer
LUMO	Lowest unoccupied molecular orbital
MeCN	Acetonitrile
MeOH	Methanol
MLCT	Metal-to-ligand charge transfer
Ms	Mesylate
NADP	Nicotinamide adenine dinucleotide phosphate
NMR	Nuclear magnetic resonance
O_2^-	Superoxide
PDB	Protein data bank
Ph	Phenyl group

ppm	parts per million
RDS	Rate determining step
S	Sulfur
SOD	Superoxide Dismutase
SOR	Superoxide Reductase
TD-DFT	Time dependent density functional theory
TLC	Thin layer chromatography
Tren	$N(EtNH_2)_3$
Ts	Tosylate
UV-Vis	Ultraviolet-visible
XANES	X-ray absorption near edge structure
XAS	X-ray absorption spectroscopy

List of Numbed Complexes

1 3-methyl-3-oxetanemethanol, $C_5H_{10}O_2$

2 2-bromomethyl-2-methyl-propane-1,3-diol, $C_5H_{11}BrO_2$

3 2-benzylsulfanyl methyl-2-methyl-propane-1,3-diol, $C_{12}H_{18}O_2S$

4 (3-methanesulfonyl-2-methanesulfonylmethyl-2-methyl-propylsulfanylmethyl)-benzene , $C_{14}H_{22}O_6S_3$

5 (3-azido-2azidomethyl-2-methyl-propylsulfanylmethyl)-benzene, $C_{12}H_{16}N_6S$

6 2-benzylsulfanylmethyl-2-methyl-propane-1,3-diamine, $C_{12}H_{20}N_2S$

7 2-benzylsulfanylmethyl-2-methyl-propane-1,3-(*tert*-Butyloxycarbonyl) diamine, $C_{22}H_{36}N_2O_4S$

8 2-thiomethyl-2-methyl-propane-1,3-(*tert*-Butyloxycarbonyl) diamine, $C_{15}H_{30}N_2O_4S$

9 2-thiomethyl-2-methyl-propane-1,3-diamine dihydrogenchloride, $C_5H_{16}Cl_2N_2S$

10 $[(Fe^{II}(Tame\text{-}N_2SPy_2))_2](PF_6)_2$, $C_{34}H_{38}F_{12}Fe_2N_8P_2S_2$

10-CN $(Fe^{II}(Tame\text{-}N_2SPy_2)CN$, $C_{18}H_{19}FeN_4S_1$

11 $[(Fe^{II}(Tame\text{-}N_2SQu_2))_2]\ (PF_6)_2$, $C_{50}H_{46}F_{12}Fe_2N_8P_2S_2$

11-BPh_4 $[(Fe^{II}(Tame\text{-}N_2SQu_2))_2](BPh_4)_2$, $C_{96}H_{86}B_2Fe_2N_8S_2$

12 $[(Fe^{II}(Tame\text{-}N_2SImid(Me)_2))_2](PF_6)_2$, $C_{30}H_{43}F_{12}Fe_2N_{12}P_2S_2$

12^{ox} $[(Fe^{III}(Tame\text{-}N_2SIm_2))_2](PF_6)_4$, $C_{30}H_{43}F_{24}Fe_2N_{12}P_4S_2$

13 $[(Co^{II}(Tame\text{-}N_2SIm_2))_2](PF_6)_2$, $C_{30}H_{43}F_{12}Co_2N_{12}P_2S_2$

13^{ox} $[(Co^{III}(Tame\text{-}N_2SIm_2))_2](PF_6)_4$, $C_{30}H_{43}F_{24}Co_2N_{12}P_4S_2$

14 $[Fe^{II}(tame\text{-}(N_2S^{Bz}(^{Me}Im)_2(MeCN))]\ (PF_6)_2$, $C_{22}H_{28}F_{12}FeN_6P_2S$

15 $[Mn^{II}(tame\text{-}(N_2S(^{Me}Im)_2Cl]\ (PF_6)$, $C_{15}H_{22}ClF_6MnN_6PS$

16 [$Fe^{II}N_3$thiazolidineCl]Cl, $C_{25}H_{35}Cl_2FeN_3S$

17 [($Fe^{II}N_3$thiazolidineCl)$_2$Cl]OTf, $C_{51}H_{70}Cl_3F_3FeN_6O_3S_3$

Chapter Contributions

Much of the work detailed in the following chapters would not have been possible without the valuable efforts of a number of collaborators. Their individual contributions are gratefully acknowledged below.

Chapter 2. Roslyn Theisen, Sarah E. Flowers and Werner Kaminsky for the crystallographic characterization of **10-12**.

Chapter 3. Julian Rees for the detailed computational results for complexes **10-12** and performing the Mössbauer spectroscopy. Alexander Nyrov and Professor Serena DeBeer for performing the Sulfur K-edge X-ray spectroscopy experiments at the ESRF beamline. Maike Blakely and Werner Kaminsky for the crystallographic characterization of **12^{ox}**.

Chapter 4. Sarah E. Flowers, Maike Blakely and Werner Kaminsky for the crystallographic characterization of **13-15** and **13^{ox}.**

Chapter 5. Michael Coggins and Werner Kaminsky for the crystallographic charterization of **16** and **17**.

Acknowledgments

First I would like to thank my graduate advisor Professor Julie Kovacs for all the support. Graduate school had many ups and downs but throughout my time at the University of Washington she has always been there to provide both the scientific and emotional support that was necessary to making me both the scientist and person I am. I am forever grateful for her advice and hopefully I have been a good role model to the next wave of Kovacs students in her laboratory.

I have always admired the ability of my committee members to take the time to discuss my chemistry, both in and out of my examinations. These Professors have provided an excellent source of inspiration in becoming a better chemist. Professors Gamelin and Cossairt have always aided me in understanding the complexities of inorganic chemistry during my examinations. Professor Stenkamp was a wonderful GSR who took the time to read my written portions and provide feedback, both in my writing and presentations. Professors Mayer, Sasaki and Boydston all took the time to sit in and encourage me during my early examinations and taught me to think critically about chemistry. I would be remiss not to acknowledge Professor Heinekey who has made the inorganic division such a wonderful place to work. I am also extremely grateful for the support from Professor Goldberg, who took time to help me, more so than she may realize, through some difficult times.

I grew as a scientist through my interactions with my Kovacs group mates. I could not have understood half of what I know without the guidance of Michael Coggins, who was as supportive of a mentor as I could have asked for. Julian Rees and Audra Johansen were my crew for the majority of my time in grad school and I cannot fathom what life or graduate school would be like without their presence. The newer members of the lab are full of excitement at the

chemistry currently underway. Maike Blakely, Maks Dedusko, Penny "Dyme" Poon (King Bob), Alex Downing and Dylan Rogers will undoubtedly carry the lab forward into exciting new frontiers of bioinorganic chemistry.

My chemistry would not be complete without the support of the University of Washington inorganic department. Some of these people have become great friends to this day and I cannot picture a world without them in my life. To the "Diner Club"[1]: Tyler Stevens, Sophia Cherry, Mike Cherry, Wilson Bailey, Cecily Ferguson, Jon Goldberg, Karena Smoll, Travis Lekich and Louise Guard, thank you! I would not have gotten through the first couple of exams without the support of my ex-wife, Carolyn Valdez, who helped shaped my understanding of what a great chemist consists of.

My life has been so enjoyable while at the University of Washington thanks to the support of my wonderful girlfriend, Kim Quigley, who has been so patient and supportive throughout this final chapter of graduate school. Words cannot express how much you have helped me get through this, thank you!

Finally, I would not be the person I am without the support of my family, who have been the best role models for me growing up and even to this day. To my sister, Mom and Dad, thank you for all the support. I don't think this journey would have been this special without you.

[1] Bailey, W. D. Late Transition-Metal Complexes Supported by Pincer Ligands: Applications in Partial Oxidation Catalysis. University of Washington, Seattle, 2016

Dedication

To my family

Chapter 1.

Introduction.

Metals in Biological Systems

Proteins are essential to the function of living organisms and perform an array of diverse processes. These macromolecules are constructed of amino acids and predominately composed of carbon, hydrogen, nitrogen and oxygen. However, the function, or structural stability, of these proteins often require cofactors. A common type of cofactor, which makes up over a third of all crystallographically characterized proteins found in the Royal Society's protein data bank (PBD), is a transition metal, signifying the importance of these elements in the foundation of life. These metals typically perform functions that are not as accessible for non-metal elements, such as providing structural integrity, aiding in electron transport or transporting small substrates.[1] An additional role of proteins is to catalyze reactions. The metal cofactor can afford access to multiple oxidation states, differing coordination numbers and geometries. This contrasts with the main group elements, which have limited oxidation states and coordination numbers available. One goal of bioinorganic chemists is to understand the properties that make these enzymes so efficient, which typically starts at the primary coordination sphere around the metal cofactor.[2] While high-resolution crystal structures have aided in the understanding structural identity of the active site, the reactivity and intermediates that form during the activity of the enzymes have largely remained a mystery.

However, high-resolution crystal structures allow for the targeted synthesis of structural models to comprehend the subtle importance of specific amino acids. These biomimetic models can be designed to have very similar coordination environments around a metal. With these models, bond lengths and spectroscopic features can be compared to the native metalloenzymes to help understand the reactivity of these important proteins.[3] Unlike the native enzymes, these models can strictly focus on the metal itself without the need for the overwhelming size of the

other amino acid residues on the protein backbone. Additionally, they can help focus on a specific active-site, as there are metalloenzymes that contain multiple metal cofactors, each with unique function. This can cause data from metal specific spectroscopic techniques to be convoluted. These model systems afford an avenue to perform low-temperature experiments to attempt to isolate key intermediates unobservable in the native enzyme. At times, these metastable intermediates in model systems can be crystalized to give structural information that is far from trivial to obtain from native enzymes. A significant example of this was the observation of a μ-η^2:η^2 peroxo bridging mode in a copper model complex that mirrored the bridging mode for copper hemocyanin.[4,5] Understanding the relationship between structure and function is paramount to the biomimetic community.

Cysteinates and Effects of the Thiolate

Many of the metals that are found in metalloenzymes were incorporated due to the abundance found in the earth's core. To bind these versatile elements, proteins typically coordinate through amino acid side chains, the amide backbone, or porphyrin and small molecule cofactors. Most metalloenzymes have a primary coordination sphere composed of nitrogen and oxygen atoms.[1,2] However cysteine (Cys) is one amino acid residue that can coordinate through a deprotonated sulfur of the side chain to have a thiolate ligated to the metal cofactor. Cysteinate ligation can be found in metalloenzymes with a variety of first row transistion metals including iron (Fe), cobalt (Co), nickel, copper and zinc.[3,6]

Unlike the first row main group atoms like oxygen and nitrogen, sulfur imparts quite different properties when coordinated to first row transition metals. Cysteinates form highly covalent bonds to first row transition metals, which aids in modulating redox potentials to impact

electron transfer and strong bond activation. Many active sites have the cysteinate *trans* to the open site where small molecule binding and/or activation occurs.[3,6] The strong σ- and π-donating thiolate has a strong *trans* effect and can promote requisite substrate release. The covalency of a coordinated cysteinate can also impact the spin state of metal ions due to the large nephelauxetic effect favoring lower spin states.[7,8]

Cysteinate Ligated Iron Metalloenzymes

Iron (Fe) is found in abundance in our Earth's core and unsurprisingly is the most commonly found transition metal in metalloenzymes. Fe-sulfur bonds are found throughout metalloproteins from Fe-S clusters to Fe-heme and Fe-non-heme enzymes.[1] Fe-heme enzymes are attractive to study due to our ability to probe them spectroscopically because of their distinct $\pi \rightarrow \pi^*$ soret band; one of more well studied enzymes featuring cysteine ligation is cytochrome P450.[9] While this enzyme has seen a wealth of publications, there is less known about non-heme cysteinate-ligated Fe metalloenzymes.[9] These enzymes, including superoxide reductase (SOR), cysteine dioxygenase (CDO), nitrile hydratase, penicillin *N* synthase and peptide deformylases have unique ligation to the metal cofactor that differs from the common "2-his-1-carboxylate" triad found in mononuclear iron enzymes.[3,6] In each case cysteinate ligation heavily impacts the reactivity of these metalloenzymes.

Cytochrome P450

Cytochrome P450 is primarily responsible for hydroxylating unactivated, strong C-H bonds. The potent oxidant required to perform these difficult transformations is formed through the reduction of O_2.[9,10] The primary coordination sphere is important for the enzyme's ability to activate O_2 and consists of the Fe metal center in a square pyramidal geometry with the basal plane consisting of the four nitrogens of a porphyrin ring (**Figure 1.01**).[11] The enzyme has one conserved cysteinate residue in proximity to the heme cofactor that is essential to the reactivity, and binds in the axial position. This affects the frontier orbitals giving rise to the signature Soret band at 450 nm.

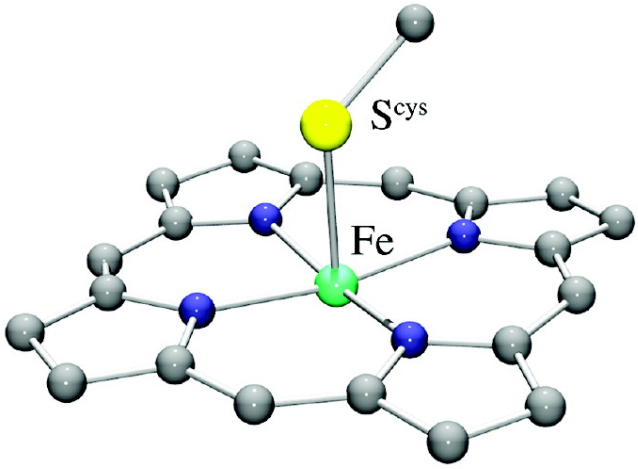

Figure 1.01: Active site of cytochrome P450 containing a basal plane formed from a porphyrin cofactor and an axial cysteinate.[6] N atoms of porphyrin are in blue, Fe in green, S in yellow while C atoms are in gray.

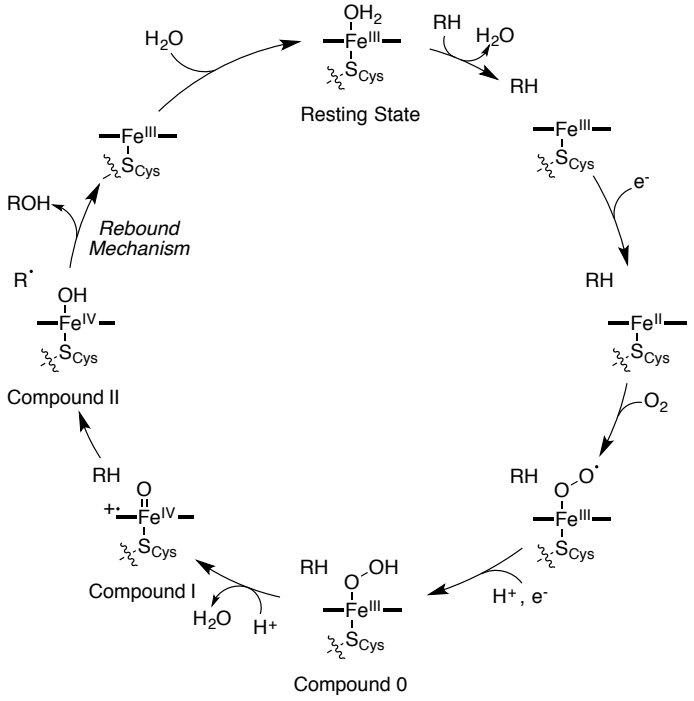

Figure 1.02: Reactivity cycle of cytochrome P450.[10]

The general reactivity of cytochrome P450 with O_2 has been established based on spectroscopic observation of significant intermediates. The enzyme has an Fe(III) resting oxidation state and reacts upon the hydrocarbon substrate entering the binding pocket (**Figure 1.02**). A reduction, typically from NAD(P)H, occurs after geometric changes that induce a spin state change from low- to high-spin Fe(III).[10] The reduction potentials are modulated and lower than expected due to the coordinated anionic thiolate. The reduced ferrous complex is then able to coordinate and reduce O_2 forming a transient Fe^{III}-superoxo species. Reduction by a flavin cofactor and protonation yields an Fe^{III}-hydroperoxo intermediate, known as compound 0. EPR measurments have identified this species as low-spin, and in the mutant enzyme, resonance Raman IR spectroscopy has shown vibrational data consistent with a bound peroxo species due to observed $\nu_{O\text{-}O}$ and $\nu_{Fe\text{-}O}$ stretch found at 799 cm^{-1} and 559 cm^{-1}.[12] This was confirmed to be a peroxo intermediate due to the isotopomeric mixture experiment observing the change in the O-

O stretch.[13] The weak O-O stretch suggests a significant influence of the axial cysteinate and the spin state on the strength of the O-O bond.

Compound 0 then undergoes heterolytic O-O bond cleavage by protonation of the distal oxygen, forming what is proposed to be the active oxidant compound I. Unlike other catalase O_2 activating heme enzymes that have a hydrophilic distal pocket to promote the protonation of the distal oxygen, cytochrome P450 enzymes have a very hydrophobic pocket.[14,15] The ability to protonate the distal oxygen and induce a heterolytic O-O bond cleavage is thus much weakened in this class of enzymes. Instead of this type of "pull" effect from a hydrogen bonding chain of residues around the distal oxygen, cytochrome P450 enzymes may aid the bond cleavage through a "push"[16] effect from the cysteinate *trans* to the peroxo unit.[17,18] The axial cysteinate can donate electron density in a π-type overlap with the iron metal orbitals. This density is then pushed into the peroxo σ^* orbital that overlaps in a π-interaction with specific metal orbitals.[19,20] Increased electron density in the σ^* orbital would then help cleave the O-O bond (**Figure 1.03**). Thus, covalency of the Fe-S bond is essential to the heterolytic O-O bond cleavage and formation of compound I.[21]

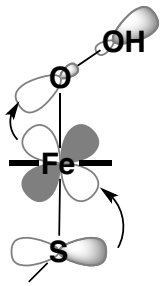

Figure 1.03: Schematic picture of the thiolate donating electron density through the iron cofactor and into the peroxide σ^* of compound 0.

The heterolytic cleavage of the O-O bond would suggest that compound I is an Fe^V-oxo species. However due to the cooperative effects of both cysteinate-Fe and π-delocalization

around the heme cofactor, this new intermediate is an Fe^{IV}-oxo with a ligand based radical ($(Por/S_{Cys}^{\bullet})Fe^{IV}=O$).[22,23] Recent work by Michael Green has established that significant ligand radical character is associated with the axial cysteinate.[24] This suggests that there is cooperativity between the organic redox reservoirs of the porphyrin ring and the axial cysteinate to produce this important reducing equivalent. The involvement of this organic based redox-reservoir in the mechanism of cytochrome P450 has inspired considerable development of synthetic 1st row transition metal complexes that contain a redox-active ligand, and will be discussed in detail later in this chapter.

Compound I is believed to be the active oxidant and the thiolate is postulated to increase the basicisity of the resulting $[(Por/S_{cys}^{\bullet})Fe^{IV}=O]$ allowing for H-atom abstraction.[25] The complete hydroxylation of the aliphatic substrate happens through the rebound mechanism. The H-atom abstraction step affords an Fe^{IV}-OH, known as compound II, and a radical based carbon on the substrate. The hydroxide and carbon radical will recombine to release the hydroxylated product and subsequent water coordination will afford the resting ferric state.[10] The axial cysteinate is proposed to impact many steps of this mechanism and synthesizing model systems to investigate this can help gain insight to the design and function of cytochrome P450.

Superoxide Reductases

While O_2 is essential to much of life on earth, its reduced species are strong oxidants that can negatively impact cells. High superoxide (O_2^-) concentration has been linked to a variety of diseases and detrimental conditions such as Parkinson's and Alzheimer's diseases, and cancers.[26] To combat this toxic small molecule oxidant, living organisms have enzymes that are capable of sequestering O_2^- into less harmful products. Most aerobic organisms contain superoxide

dismutase (SOD), which will affect the $1e^-$ disproportionation of O_2^- into the more benign O_2 and H_2O_2 (**Scheme 1.01**).[27] Both the reduction and oxidation of superoxide occurs at a single redox active metal cofactor active site consisting of either a non-heme Fe, Mn or Cu. Unique to the copper enzyme is a redox-inert zinc cofactor.[28]

Scheme 1.01: Disproportionation of O_2^- by SOD

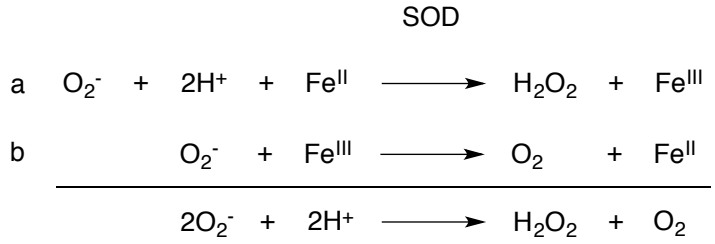

Scheme 1.02: Sequestering of O_2^- by SOR

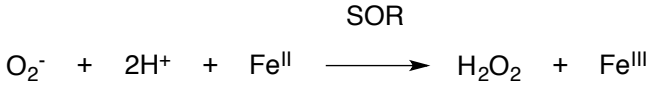

Anaerobic bacteria also have an enzyme that sequesters O_2^- but unlike in SOD it will not produce O_2. This enzyme known as superoxide reductase (SOR), will only perform one half of the reaction seen in SOD (**Scheme 1.02**).[29] This enzyme has a primary coordination sphere that is reminiscent of Cytochrome P450. It is known to contain a Fe metal cofactor constrained in a square pyramidal geometry (**Figure 1.04**). Four nitrogens from histidine residues makeup the basal plane and an axial cysteinate is *trans* to the open site.[3] The location of the active site by the surface of the enzyme may allow proton shuttles that are necessary for enzymatic reactivity.[29]

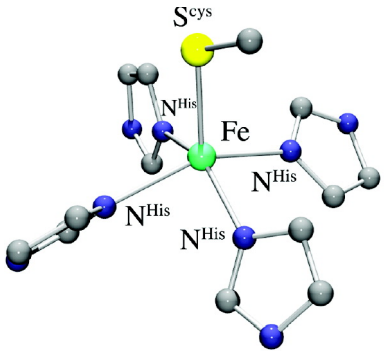

Figure 1.04: Active site of superoxide reductase consisting of a basal plane of four histidines and an axial thiolate. N atoms of histidines are in blue, Fe in green, S in yellow while C atoms are in gray.

The enzyme has a high-spin ferric resting state that coordinates a nearby glutamate to the open site, resulting in an octahedral geometry. This glutamate (glu^{14}), as well as a nearby lysine, are essential to the reactivity and could maintain a proton relay or guide the O_2^- substrate to the active site.[29] The reduction of the ferric species will release the glutamate and establish the five-coordinate high-spin ferrous active species. Coordination of O_2^- and oxidation of the ferrous metal center will generate a metastable high spin ferric species, T1 (**Figure 1.05**).[30]

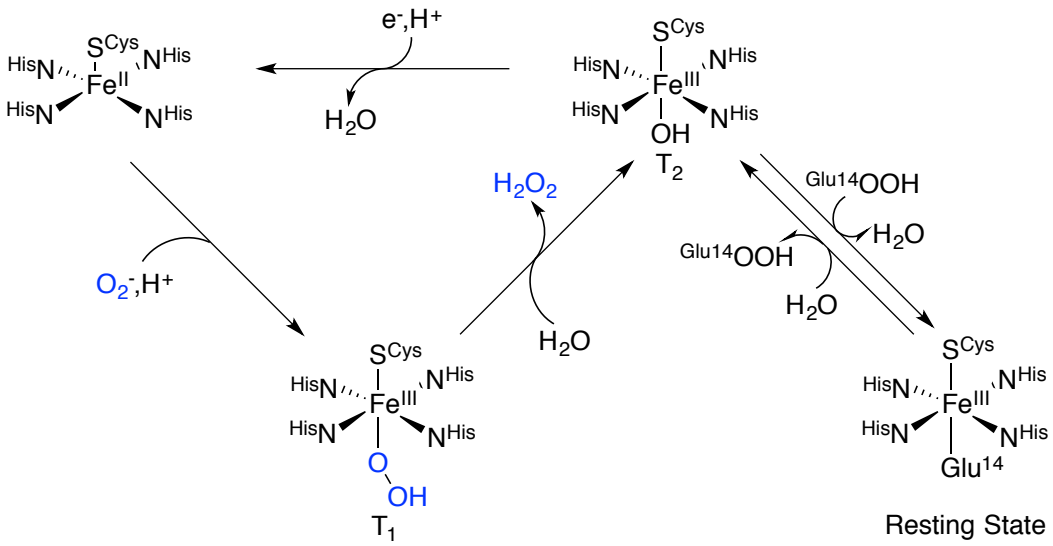

Figure 1.05: Proposed reaction cycle of superoxide reductase indicating two metastable species, T1 and T2.

A charge transfer band at 600 nm has been established as the $S_{cys} \rightarrow Fe$ charge transfer transition for the T_1 intermediate.[31] Resonance Raman probed vibrational parameters of this species with a mutant enzyme, using H_2O_2 as the oxidant. This species had a weak ν_{Fe-O} stretch at 438cm^{-1} but a strong ν_{O-O} stretch at 850 cm^{-1}, which were both isotopically sensitive when ^{18}O-labeled substrate was added.[32] At the time this species was tentatively assigned as an η^2-side-on peroxo species based on synthetic models. Larry Que had established that η^2-side-on peroxo complexes typically had weaker ν_{Fe-O} and favored high spin ferric states, while η^1-end-on peroxos favored low-spin states resulting in stronger ν_{Fe-O}.[33] However, the crystal structure of this intermediate definitively identified this species as an end-on hydroperoxo species.[34] It has been hypothesized that the strong *trans* effect of the axial cysteinate helps to weaken the Fe-O bond and promote product release.

This intermediate suggests that cytochrome P450 and SOR proceed through a structurally similar end-on ferric hydroperoxo. However, unlike the heme enzyme, SOR will not proceed through a high valent Fe=O. Instead of protonating the distal oxygen and favoring O-O cleavage, SOR will protonate the proximal oxygen resulting in the release of H_2O_2 and the cleavage of the Fe-O bond.[3,6] After release of H_2O_2, a new ferric species is observed and believed to be an Fe^{III}-hydroxide, known as T2. Reduction by NADPH will then regenerate the starting active ferrous state.[35] The axial cysteinate has been postulated to help promote the critical bond breaking steps of the related Fe^{III}-hydroperoxo intermediates in both enzymes, however this cleavage occurs at two different locations (**Figure 1.06**).

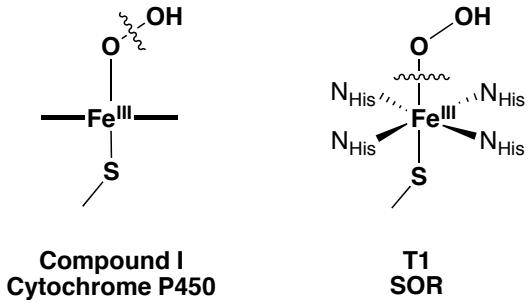

Figure 1.06: Location of the heterolytic bond cleavage after the similar ferric hydroperoxo intermediate in both cytochrome P450 (Left) and SOR (Right).

Biomimetic Modeling of Ferric Peroxides

As discussed above, a vast number of pentadentate amine scaffolds have been isolated and has been shown that there is significant differences between high spin metal complexes and low spin complexes. Low-spin systems typically have $\nu_{Fe\text{-}O}$ around 617-644 cm^{-1} and $\nu_{O\text{-}O}$ around 781-806 cm^{-1} (**Table 1.01**).[33,36,37] Conversely, high-spin complexes have $\nu_{Fe\text{-}O}$ around 470-495 cm^{-1} and $\nu_{O\text{-}O}$ around 817-827 cm^{-1} suggesting that SOR could modulate the strong O-O bond by maintaining a high spin iron metal center, favoring protonation of the proximal oxygen and subsequent release of H_2O_2.[38,39] The low-spin state of the ferric metal in the cytochrome P450 intermediates can promote O-O bond cleavage instead.

Table 1.01: Vibrational data of Fe(III)-peroxo intermediates in selected synthtetic model complexes and for some metastable intermediates of enzymes. Table adapted from Ref 33.

	$\nu_{Fe\text{-}O}$ (cm^{-1})	$\nu_{O\text{-}O}$ (cm^{-1})	Spin	ref
Py5-(OOH)	627	806	1/2	33
5-Br_2-N_4Py-(OOH)	641	795	1/2	33
5-$(MeO)_2N_4$Py-(OOH)	644	791	1/2	33
TPEN-OOH	617	796	1/2	36
$S^{Me2}N_4$Tren-OOH	562(DFT)	784	1/2	44
CytP450 compound I	553	792	1/2	12
N4Py-(OO)	495	827	5/2	33
EDTA-(OO)	459	816	5/2	39
BPPA-(OOH)	621	830	5/2	38
CyclamPrS-(OOH)	419	850	5/2	45
E47A SOR T1	438	850	5/2	32

However the axial cysteinate in both of these enzymes is critical and is potentially responsible for impacting the vibrational stretches. David Goldberg demonstrated that the incorporation of a thiolate will weaken the Fe-O bond of alkylperoxides. A tetradentate cyclam amine backbone formed the basal plane around the Fe metal center (**Figure 1.07**).[40] The incorporation of a *trans* thiolate decreases the $\nu_{Fe\text{-}O}$ by 90 cm^{-1} compared to other low-spin ferric alkylperoxides.[41] Methylating the backbone affords a spin state change from low-spin to high-spin and, as expected, the vibrational $\nu_{Fe\text{-}O}$ stretches decreased from 612 cm^{-1} to 584 cm^{-1} with the same change of *trans* triflate to an aryl thiolate.[42] These results indicate the importance of both the coordinated atoms and the spin state of the metal ion on the strength of the Fe-O bond.

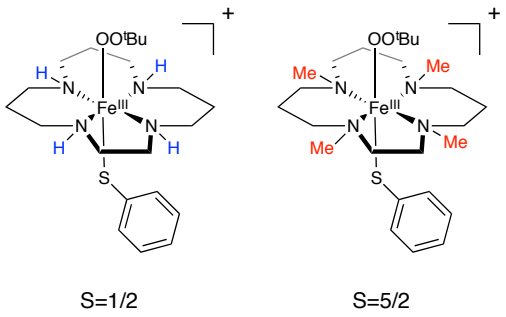

Figure 1.07: Spin states of two Tetradentate cyclam ferric alkylperoxos with an exogenous aryl thioalate in the axial position.

The Kovacs group has shown the importance of both the spin-state and the location of a coordinated thiolate on functional synthetic models of SOR. While Goldberg had N_4S ligation around the Fe metal, the thiolate was not tethered to the basal amine framework. Kovacs' first functional model maintained the N_4S coordination but the geometry was not similar to that seen in SOR.[43] The system, $[Fe^{II}(S^{Me2}N_4(tren)]^+$, coordinated in a trigonal bipyramidal geometry around the ferrous metal (**Figure 1.08** left). A key feature of the enzyme's active site, the *trans* cysteinate, was not replicated as in this model as the thiolate is *cis* to the open coordination site.

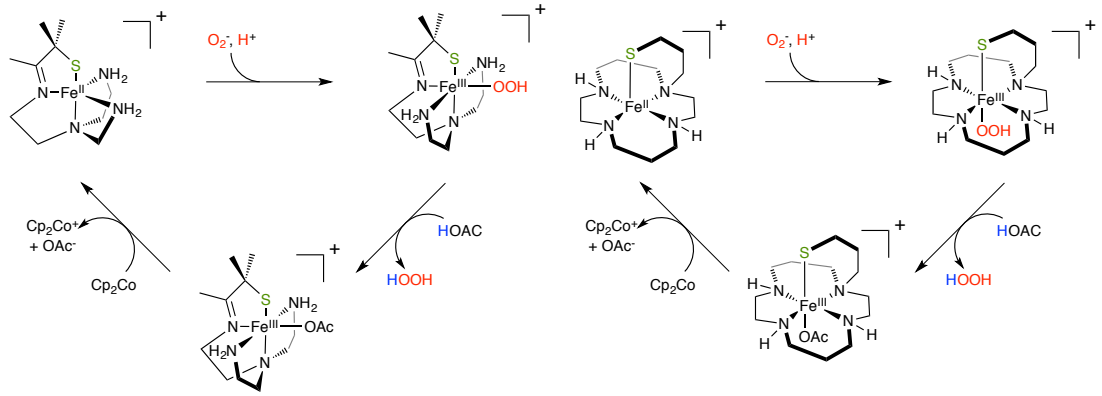

Figure 1.08: Synthetic models designed by Kovacs and coworkers containing a coordinated thiolate in both *cis* (left) and *trans* (right) to the open site. Both model the reactivity of SOR.

Even with these differences, superoxide will bind to and oxidize the ferrous metal center to form a metastable intermediate with a charge transfer band at 452 nm. This intermediate was identified to contain a ferric metal center based on the location of this sulfur to Fe charge transfer transition. An axial EPR signal with g-values indicating a low-spin ferric metal center and X-ray absorption data also confirmed this assignment.[44] This species was further identified as a Fe-hydroperoxo species due to the observation of a distal oxygen in the EXAFS spectrum, as well as vibrational data. FT-IR data indicated a Fermi resonance, due to coupling between two vibrations of similar energies, at 788 and 781 cm^{-1}. Addition of D_2O caused the Fermi resonance to collapse into a single peak at 784 cm^{-1}. This suggests that there is a peroxo binding mode due to the $\nu_{O\text{-}O}$ stretch in the IR spectrum. Isotopically labeling the oxygens results in a shift of this resonance of 31 cm^{-1} to 753 cm^{-1} as expected by Hooke's law.[44] The $\nu_{Fe\text{-}O}$ stretch was unobserved but calculated by DFT to be at 562 cm^{-1}. This weakened O-O bond is not without precedent and similar to the ferric hydroperoxo observed in compound 0, both of which contain a thiolate in the primary coordination sphere.[12]

Protonation of this species by acid will afford a 6-coordinate low-spin ferric complex with the coordinated conjugate base and the release of H_2O_2 modeling the second step of the

SOR mechanism. An outersphere reductant will regenerate the starting ferrous complex. Addition of another equivalent of potassium superoxide will result in the formation of the same metastable intermediate replicating the chemistry produced by SOR, even with different ferric spin states and geometry of the coordinated thiolate.

While $[Fe^{II}(S^{Me2}N_4(tren)]^+$ did not have a thiolate *trans* to the open site or a similar spin state of the ferric hydroperoxo species seen in SOR, Kovacs and coworkers synthesized a second model system to address these features. The cyclam basal plane was adapted to contain a single arm containing an aliphatic thiolate known as $[Fe^{II}$cyclamPrS$]^+$ (**Figure 1.08** right).[45] This afforded a square pyramidal N_4S geometry with the basal plane consisting of the four nitrogens and an apical thiolate consistent with the active site of SOR. Addition of superoxide results in the formation of a metastable species with a visible charge transfer band at 530 nm.

EPR spectroscopy has identified this species as a high-spin ferric complex. The vibrational data collected with resonance Raman spectroscopy suggests that, once again, a ferric-peroxo species is formed. The ν_{O-O} stretch is exceptionally high at 891 cm^{-1} while the ν_{Fe-O} stretch indicates a weak Fe-O bond at 419 cm^{-1}. This Fe-O bond is unusually weak but relates well to the vibrational data observed in SOR. Addition of an acid will produce H_2O_2 and a ferric complex with the coordinated conjugate base. Reduction can then reform the ferrous starting complex which can undergo another turnover. The difference in the vibrational data of these two thiolate ligated synthetic models suggests the importance of the both the geometry of the complex, the position of the coordinated thiolate, and the spin-state of the metal. Understanding the true effects of both of these factors would be more viable with a larger library of thiolate-ligated model complexes.

Redox-Active Ligands and Their Effect on Catalysis

Typically earth abundant, 1st row transition metals excel at sequential $1e^-$ redox chemistry but Nature has found a way to incorporate these metals to perform multiple electron redox transformations. Water oxidation and nitrogen reduction are two essential transformations that require multiple electrons. To accomplish these difficult transformations, enzymes have adopted active sites that contain multiple metal ions, expanding the number of redox states and making this chemistry viable.[1,2]

Cytochrome P450, however, undergoes the $4e^-$ reduction of O_2 at a mononuclear Fe-metal center.[9] An essential feature of the chemistry of cytochrome P450 is the ability of the porphyrin/cysteinate's redox reservoir to participate in the critical heterolytic O-O bond cleavage step. This cooperativity between the metal redox orbitals and the organic redox orbitals, so essential to the enzyme, has inspired considerable effort to characterize and understand synthetic systems with similar characteristics.[46]

Recently there has been a wealth of publications on the preparation of 1st row transition metal complexes containing redox-active ligands. Examples of these systems include salen,[47] dithiolenes,[48] *o*-phenylenediamines,[49] bis(imino)pyridine[50] and α-(imino)pyridines[51] (**Figure 1.09**). These first examples were interesting to inorganic chemists due to the electronic structure of these complexes. The observation of redox-activity has been shown in these cases to involve ligand π or π^* orbitals that are close in energy to the *d*-orbitals of the metal center.

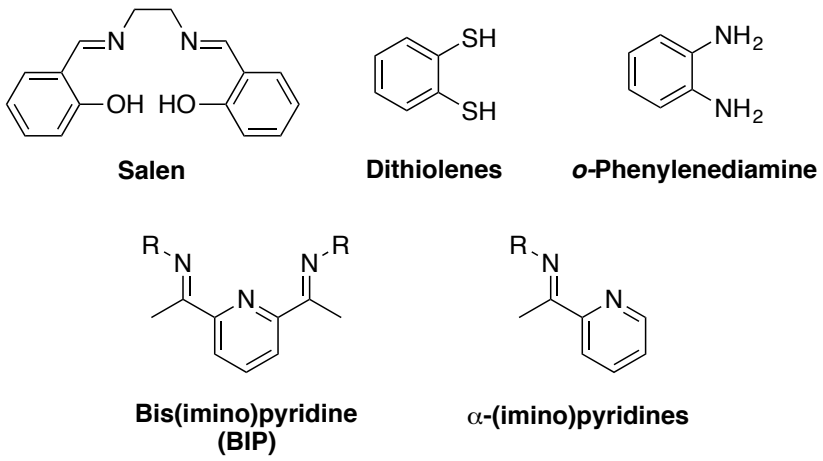

Figure 1.09: Structures of typical redox-active ligands.

While these complexes have unique spectroscopic properties, some of them have shown promise at performing multiple electron redox transformations that are typically reserved for noble metals. The Chirik group has reported multiple types of catalytic chemistry with reduced bis(imino)pyridine complexes. For example they have demonstrated the ability of a monomeric Fe complex to perform hydrogenation of olefins. A putative catalytic cycle identified two key $2e^-$ redox transformations, oxidative addition of H_2 and reductive elimination of the alkane.[52] The same complex served as a catalyst for [2π+2π] cycloaddition of dienes where a proposed reductive elimination of the cyclized product is critical.[53] The precatalyst is a doubly reduced ferrous(bis)iminopyridine complex that was later established as an Fe(II) doubly reduced ligand (**Figure 1.10**).[50] A second generation bis(imino)pyridine pre-catalyst was shown to do hydrogenation where reducing equivilants originate from both the ligand and metal redox orbitals, highlighting the cooperativity between the metal and ligand redox reservoirs.[54] The ability of the ligand redox orbitals to participate in these critical 2 e^- steps is essential to preventing complications of high valent or low valent oxidation states of the Fe metal center.

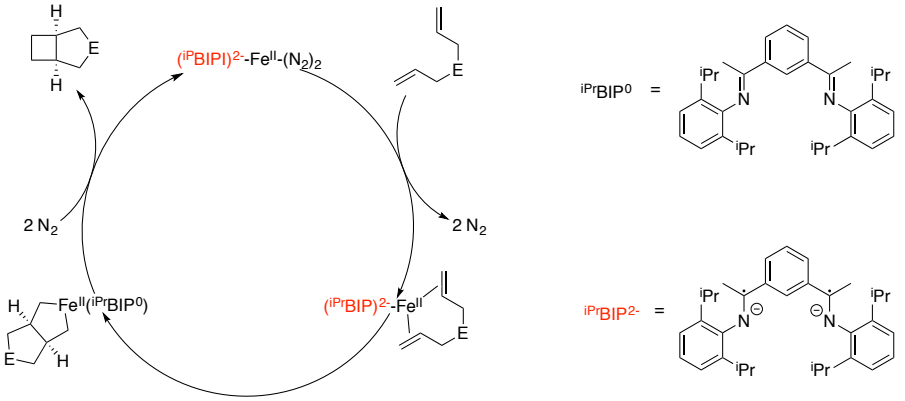

Figure 1.10: Proposed catalytic cycle of a bicyclization consisting of a 2e$^-$ reduction of the substrate.[53] The two electrons originate from a ligand based redox orbital.

Tobias Ritter has shown the competence of an α-(imino)pyridine catalyst in hydrosilations of dienes.[55] The proposed catalytic cycle is initiated by oxidative addition of silane and is completed with the reductive elimination of the hydrosilation product. Both of these steps require a 2e$^-$ redox chemistry to occur at the metal center. The availability of the ligand redox orbitals is thought to be critical to mitigate the electronic demands at the metal center. This property can maximize catalyst turnover by preventing degradation through the formation of an Fe(0) product.[56] Tuning the energetics of the metal redox-orbitals and the ligand-based orbitals is essential for these catalysts to function.

While Chirik and Ritter have showcased the activity of these redox-active ligands in the participation of 1st row transition metal catalysts, there remains much to understand about these unique systems. The Betley group has demonstrated that suitable energetics alone does not guarantee the ligand will participate in redox transformations.[57] The tris(5-mesitylpyrrolyl)ethane (TPE) ligand was shown to undergo a ligand-based oxidation with outer-sphere oxidants when coordinated to 1st row divalent metals.[58] However, inner-sphere oxidants undergo an entirely metal-based oxidation with no participation of the ligand-based redox-orbitals (**Scheme 1.03**).[59] The Betley group proposes that the π overlap of the ligand redox orbitals with the metal-based *d*-orbitals prevents ligand-based oxidation. The difference in the

energetics of the ligand-based orbitals and metal-based orbitals may not provide a large enough thermodynamic driving force for an electron transfer from the ligand HOMO orbital to the metal orbital.[59] However, the addition of an inner-sphere would alter the molecular orbitals and could conceivably change the HOMO orbital to be more metal-based as seen with the metal oxidation. Consequently, understanding the interactions between multiple redox-reservoirs around a metal center would be essential for designing future effective homogeneous catalysts.

Scheme 1.03: Reactivity of a ferrous TPE complex with both inner-sphere and outer-sphere oxidants.[59]

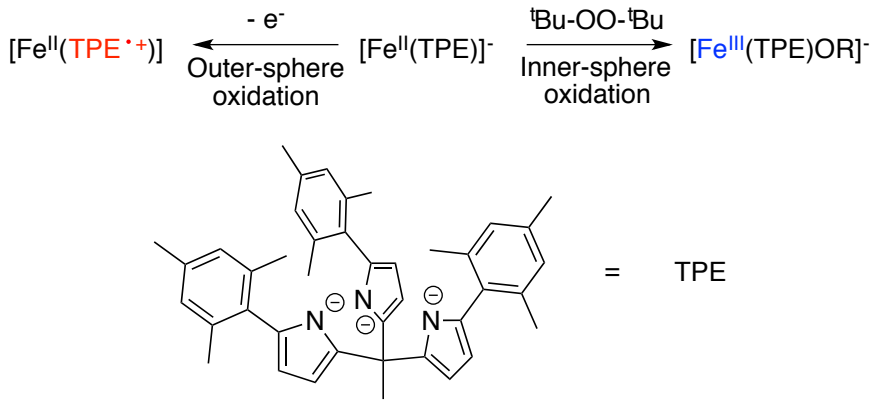

While the design of these catalysts have been influenced by cytochrome P450 and the involvement of the porphyrin redox state, few have incorporated a thiolate. As previously mentioned, there is now belief that significant organic radical character is maintained on the axial cysteinate. Due to the interactions between the cysteinate and the porphryin it is essential to synthesize and characterize synthetic complexes containing a redox-active ligand along with a coordinated thiolate. Probing these interactions on model systems can impact our understanding of the complex synergy of the multiple pieces of cytochrome P450. As of now, there is a one example of a ferrous bis(imino)pyridine complex with a coordinated thiolate that was reported by David Goldberg.[60] This complex has unique structural parameters that may be suggestive of thiolate involvement in the redox-active bis(imino)pyridine framework.

Notes to Chapter 1

1. Holm R. H.; Kennepohl P.; Solomon E. I. *Chem. Rev.* **1996**, *96*, 2239-2314.

2. Lippard, S. J.; Berg, J. M. *Principles of Bioinorganic Chemisty*. University Science Books: Mill Valley, CA, 1994; P 411

3. Kovacs, J. A. *Chem. Rev.* **2004**, *104*, 825–848.

4. Kitajima, N.; Fujisawa, K.; Fujimoto, C.; Morooka, Y.; Hashimoto, S.; Kitagawa, T.; Toriumi, K.; Tatsumi, K.; Nakamura, A. *J. Am. Chem. Soc.* **1992**, *114*, 1277–1291.

5. Magnus, K. A.; Ton-That, H.; Carpenter, J. E. *Chem. Rev.* **1994**, *94* (3), 727–735.

6. Kovacs, J. A.; Brines, L. M. *Acc. Chem. Res.* **2007**, *40*, 501–509.

7. Green, M. T. *J. Am. Chem. Soc.* **1998**, *120*, 10772-10773.

8. Kennepohl, P.; Neese, F.; Schweitzer, D.; Jackson, H. L.; Kovacs, J. A.; Solomon, E. I. *Inorg. Chem.* **2005**, *44*, 1826-1836.

9. Denisov, I. G.; Makris, T. M.; Sligar, S. G.; Schlichting, I., *Chem. Rev.* **2005**, *105*, 2253-2278.

10. Shaik, S.; Cohen, S.; Wang, Y.; Chen, H.; Kumar, D.; Thiel, W. *Chem. Rev.* **2010**, *110*, 949–1017.

11. Ortiz de Montellano, P. R. *Chem. Rev.* **2010**, *110*, 932–948.

12. Denisov, I. G.; Mak, P. J.; Makris, T. M.; Sligar, S. G.; Kincaid, J. R. *J. Phys. Chem. A* **2008**, *112*, 13172–13179.

13. Mak, P. J.; Denisov, I. J.; Victoria, D.; Makris, T. M.; Deng, T; Sligar, S. G.; Kincaid, J. R. *J. Am. Chem. Soc.* **2007**, *129*, 6382–6383.

14. Poulos, T. L.; Finzelsy, B. C.; Gunsalusll, I. C.; Wagner, G. C.; Kraut, J. *J. Biol. Chem.* **1985**, *260*, 16122–16130.

15. Poulos, T. L.; Finzel, B. C.; Howard, A. J. *J. Mol. Biol.* **1987**, *195*, 687–700.

16. Dawson, J. H.; Sono, M. *Chem. Rev.* **1987**, *87*, 1255–1276.

17. Dey, A.; Jiang, Y.; Ortiz de Montellano, P.; Hodgson, K. O.; Hedman, B.; Solomon, E. I. *J. Am. Chem. Soc.* **2009**, *131*, 7869–7878.

18. Yoshioka, S.; Takahashi, S.; Ishimori, K.; Morishima, I. *J. Inorg. Biochem.* **2000**, *81*, 141–151.

19. Ogliaro, F.; de Visser, S. P.; Shaik, S. *J. Inorg. Biochem.* **2002**, *91*, 554–567.

20. Dey, A.; Okamura, T.; Ueyama, N.; Hedman, B.; Hodgson, K. O.; Solomon, E. I. *J. Am. Chem. Soc.* **2005**, *127*, 12046-12053.

21. Sivaramakrishnan, S.; Ouellet, H.; Matsumura, H.; Guan, S.; Moënne-Loccoz, P.; Burlingame, A. L.; Ortiz de Montellano, P. R. *J. Am. Chem. Soc.* **2012**, *134*, 6673–6684.

22. Schöneboom, J. C.; Lin, H.; Reuter, N.; Thiel, W.; Cohen, S.; Ogliaro, F.; Shaik, S. *J. Am. Chem. Soc.* **2002**, *124*, 8142-8151.

23. Rittle, J.; Green, M. T. *Science* **2010**, *330*, 933-937.

24. Green, M. T. *J. Am. Chem. Soc.* **1999**, *121*, 7939-7940.

25. Green, M. T.; Dawson, J. H.; Gray, H. B. *Science* **2004**, *304*, 1653-1656.

26. Auchère, F.; Rusnak, F. *J. Biol. Inorg. Chem.* **2002**, *7*, 664–667.

27. Fridovich, I. *Acc. Chem. Res.* **1972**, *5*, 321–326.

28. Kurtz, D. M.; Coulter, E. D. *J. Biol. Inorg. Chem.* **2002**, *7*, 653–658.

29. Yeh, A. P.; Hu, Y; Jenney, F. E.; Adams, M. W.; Rees, D. C. *Biochemistry* **2000**, *39*, 2499–2508.

30. Rodrigues, J. V.; Abreu, I. A.; Cabelli, D.; Teixeira, M. *Biochemistry* **2006**, *45*, 9266-9278.

31. Coulter, E. D.; Emerson, J. P.; Kurtz Jr., D. M.; Cabelli, D. E. *J. Am. Chem. Soc.* **2000**, *122*, 11555–11556.

32. Mathé, C.; Mattioli, T. A.; Horner, O.; Lombard, M.; Latour, J.; Fontecave, M.; Nivière, V. *J. Am. Chem. Soc.* **2002**, *124*, 4966-4967.

33. Roelfes, G.; Vrajmasu, V.; Chen, K.; Ho, R. Y. N.; Rohde, J.; Zondervan, C.; la Crois, R. M.; Schudde, E. P.; Lutz, M.; Spek, A. L.; Hage, R.; Feringa, B. L.; Münck, E.; Que, L. . *Inorg. Chem.* **2003**, *42*, 2639-2653.

34. Katona, G.; Carpentier, P.; Nivière, V.; Amara, P.; Adam, V.; Ohana, J.; Tsanov, N.; Bourgeois, D. *Science* **2007**, *316*, 449-453.

35. Kurtz, D. M. *Acc. Chem. Res.* **2004**, *37*, 902–908.

36. Simaan, A. J.; Döpner, S.; Banse, F.; Bourcier, S.; Bouchoux, G.; Boussac, A.; Hildebrandt, P.; Girerd, J.-J. *Eur. J. Inorg. Chem.* **2000**, *2000* (7), 1627–1633.

37. Bernal, I.; Jensen, I. M.; Jensen, K. B.; McKenzie, C. J.; Toflund, H.; Tuchagues, J. P. *J. Chem. Soc. Dalton Trans.* **1995**, 3667-3675.

38. Wada, A.; Ogo, S.; Nagatomo, S.; Kitagawa, T.; Watanabe, Y.; Jitsukawa, K.; Masuda, H. *Inorg. Chem.* **2002**, *41*, 616–618.

39. Ahmad, S.; McCallum, J. D.; Shiemke, A. K.; Appelman, E. H.; Loehr, T. M.; Sanders-Loehr, J. *Inorg. Chem.* **1988**, *27*, 2230–2233.

40. Krishnamurthy, D.; Kasper, G. D.; Namuswe, F.; Kerber, W. D.; Narducci Sarjeant, A. A.; Moënne-Loccoz, P.; Goldberg, D. P. *J. Am. Chem. Soc.* **2006**, *128*, 14222–14223.

41. Namuswe, F.; Kasper, G. D.; Sarjeant, A. A. N.; Hayashi, T.; Krest, C. M.; Green, M. T.; Moënne-Loccoz, P.; Goldberg, D. P. *J. Am. Chem. Soc.* **2008**, *130*, 14189–14200.

42. Namuswe, F.; Hayashi, T.; Jiang, Y.; Kasper, G. D.; Sarjeant, A. A. N.; Moënne-Loccoz, P.; Goldberg, D. P. *J. Am. Chem. Soc.* **2010**, *132*, 157–167.

43. Shearer, J.; Nehring J.; Lovell, S.; Kaminsky, W.; Kovacs, J. A. *Inorg. Chem.* **2001**, *40*, 5483-5484.

44. Shearer, J.; Scarrow, R. C.; Kovacs, J. A. *J. Am. Chem. Soc.* **2002**, 11709-11717.

45. Kitagawa, T.; Dey, A.; Lugo-Mas, P.; Benedict, J. B.; Kaminsky, W.; Solomon, E. I.; Kovacs, J. A. *J. Am. Chem. Soc.* **2006**, *128*, 14448-14449.

46. Chirik, P. J.; Wieghardt, K. *Science* **2010**, *327*, 794-795.

47. Storr, T.; Verma, P.; Pratt, R. C.; Wasinger, E. C.; Shimazaki, Y.; Stack, T. D. P. *J. Am. Chem. Soc.* **2008**, *130*, 15448–15459.

48. Stiefel, E. I.; Waters, J. H.; Billig, E.; Gray, H. B. *J. Am. Chem. Soc.* **1965**, *87*, 3016–3017.

49. Herebian, D.; Bothe, E.; Neese, F.; Weyhermüller, T.; Wieghardt, K. *J. Am. Chem. Soc.* **2003**, *125*, 9116-9128.

50. Bart, S. C.; Chłopek, K.; Bill, E.; Bouwkamp, M. W.; Lobkovsky, E.; Neese, F.; Wieghardt, K.; Chirik, P. J. *J. Am. Chem. Soc.* **2006**, *128*, 13901–13912.

51. Lu, C. C.; Bill, E.; Weyhermüller, T.; Bothe, E.; Wieghardt, K. *J. Am. Chem. Soc.* **2008**, *130*, 3181-3197.

52. Bart, S. C.; Lobkovsky, E.; Chirik, P. J. *J. Am. Chem. Soc.* **2004**, *126*, 13794–13807.

53. Bouwkamp M. W.; Bowman, A. C.; Lobkovsky, E.; Chirik, P. J. *J. Am. Chem. Soc.* **2006**, *128*, 13340-13341.

54. Hoyt, J. M.; Sylvester, K. T.; Semproni, S. P.; Chirik, P. J. *J. Am. Chem. Soc.* **2013**, *135*, 4862–4877.

55. Wu, J. Y.; Moreau, B.; Ritter, T. *J. Am. Chem. Soc.* **2009**, *131*, 12915–12917.

56. Wu, J. Y.; Stanzl, B. N.; Ritter, T. *J. Am. Chem. Soc.* **2010**, *132*, 13214–13216.

57. King, E. R.; Betley, T. A. *J. Am. Chem. Soc.* **2009**, *131* (40), 14374–14380.

58. Sazama, G. T.; Betley, T. A. *Inorg. Chem.* **2010**, *49* (5), 2512–2524.

59. Sazama, G. T.; Betley, T. A. *Inorg. Chem.* **2014**, *53* (1), 269–281.

60. Widger, L. R.; Jiang, Y.; Siegler, M. A.; Kumar, D.; Latifi, R.; de Visser, S. P.; Jameson, G. N. L.; Goldberg, D. P. *Inorg. Chem.* **2013**, *52*, 10467–10480.

Chapter 2.

Synthesis and Characterization of a Family of Fe α-(Imino)-*N*-Heterocycle complexes; Preliminary Reactivity with Small Substrates.

Portions of this chapter have been adapted from: Leipzig, B. K.; Rees, J. A.; Nyrov, A.; Theisen, R.; Flowers, S. E.; Kaminsky, W.; DeBeer, S.; Kovacs, J. A. *In Preparation*.[1]

Introduction:

Metalloenzymes perform many functions critical to life on earth. The ability of these enzymes to accomplish their catalytic function is dependent on numerous specific geometric arrangements in both the primary and secondary coordination sphere.[2] As discussed in the introductory chapter, the addition of a thiolate can have a remarkable influence on the properties of Fe metalloenzymes, which will be further elaborated here.[3,4]

Our group has shown that the model system $[Fe^{II}(S^{Me2}N_4(tren))]^+$ has remarkable similarities to the SOR. In this model system, superoxide will bind and oxidize the ferrous metal center to provide a metastable ferric hydroperoxo intermediate **(Figure 2.01)**.[5,6] Akin to the metalloenzyme, this intermediate can be protonated at the proximal oxygen and release H_2O_2; the resulting ferric metal center can be reduced to regenerate the starting complex. While this intermediate is quite similar to that of the T1 species of SOR in regards to the N_4S primary coordination sphere, there are geometric and electronic differences between the two. Unlike the enzyme, which has the cysteinate *trans* to the peroxo, our model system constrained the thiolate *cis* to the peroxo.[7] In addition, the high-spin Fe metal center in SOR is thought to be essential in weakening the Fe-O bond and releasing the hydrogen peroxide, however our model system is a low-spin S=1/2, though still releases H_2O_2.[8]

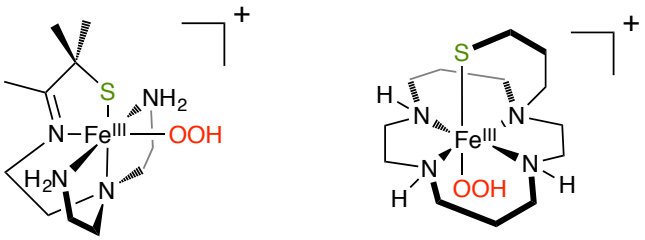

$[Fe^{III}trenS\text{-}OOH]^+$
L.S. S=1/2
cis thiolate

$[Fe^{III}cyclamPrS\text{-}OOH]^+$
H.S. S=5/2
trans thiolate

Figure 2.01: Synthetic models incorporating a thiolate in the primary coordination sphere.

To further investigate the importance of the thiolate position in SOR, our group has prepared a second model system that incorporates cyclam in the basal plane with a pendant thiolate arm that is *trans* to the open site. The model system, $[Fe^{II}(cyclam\text{-}PrS]^{+}$, also reacts with superoxide and forms an intermediate that has a very low $\nu_{Fe\text{-}O}$ stretch at 419 cm^{-1}, which is similar to a mutant enzyme which has an $\nu_{Fe\text{-}O}$ of 438 cm^{-1}.[9,10] This is due to the high-spin nature of the Fe in the model complex and the thiolate having a strong *trans* effect and weakening the Fe-O bond.

To further highlight the importance of the geometry of the primary coordination sphere, more synthetic models need to be prepared. These new model systems will provide benchmark spectroscopic parameters to understand crucial enzymatic intermediates. A new system has been reported by the Kovacs group that incorporates a tripodal backbone with a thiolate and two primary amines. It is hypothesized that the condensation of aromatic pyridines to this tripodal base may impart a rigid basal plane and place the thiolate *trans* to an open site (**Figure 2.02**). However, it was observed that this new system does not form a monomeric species in the solid state, rather a bis μ-thiolate dimeric geometry, even in coordinating solvent solutions.[11] However, two new systems have been designed with differing *N*-heterocycles (**Figure 2.02**). This family of complexes has some unique ligand bond lengths that suggests an interesting electronic structure.

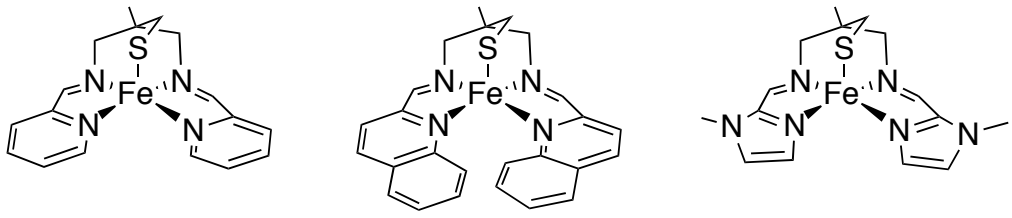

Figure 2.02: Idealized square pyramidal metal complex containing a thiolate *trans* to the open site using the tripodal tame(N_2S) backbone.

Experimental:

General Considerations: Sodium azide, 1-hydroxybenzotriazole (HOBt), dicyclohexylcarbodiimide, 3,3'-aminopropylamine, di-tert-butyl dicarbonate, 2-(tert-butoxycarbonylamino)isobutyric acid, iron(II) acetate, iron(II) chloride, and tetraphenyl phosphonium chloride were all purchased from TCI and used as received. 3-methyl-3-oxetanemethanol (**1**) was purchased from Sigma-Aldrich and used without further purification. DMSO-d_6, $CDCl_3$ and MeCN-$_{d3}$ were purchased from Cambridge Isotope Labs and used as received. EtOH was purchased from Decon and degassed prior to use. Et_2O was purchased from Fischer Scientific and purified using a solvent purification columns housed in a custom stainless steel cabinet and dispensed by a stainless steel Schlenk-line (GlassContour). All other solvents were purchased from Sigma Aldrich. MeOH, MeCN and CH_2Cl_2 were dried and distilled prior to use. A 48% aqueous solution of hydrobromic acid was purchased from Alfa-Aesar and used as received. Ammonia was obtained from Praxair while all other material was purchased and used as received from Sigma Aldrich.

^1H and ^{13}C NMR spectra were obtained on a Bruker AV300, AV301, DRX499, or AV500. Chemical shifts are listed in parts per million and were reported relative the residual protio solvent. UV/Vis spectra were recorded on a Varian Cary 50 spectrophotometer equipped with a fiber optic cable connected to a "dip" ATR probe (C-technologies). A custom-built two neck solution sample holder equipped with a threaded glass connector was sized specifically to fit the "dip" probe. Electrospray ionization mass spectrometry (ESI-MS) was preformed on a Bruker Esquire LC-Ion Trap. X-ray crystallographic data was recorded on a Bruker APEX II single crystal X-ray diffractometer using Mo-radiation. Elemental analysis were preformed by

Atlantic Microlab, Inc. Norcross, Ga. Infrared spectra were recorded on a Bruker Tensor 27 FTIR instrument.

All manipulations were performed using Schlenk techniques or under a N_2 atmosphere in a glovebox. The synthesis of 2-bromomethyl-2-methyl-propane-1,3-diol (**2**) and 2-benzylsulfanyl methyl-2-methyl-propane-1,3-diol (**3**) was performed according to a modified literature procedure.[12]

Synthesis of (3-methanesulfonyl-2-methanesulfonylmethyl-2-methyl-propylsulfanylmethyl)-benzene (4). Methanesulfonyl chloride (18.2 g, 159 mmol) was added dropwise to a CH_2Cl_2 (375 mL) solution containing **3** (9.0 g, 39.8 mmol), triethylamine (TEA) (24.1 g, 239 mmol) and a catalytic amount (0.3g) of 4-dimethylaminopyridine at 0°C. The orange solution was monitored by TLC through the disappearance of the starting material. The reaction was then allowed to warm to room temperature. Water (300 mL) was added to the solution and extracted with CH_2Cl_2 (2 x 300 mL), the combined organics were washed with water and brine (2 x 100 mL each) prior to drying with sodium sulfate. Solvents were removed *in vacuo* and the orange oil was purified to an off yellow oil by column chromatography (1:1 EtOAc:hexanes) in 87% yield. ^{1}H NMR (300 MHz, $CDCl_3$) δ 7.33 (m, 5H), 4.09 (d, ^2J=10 Hz, 2H), 4.03 (d, ^2J=10 Hz, 2H), 3.75 (s, 2H), 3.01 (s, 6H), 2.53 (s, 2H), 1.08 (s, 3H). ESI-MS: expected *m/z* for $C_{14}H_{22}O_6S_3$= 382.1 found 382.2.

Synthesis of (3-azido-2azidomethyl-2-methyl-propylsulfanylmethyl)-benzene (5). (4) (8.0 g, 21 mmol) was added to a solution of sodium azide (12.3 g, 189 mmol) in DMF (130 mL) and refluxed for 3 days. After cooling to room temperature, water (130 mL) was added and the

organics were extracted with EtOAc (3x 200 mL). The combined organics were combined and washed water and brine (2 x 200 mL each) wherein the reaction mixture was dried with sodium sulfate. The solvent was removed *in vacuo* and the resulting yellow oil was purified by silica gel column chromatography (4:1 hexanes:EtOAc) to yield **5** as an off white oil in 80% yield. ^{1}H NMR (300 MHz, $CDCl_3$) δ 7.34 (m, 5H), 3.74 (s, 2H), 3.29 (d, ^{2}J=12 Hz, 2 H), 3.24 (d, ^{2}J=12 Hz, 2 H), 2.44 (s, 2H), 0.98 (s, 3H).

Synthesis of 2-benzylsulfanylmethyl-2-methyl-propane-1,3-diamine (6). 5 (2.0 g, 7.2 mmol) was added drop wise to a stirred solution of lithium aluminum hydride (LAH) (1.1 g, 28.8 mmol) in ether (150 mL) at 0°C. Once the reaction was complete water was added slowly to quench the excess LAH. The reaction was then filtered through Celite and dried with sodium sulfate. The ether was removed *in vacuo* and the clear oil was placed in an aqueous solution (10 mL) and acidified to pH 2.0. The aqueous solution was washed with ether (3 x 20 mL) before being basified to pH 12.0. The product was then extracted ether (3 x 40 mL). The combined organics were dried with sodium sulfate and then removed *in vacuo* to yield **6** as a clear oil in 51% yield. ^{1}H NMR (300 MHz, $CDCl_3$) δ 7.32 (m, 5H), 3.70 (s, 2H), 2.55 (s, 4H), 2.44 (s, 2H), 0.86 (s, 3H). ESI-MS: expected *m/z* for $C_{12}H_{20}N_2S$= 224.1, found *m/z*=225.1.

Synthesis of 2-benzylsulfanylmethyl-2-methyl-propane-1,3-(*tert*-Butyloxycarbonyl) diamine (7). **6** (4.7g, 20 mmol) was dissolved in CH_2Cl_2 (50 mL) and cooled to 0°C. di-*tert*-butyl dicarbonate (9.1g, 40mmol) was dissolved in CH_2Cl_2 (10 mL) and added dropwise to the solution of **6**. This solution was allowed to warm to room temperature overnight. The solution was washed with brine (2 x 50 mL) and dried over Na_2SO_4. Volatiles were removed *in vacuo* to

afford **7** as a white solid in 95% yield (8.1g) ^{1}H NMR (300 MHz, $CDCl_3$) δ 7.33 (m, 5H), 5.03 (bs, 2H), 3.69 (s, 2H), 3.048 (*dd*, ^{3}J=7.5 Hz, ^{2}J=14.7 Hz, 2H), 2.80 (*dd*, ^{3}J=6.3 Hz, ^{2}J=14.9 Hz 2H), 2.35 (s, 2H), 1.44 (s, 18H), 0.86 (s, 3H). ESI-MS: expected *m/z* for $C_{22}H_{36}N_2O_4S$= 424.1, found *m/z*=425.1

Synthesis of 2-thiomethyl-2-methyl-propane-1,3-(*tert*-Butyloxycarbonyl) diamine (8). To a stirred solution of liquid ammonia (50 ml) cooled to -78°C, was added sodium metal (200 mg). **7** (2.9g, 6.8 mmol) of was added in 0.3 g portions. Additional sodium was periodically added in small proportions to maintain the deep blue color. The completion of the reaction was assumed once the solution maintained its deep blue color for more than 1 h. Ammonium chloride was added until the solution changed from blue to yellow, thus quenching the sodium. The liquid ammonia was evaporated under a stream of N_2. A 50 mL, 0.025M K_2HPO_4 and 0.025M NaH_2PO_4 aqueous solution was then added and the reaction was acidified with 37% HCl until the reaction reached a pH of 2. The organic product was extracted with dichloromethane (4 x 75ml). The organics were then dried with Na_2SO_4 and the volatiles were removed to afford **8** as a foul smelling oil in 93% yield (2.1 g) ^{1}H NMR (300 MHz, $CDCl_3$) δ 5.26 (bs, 2H), 3.00 (m, 4H), 2.41 (d, ^{3}J=9 Hz 2H), 1.66 (t, ^{3}J=9 Hz 1H), 1.46 (s, 18H) 0.89 (s, 3H). ESI-MS: expected *m/z* for $C_{15}H_{30}N_2O_4S$= 334.1, found *m/z*=335.1

Synthesis of 2-thiomethyl-2-methyl-propane-1,3-diamine dihydrogenchloride (9).

5ml of 4M HCl in dioxane was added to **8** (2.1g, 6.4 mmol) in methanol (2 mL). Gas evolution was observed and this was allowed to stir overnight. The volatiles were removed to afford a **9** as a white solid in 95% yield (1.2 g) ^{1}H NMR (300 MHz, DMSO-d_6) δ 8.12 (bs, 5H, NH_2), 2.91 (bs,

4H), 2.65 (s, 2H), 1.02 (s, 3H). ESI-MS: expected *m/z* for $C_5H_{16}Cl_2N_2S$= 207.1, found *m/z*=135.1 (No HCl's)

Synthesis of $[(Fe^{II}(Tame\text{-}N_2SPy_2))_2](PF_6)_2$ (10). **9** (0.2 g, 1 mmol) was added to a vial containing a stirred solution of sodium methoxide (0.156 g, 3 mmol) in of methanol (10 mL). 2-pyridinecarboxaldehyde (0.21g, 2mmol) was then added and the stirred suspension was cooled to -40° C. In a separate vial, iron (II) chloride (0.126 g, 1 mmol) dissolved in methanol (50 mL) and cooled to -40° C. The iron solution was then slowly added to the organic solution. Immediately, the solution became a deep turquoise color. This was stirred for 1h at which time sodium hexafluorophosphate (0.168g, 1mmol) was added. This solution was stirred overnight at which time a dark solid precipitated out. The methanol was removed and the solid was dissolved in acetonitrile, and filtered through celite. The deep turquoise solution was concentrated to a minimal volume (~ 2 mL) upon which Et_2O was layered to isolate a deep blue solid in 70% yield (360 mg). Electronic absorption spectrum: λ_{max} (nm) (ε ($M^{-1}cm^{-1}$): (MeCN): 420 (6,150), 580 (9,100), and 650 (11,800)). ^{1}H NMR (300 MHz, MeCN-d_3) δ 9.3 (s, 1H), 9.00 (s, 1H), 8.97 (s, 1H) 8.15, (m, 3H), 7.75 (t ^3J 7.5 Hz, 1H), 7.45 (m, 2H), 7.09 (t ^3J=7 Hz, 1H), 4.14 (d ^2J=12.7 Hz, 1H) 3.77 (m, 3H), 1.04 (s, 3H), 0.90 (d, ^2J=13.3 Hz 1H), 0.31 (d ^2J=13.4 Hz, 1H); ^{13}C NMR (500 MHz, MeCN-d_3) δ 169.2 (s, 2C), 168.5 (s, 2C), 160.2 (s, 2C), 158.9 (s, 2C), 154.4 (s, 2C), 153.3 (s, 2C), 136.9 (s, 2C), 136.1 (s, 2C) 128.8 (s, 2C), 128.1 (s, 2C), 125.4 (s, 2C), 125.2 (s, 2C), 69.0 (s, 2C), 67.0 (s, 2C), 43.4 (s, 2C), 26.6 (s, 2C), 24.8 (s, 2C) ESI-MS: expected *m/z* for $[C_{34}H_{38}N_8S_2Fe_2]^{2+}$= 367.1, found *m/z*=367.1 Elemental Analysis for $C_{34}H_{38}F_{12}N_8P_2S_2Fe_2$ Calculated: C, 39.86; H, 3.74; N, 10.94. Found C, 39.28; H, 3.73; N; 10.80.

Synthesis of $[(Fe^{II}(Tame\text{-}N_2SQu_2))_2]^{2+}$ $(PF_6)_2$ (11). 11 was isolated following a similar procedure as **10**. A deep blue solid was isolated by layering Et_2O onto a concentrated solution of **11** in DCM in 67% yield (410 mg). λ_{max} (nm) (ε ($M^{-1}cm^{-1}$): (MeCN): 420 (6,240), 607 (14,830), and 719 (19,500)). ^{1}H NMR (300 MHz, MeCN-d_3) δ 9.81 (s, 2H), 8.30 (d, ^2J=8.5hz, 2H), 8.06 (d, ^2J=8.4hz, 2H), 7.90 (d, ^2J=7.8hz, 2H), 7.58 (t, ^3J=7.4hz, 2H), 7.47 (t, ^3J=7.7hz, 2H), 6.50 (d, ^2J =8.3hz, 2H), 4.77 (d, ^2J =15.1hz, 2H) 3.87 (d, ^2J 15.1hz, 3H), 0.67 (s, 3H), 0.00 (s, 2H) ESI-MS: expected *m/z* for $[C_{50}H_{46}N_8S_2Fe_2]^{2+}$= 467.1, found *m/z*=467.1 Elemental Analysis for $C_{50}H_{46}F_{12}N_8P_2S_2Fe_2CH_2Cl_2$ Calculated: C, 46.77; H, 3.69; N, 8.56. Found C, 46.85; H, 3.73; N; 8.11.

Synthesis of $[(Fe^{II}(Tame\text{-}N_2SQu_2))_2]^{2+}$ $(BPh_4)_2$ (11-BPh_4). Crystals with the BPh_4 counterion were grown by a slow vapor diffusion of MeCN:Et_2O. λ_{max} (nm) (ε ($M^{-1}cm^{-1}$): (MeCN): 420 (6,240), 607 (14,830), and 719 (19,500)). ESI-MS: expected *m/z* for $[C_{50}H_{46}N_8S_2Fe_2]^{2+}$= 467.1, found *m/z*=467.1.

Synthesis of $[(Fe^{II}(Tame\text{-}N_2SImid(Me)_2))_2]^{2+}\bullet MeCN(PF_6)_2$ (12). 12 was isolated following the same procedure for **11**. A royal blue solid was obtained in 85% yield (440 mg) from layering of ether onto a concentrated volume of acetonitrile. Crystals were isolated in a slow diffusion of Et_2O into a concentrated volume of acetonitrile. λ_{max} (nm) (ε ($M^{-1}cm^{-1}$): (MeCN): 619 (11,500); (MeOH) 595 (4,600). Magnetic moment (solution MeCN 298K) 2.89μ_B ESI-MS: expected *m/z* for $[C_{30}H_{43}N_{12}S_2Fe_2]^{2+}$= 373.5, found *m/z*=373.1 Elemental Analysis for $C_{30}H_{42}F_{12}N_{12}P_2S_2Fe_2CH_3CN$ Calculated: C, 35.67; H, 4.21; N, 16.90. Found C, 35.57; H, 4.14; N; 16.74.

Reactions with $CO_{(g)}$. In a typical experiment 15-20mg of **10** or **12** was added to a medium walled J. Young NMR tube in MeCN-d_3. The NMR tube was rigorously degassed and was then pressurized with 5 atm of $CO_{(g)}$ for about 30 seconds. This NMR tube was then stirred slowly at room temperature over the course of days.

Synthesis of (Fe^{II}(Tame-N_2SPy_2)CN (10-CN): 9 (0.1 g, 0.5 mmol) was added to a vial containing a stirred solution of sodium methoxide (0.081 g, 1.5 mmol) in 10ml of methanol. 2-pyridinecarboxaldehyde (0.107 g, 1 mmol) was then added and the stirred suspension was cooled to -40° C. In a separate vial iron (II) chloride (0.063 g, 0.5 mmol) was dissolved in 5ml of methanol and cooled to -40° C. The iron solution was then slowly added to the organic solution. Immediately, the solution became a deep turquoise color. This was stirred for 1h at which time sodium cyanide (0.025g, 0.5mmol) was added. This solution was stirred overnight at which time a dark solid precipitated out. The methanol was removed and the solid was dissolved in dichloromethane, and filtered through celite. The deep turquoise solution was concentrated to a minimal volume (~2ml) upon which ether was layered to isolate a deep blue crystalline solid solid in 70% yield (360 mg). Electronic absorption spectrum: λ_{max} (nm) (ε ($M^{-1}cm^{-1}$): 353 (3,500), 409 (4600), 577 (3,600) 697 (4,200) (some may have decomposed). (MeCN) ^{1}H NMR (300 MHz, MeCN-d_3) δ 9.76 (d, ^3J=6 Hz, 1H), 9.15 (s, 1H), 8.76 (s, 1H) 8.00, (d, ^3J=12 Hz 1H), 7.86 (m, 2H), 7.68 (t, ^3J=12 1H), 7.45 (m, 2H), 7.10 (t, ^3J=10 Hz, 1H) 4.71 (d ^2J=16 Hz, 1H) 3.76 (m, 3H), 1.17 (s, 3H), 2 protons masked by solvent peak. ESI-MS: expected *m/z* for $C_{18}H_{19}N_5SFe$= 393.07, found *m/z*=393.1 IR (solution, CH_2Cl_2, cm^{-1}) ν (CN) 2087.

O_2 Reactions: An inert custom 'dip' probe cell was evacuated with $Ar_{(g)}$. To this a 0.05 mM solution of the corresponding complex was added. This custom cell could be immersed in a cold bath or heated to allow temperature control. Once temperature is equilibrated the cell was exposed to atmosphere and scans were recorded in timed intervals.

X-Ray Crystallographic Structure Determination

A lustrous green prism, **11**, measuring 0.20 x 0.15 x 0.13 mm^3 was mounted on a loop with oil. Data was collected at -173°C on a Bruker APEX II single crystal X-ray diffractometer, Mo-radiation. Crystal-to-detector distance was 40 mm and exposure time was 10 seconds per frame for all sets. The scan width was 0.5°. Data collection was 100% complete to 25° in ϑ. A total of 128992 reflections were collected covering the indices, h = -18 to 18, k = -18 to 18, l = -19 to 19. 11639 reflections were symmetry independent and the R_{int} = 0.0287 indicated that the data was of better than average quality (0.07). Indexing and unit cell refinement indicated a triclinic lattice. The space group was found to be P $\bar{1}$ (No. 2).

A blue piece, **12**, measuring 0.10 x 0.05 x 0.05 mm^3 was mounted on a loop with oil. Data was collected at -173°C on a Bruker APEX II single crystal X-ray diffractometer, Mo-radiation. Crystal-to-detector distance was 40 mm and exposure time was 30 seconds per frame for all sets. The scan width was 0.5°. Data collection was 99.9% complete to 25° in ϑ. A total of 50076 reflections were collected covering the indices, h = -19 to 19, k = -20 to 20, l = -21 to 20. 14435 reflections were symmetry independent and the R_{int} = 0.0608 indicated that the data was of slightly better than average quality (0.07). Indexing and unit cell refinement indicated a triclinic lattice. The space group was found to be P $\bar{1}$ (No. 2).

A dark blue translucent prism, **10-CN** measuring 0.38 x 0.03 x 0.03 mm^3 was mounted on a loop with oil. Data was collected at -173^oC on a Bruker APEX II single crystal X-ray diffractometer, Mo-radiation. Crystal-to-detector distance was 40 mm and exposure time was 120 seconds per frame for all sets. The scan width was 1^o. Data collection was 95.5% complete to 25^o in ϑ. A total of 46138 reflections were collected covering the indices, h = -46 to 46, k = -46 to 46, l = -8 to 8. 3647 reflections were symmetry independent and the R_{int} = 0.3106 indicated that the crystal was not that good and the data quite week. Indexing and unit cell refinement indicated a R-centered trigonal lattice. The space group was found to be R $\bar{3}$ (No.148).

The data was integrated and scaled using SAINT, SADABS within the APEX2 software package by Bruker. Solution by direct methods (SHELXS, SIR97[13,14]) produced a complete heavy atom phasing model consistent with the proposed structure. The structure was completed by difference Fourier synthesis with SHELXL97.[15,16] Scattering factors are from Waasmair and Kirfel.[17] Hydrogen atoms were placed in geometrically idealised positions and constrained to ride on their parent atoms with C---H distances in the range 0.95-1.00 Angstrom. Isotropic thermal parameters U_{eq} were fixed such that they were 1.2U_{eq} of their parent atom Ueq for CH's and 1.5U_{eq} of their parent atom U_{eq} in case of methyl groups. All non-hydrogen atoms were refined anisotropically by full-matrix least-squares. Crystallographic data for **11**, **12** and **10-CN** are presented in **Table 2.01**.

Table 2.01: Crystallographic data for **11**, **12** and **10-CN**.

	1	**12**	**10-CN**
Formula	$C_{98}H_{96}B_2FeN_8S_2$	$C_{70}H_{99}F_{24}Fe_4N_{29}P_4S_4$	$C_{70}H_{99}F_{24}Fe_4N_{29}P_4S_4$
MW (g/mol)	1527.8	2278.30	2359.75
Crystal System	Triclinic	Triclinic	Trigonal
Space Group	P-1	P-1	R-3
Unit Cell Dimensions			
a (Å)	13.35249(16)	13.9227(10)	39.021(7)
b (Å)	13.6085(16)	14.5427(19)	39.021(7)
c (Å)	14.5700(16)	15.0078(11)	7.0622(14)
α (deg)	71.249(5)	97.318(6)	90
β (deg)	66.021(5)	116.683(4)	90
γ (deg)	78.500(6)	112.025(6)	120
Final R indices	0.0317	0.0501	0.0987
R indices (all Data)	0.0363	0.0976	0.2270

Results and Discussion:

N_2S Ligand Design and Synthesis:

To attempt to fully mimic cysteinate ligated metalloenzymes, which contains the sulfur *trans* to an open site, a square pyramidal ligand system would have to be designed in which the thiolate is contained in the axial position. Previous work in our group used the *tren* ($N(EtNH_2)_3$) ligand scaffold, which with the addition of 3-methyl-3-mercapto-2-butanone, forms a trigonal bipyramidal geometry with the thiolate *cis* to the open site. To enforce a square planar type geometry, a tripodal backbone containing two primary amines and a thiolate was designed by the Kovacs group and is a derivative of 1,1,1 tris-(aminoethyl)ethane (tame).[10] This tripodal ligand framework should be suited for metal templated Schiff base condensations in order to isolate

pentadentate metal complexes that mimic the active sites of cysteinate ligated metalloenzymes. Ideally the conjugated aromatic rings would form a basal plane forcing the thiolate to retain a position *trans* to the vacant site. However, a crystal structure obtained in our group of an iron complex indicate these complexes have flexibility, allowing a geometry that places the thiolate *cis* to the open site and causing dimerization through bridging thiolates.[11]

Although this tame derivative has been used in the Kovacs lab previously, the ligand synthesis has been optimized and the puritiy of the final product improved (**Scheme 2.01**). The 7 step organic synthesis has an overall yield of 29%. The synthesis begins with the ring opening of 2-methyl-3-oxetanemethanol with HBr to generate **2**. The thiolate is then incorporated by nucleophilic attack of benzyl mercapton to yield **3**.[11] Since thiolates can be oxidized, the benzyl mercapton is essential due to the high stability of this protecting group and the duration of this lengthy organic synthesis.

Scheme 2.01: Eight-step synthetic route to isolate TameN_2SH•2HCl with an overall yield of 29%.

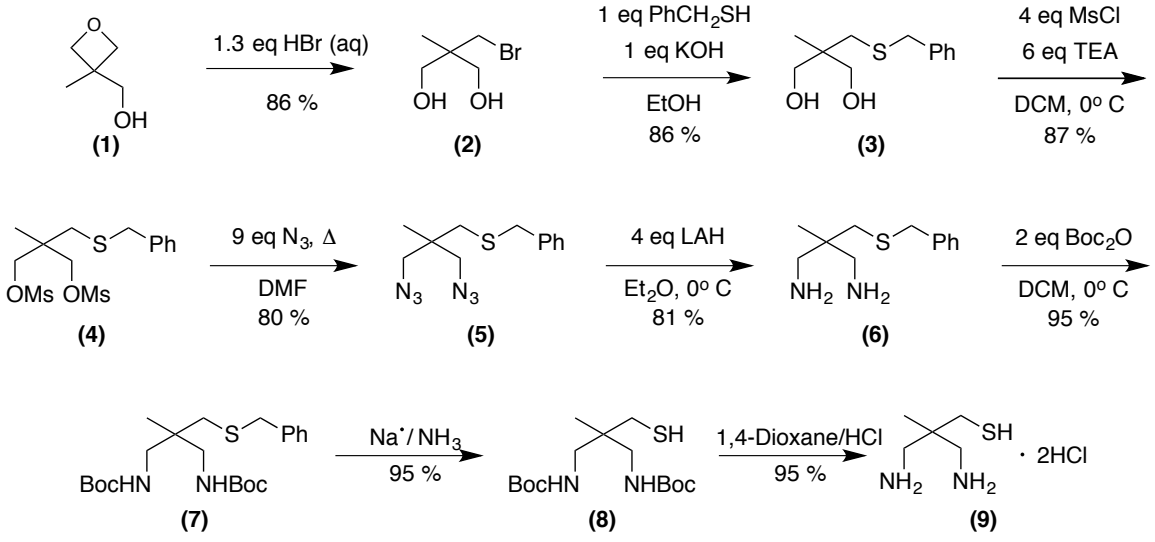

While TsCl was used in order to convert the alcohols to a better leaving group, this reaction took 2 days. Using MsCl would convert the alcohols to the mesylate product, **4**, in just hours and also afforded improved yields. Addition of sodium azide afforded the azide product **5** and a LAH reduction reduces the azide to the primary amine product **6**, essential for the metal template Schiff base condensation.

Previously, **6** is deprotected in one step with sodium metal, however this has proven to be unreliable. Elemental analysis using a one step deprotection indicates significant impurities in the organic product, with as much as 15% of the molar mass unaccounted for. The main issue with the straight deprotection is that isolating the thiolate product from the bi-products is difficult due to the pKas of the ammoniums groups and the thiolate group (pKa's of 10 and 9 respectively) being closely related. Excess sodium chloride and ammonium salts, which were generated during the workup, and potential alkoxide bi-products may all be present in this one step deprotection, thus lowering the purity of this step. These bi-products will affect the yield of the metal templated Schiff base condensation and the purity of the final metal complexes.

To circumvent these issues, an extra protection step has been added. The boc protection group is unaffected by the sodium reduction and the carboxamide functional group will allow for an organic work up to remove any salt bi-products. Stirring the product of the sodium reduction in an organic solution of HCl will remove the boc groups and afford the desired tripodal backbone as a di-HCl salt **9**. The purity of the isolated product was greatly improved through the addition of these two extra steps.

Structural Characterization of a Family of FeTame α-(imino)-N-heterocycle Complexes:

The complete pentadentate ligand was not isolated but instead synthesized coordinated to the metal in a one-pot metal-templated Schiff base condensation (**Scheme 2.02**). Using two equivalents of 2-pyridinecarboxyaldehyde along with one equivalent of the tripodal ligand and one equivalent of an Fe(II) source, **10** was isolated. When using the longer organic synthesis, much purer metal product was obtained, as confirmed with elemental analysis and yields that were over 30% higher than previously reported. However, the pyridine version does not form the desired monomeric square pyramidal geometry, but instead forms a dimer, bridged through *bis*-μ-thiolates.

Scheme 2.02: Iron templated Schiff base condensation to form the dimeric solid state structure.

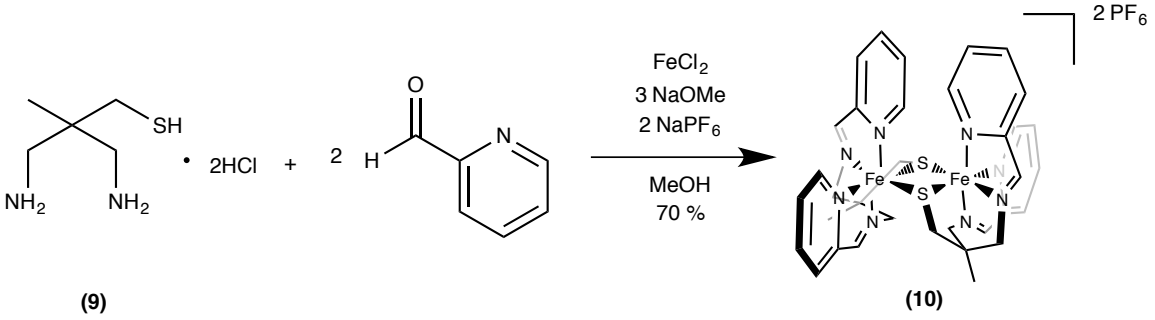

One way to favor monomeric products is to increase the steric bulk or alter the electronic parameters, both of which may be possible through the modification of the aldehyde and *N*-heterocyclic amine. This was done by incorporating commercially available quinoline and imidazole derivatives of the 2-pyridinecarboxyaldehyde to generate **11** and **12** respectively. Similar to **10** these two analogues form dimeric structures in the solid state (**Figure 2.03**). To favor a monomeric species, steric bulk is most likely necessary in a more proximal position to the thiolate. Our group has shown that the incorporation of *gem*-dimethyl groups adjacent to the thiolate stabilizes coordinatively unsaturated monomeric metal-thiolate complexes.[18,19] However,

the incorporation of *gem*-dimethyl groups using this synthesis may not be feasible due to the specific ring opening mechanism of the first step.

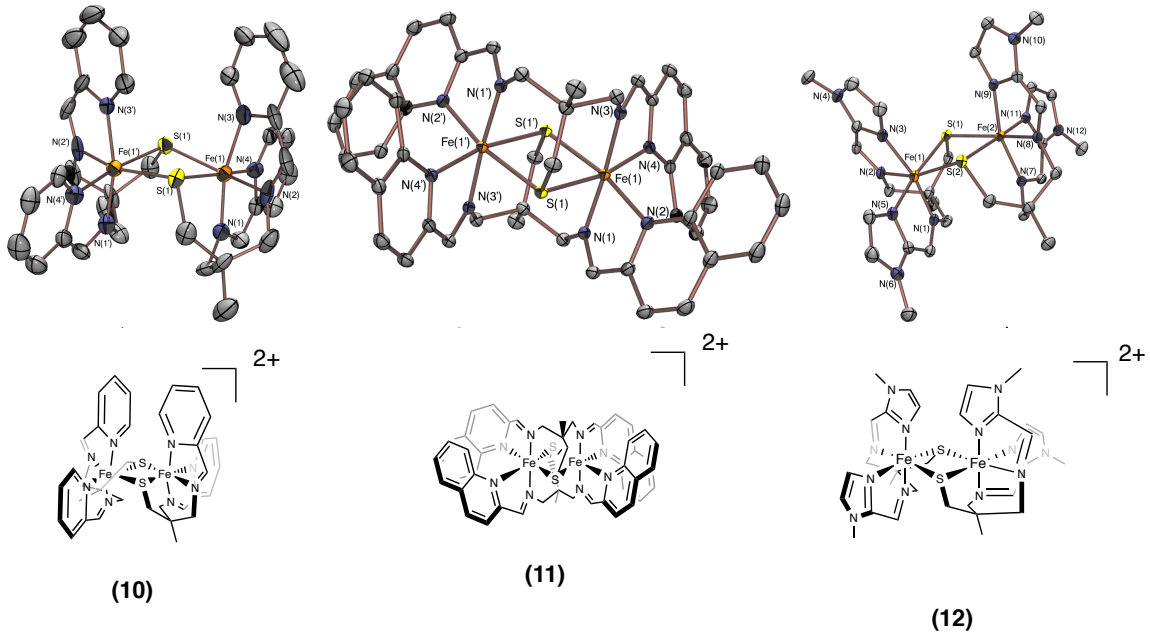

Figure 2.03: X-ray crystal structures of **10, 11, 12** with 50% probability ellipsoids. Counterions, cosolvents and hydrogens omitted for clarity (top). Corresponding structural representations (bottom).

In addition to the similar bridging μ-thiolates (**Figure 2.04**), all three complexes have comparable Fe-N bond lengths that are consistent with other low-spin Fe(II) systems (**Table 2.02**).[20,21] When considering the ligand environment it is not surprising that the metal favors a low-spin state. As a π-acceptor, the α-imino-*N*-heterocyle arms would favor a low spin metal center. The thiolate, even as a π-donor that would normally favor higher spin states, forms very covalent bonds with first row transition metals and, due to the nepheloxetic effect, can favor low-spin Fe complexes. In addition, the octahedral geometry would provide a splitting of the t_{2g}- and e_g^*-like orbitals and thus favor the low spin state.

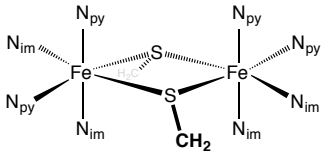

10

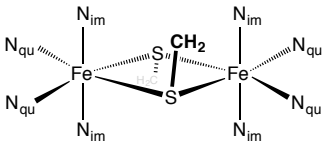

11

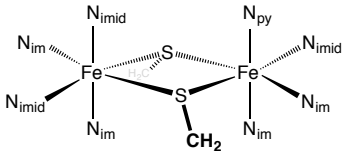

12

Figure 2.04: Schematic representation of the four atom core Fe_2S_2 for complexes **10-12**. Also including the S-C bond for reference.

However, there are differences between these three complexes. In contrast to the C_2 symmetric **10** and **12**, which are bridged only through the sulfur, **11** has C_{2h} symmetry. This may be due to the increase in sterics of the quinoline ring which forces the ligand to span both metals, with one α-(imino)quinoline arm coordinated to one metal and the other arm to the other. In contrast to the symmetric bis μ-thiolate core of **10** and **11**, the Fe-S bonds of **12** are less symmetric and suggest more facile cleavage of this dimer (*vide infra*).

Table 2.02: Selected bond lengths (Å) for complexes **10**, **11**, **12**, **13**. [a]Crystallographic dimers identical bond lengths on each Fe.

Bond Lengths	10[a]	11[a]	12
Fe(1)-S(1)	2.284(1)	2.273(1)	2.288(1)
Fe(1)-S(2/1')	2.289(1)	2.279(1)	2.311(1)
Fe(1)-N(1)	1.908(4)	1.949(1)	1.917(2)
Fe(1)-N(2)	1.916(4)	1.996(1)	1.923(2)
Fe(1)-N(3)	1.984(4)	1.949(1)	1.955(2)
Fe(1)-N(4)	1.997(4)	1.987(1)	-
Fe(1)-N(5)	-	-	1.966(2)
Fe(2)-S(1)	-	-	2.297(1)
Fe(2)-S(2)	-	-	2.283(1)
Fe(2)-N(7)	-	-	1.933(2)
Fe(2)-N(8)	-	-	1.925(2)
Fe(2)-N(9)	-	-	1.970(2)
Fe(2)-N(10)	-	-	-
Fe(2)-N(11)	-	-	1.973(2)

This family of complexes is unique in that it has three "redox-active" components: the metal, the thiolate and the α-(imino)-*N*-heterocycle.[22,23] As seen in nature, first row transition

metals are used by metalloenzymes to perform essential redox transformations. Thiolates can be oxidized and therefore provide a second redox-active site as well to modulate the redox potentials of the metal.[2,3] Finally the α-(imino)-*N*-heterocycle is part of a growing family of "redox-active ligands" that are more commonly being incorporated into base metal catalysts.[24,25,26] This α-(imino)-*N*-heterocycle backbone can accept up to two electrons on each arm and have characteristic bond lengths depending on the formal oxidation state of the ligand (**Table 2.03**).[23]

Table 2.03: Ligand backbone bond lengths (Å). Average distances of all 4 (α-imine)N-heterocycle arms.

Bond Lengths[a]	10	11	12	Typical L(0)[23]	Typical L(•)[-23]
C-N_{imine}	1.297(3)	1.297(1)	1.297(3)	1.28(1)	1.34(1)
C-C	1.414(3)	1.440(2)	1.427(3)	1.47(1)	1.41(1)
C-$N_{N\text{-}heterocycle}$	1.364(4)	1.352(1)	1.336(8)	1.35(1)	1.39(1)

Unexpectedly, even without the addition of an external reductant, the bond lengths show increased electron density within this organic framework of the imine bond. All three complexes have elongated imine bonds and shortened C-C bonds (**Table 2.03**), which are diagnostic of a partially reduced ligand backbone. While there are other complexes with long imine bonds around (1.29 Å) these ferrous complexes do not have the concurrent short C-C bond; these ferrous complexes C-C bonds are around 1.46 Å.[27,28] This elongation could be caused by either a reduction of the ligand backbone or increased backbonding into the α-(imino)-*N*-heterocycle π^* orbital. Milstein *et al.* have observed an unusual elongation of the imine bond in a similar α-(imino)pyridine complex and they have attributed this to increased backbonding due to the electronic geometry of the metal complexes.[29] However his C-C bond does not show the same decrease in bond length that is observed within this family of thiolate ligated ferrous complexes suggesting there may be more electron density present within this redox-active ligand

framework.[29] While there is a wealth of similar α-(imino)pyridine complexes and other similar "redox-active" ligands, there are few with a coordinated thiolate which could influence both the electronics of the metal and other ligands around the metal center. In one similar instance, Goldberg has also observed unusual bond lengths within the imine arms of a singly reduced bis(imino)pyridine system with a pendent thiolate, suggesting that the thiolates may be able to modulate the electron density of other redox ligands coordinated to the metal center.[30]

*Solution State Structural Analysis of **10**, **11** and **12*:**

A diamagnetic ^{1}H NMR spectrum is expected since the metal-ligand bond lengths are consistent with a low-spin ferrous electronic configuration. Indeed, complexes **10** and **11** do have diamagnetic proton spectra that are consistent with the structural geometry of the complex depending on how the ligand bridges the two iron metal centers (**Figure 2.05**). As seen in the solid state structure, **11** has C_{2h} symmetry, and has two doublets observed at 4.77 ppm (^2J = 15.1 Hz) and 3.88 ppm (^2J = 15.2 Hz) which are assigned to the diasterotopic protons on the four symmetry related methylene carbons adjacent to the imine nitrogens. Additionally the methylene protons adjacent to the thiolate are equivalent by ^{1}H NMR spectroscopy, constituting the singlet resonance at 0 ppm. Finally, each quinoline ring is related by symmetry and as such only 6 unique aromatic protons are observed while the protons on the imine carbon are all symmetry related and are observed as a singlet at 9.8 ppm.

Conversely, since the C_2 symmetric **10** is of lower symmetry, there are more distinct proton environments observed. The protons on the methylene groups adjacent to the imine nitrogen now consist of four unique protons instead of two and they can be observed as a doublet consisting of one of the protons at 4.15 ppm (^2J = 12.7 Hz) and a multiplet containing the other

three protons at 3.77 ppm (**Figure 2.05**). Similarly the protons on the methylene adjacent to the thiolate are now split into two doublets at 0.90 ppm (^2J = 13.3 Hz) and 0.31 ppm (^2J = 13.4 Hz). Since the two aromatic rings on each organic backbone are no longer symmetry related, there are 8 peaks corresponding to the 8 unique aromatic protons. The two imine arms are also chemically inequivalent and the protons on the imine carbon are now two singlets at 9.3 and 9.0 ppm. The splitting patterns in these spectra give evidence that the solid-state structure geometry is maintained in solution.

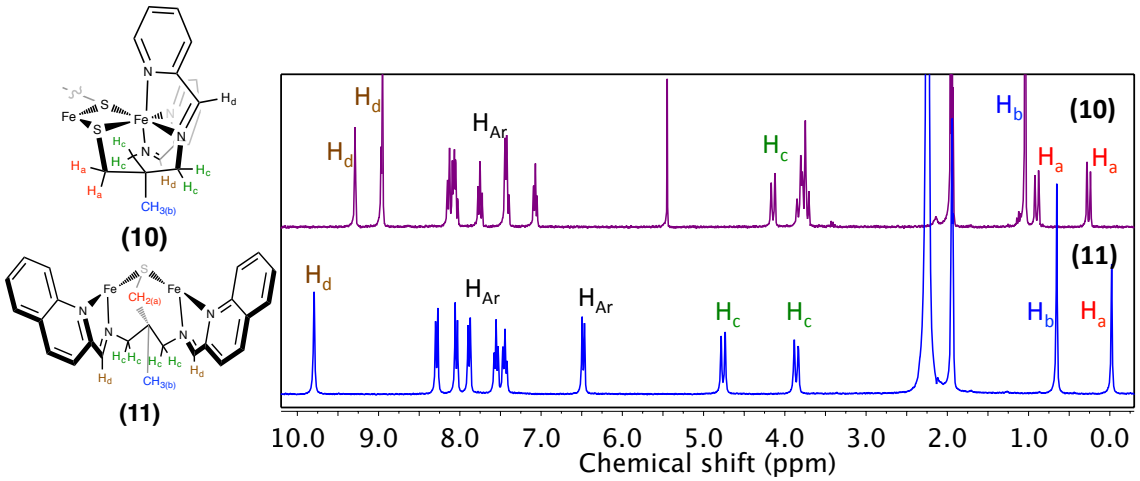

Figure 2.05: ^{1}H NMR spectra of **10** (top) and **11** (bottom) in MeCN-d_3 at 300 MHz and 298 K. Diagrams are showing one half of the dimeric solid state structure as the other half is related by symmetry. H_{Ar} indicates aromatic protons.

However, while a low-spin ferrous metal center would be consistent with the metal-ligand bond lengths, the intra-ligand bond lengths and the diamagnetic ^{1}H NMR spectrum, alternative electronic geometries exist that could also explain these observations. Since α-(imino)pyridine ligands can be reduced, an internal electronic rearrangement wherein the ferrous metal center reduces the ligand backbone would lead to a complex such as Fe(III)-(L)(L$^{\bullet-}$). It would be expected that, in this geometry the solid state structure would have two asymmetric imine arms according to the oxidation state of each ligand, but Wieghardt has observed with Fe

that the radical can be delocalized across both α-(imino)pyridine arms leading to bond lengths halfway between a closed shell ligand and a reduced ligand.[23] These bond lengths match the bond lengths observed for **11**. Additionally, Wieghardt has reported strong antiferromagnetic coupling between a singly reduced α-(imino)pyridine and a paramagnetic metal center with coupling constants ranging from J = -330 to -1370 cm^{-1}.[23] As such the diamagnetic ^{1}H NMR spectra do not discount this electronic configuration.

While the structure of **12** has similar bond lengths to the other two complexes, the ^{1}H NMR spectrum is distinct. This spectra contains a mixture of paramagnetic and diamagnetic features, indicating that a mixture of species is present in solution. As observed in the solid state, the Fe-S bonds for **12** are asymmetric which may lead to the cleavage of the dimeric solid-state structure. If the solid-state dimer were to cleave, it would be expected that the corresponding five-coordinate monomeric species may have a different metal spin state due to the geometry and could lead to the paramagnetic features. A solution-state effective magnetic moment was evaluated over a range of temperatures by using the Evans method and it clearly shows an increase as a function of temperature deviating from Curie's law, suggesting the possibility of a monomer-dimer equilibrium in solution (**Figure 2.06**). If the solid-state dimer were to cleave a monomeric species may be paramagnetic. The ratio of these two would depend on the temperature dependent equilibrium constant (K_{eq}) giving rise to the variation of μ_{eff} on temperature. The possibility of a monomeric species in solution is further supported by this complex's reactivity with O_2.

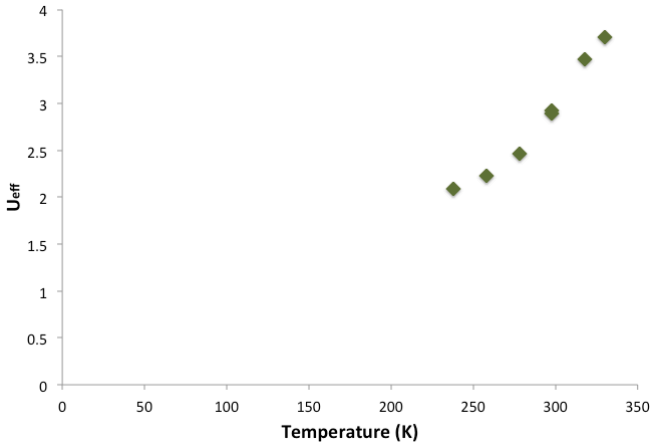

Figure 2.06: Evans method of **12** indicating an effective magnetic moment dependence of temperature: in MeCN-d_3

*Electronic Absorption Spectra of **10, 11** and **12**:*

The electronic absorption spectra of all three of these complexes show intense visible features. These features have very large extinction coefficients, which suggests that these transitions are not ligand field transitions in nature, but charge transfer transitions (**Figure 2.07, Figure 2.08** and **Table 2.04**). Thiolate ligated Fe complexes typically contain intense ligand to metal charge transfers (LMCT) due to the covalent thiolate bond and initially it was hypothesized that these transitions were a result of this type of transition.[2,10] However, typically our group observes these strongly visible features only when the metal is oxidized to the ferric oxidation state. This could lend confidence to the hypothesis of the electronic rearrangement wherein the correct electronic configuration would consist of an Fe(III)-(L)($L^{\bullet-}$). However, the nature of the charge transfer is due to the low lying π^* ligand orbitals of the α-(imino)pyridines which will be seen in the electronic absorption spectra.[31] This will be further evaluated in Chapter 3.

It should be noted that in solution **12** contains two species, one diamagnetic and one paramagnetic, convoluting the analysis of the extinction coefficients. This mixture has a solution

μ_{eff} of 2.9 μ_B at 298 K by Evans (**Equation 2.01**). This is close to the value for an S=1 system (μ_{eff} of 2.9 μ_B). This would suggest that the paramagnetic species has high spin S=2 and a solution of 100% of this species would should have a μ_{eff} of 4.9 μ_B. The experimental magnetic moment would therefore indicate that the solution consists of 35% paramagnetic species while 65% is diamagnetic species at 298 K.[32] Using this information, K_{eq} of the monomer-dimer equilibrium at room temperature is 0.0034 M for a solution containing 9.1 mM of Fe (**Equation 2.02**). The relative concentrations of monomer and dimer were then determined for the more dilute UV-Vis samples using this equilibrium constatnt. By varying these concentrations of iron between 0.228 mM to 0.055 mM they can be used to solve for the extinction coefficients of both species. The monomeric species therefore has a molar absorptivity of 6,100 M^{-1} cm^{-1} at 619 nm, while the dimer has a molar absorptivity of 12,400 M^{-1} cm^{-1} at 619 nm (**Equation 2.03**).

$$FeTIM_{dimer} \rightleftharpoons 2\ FeTIM_{monomer} \qquad \text{(eq 2.01)}$$

$$K_{eq} = \frac{[Monomer]^2}{[Dimer]} \qquad \text{(eq 2.02)}$$

$$Abs_{619} = \varepsilon_{monomer} * [Monomer] + \varepsilon_{dimer} * [Dimer] \qquad \text{(eq 2.03)}$$

Table 2.04: UV-Vis transitions for complexes **10, 11** and **12** in MeCN RT.

	λ_{max} **(nm)**(ε **($M^{-1}cm^{-1}$)**
10	**420 (6,150), 580 (9,100), 650 (11,800)**
11	**420 (6,240), 607 (14,830), 719 (19,500)**
12 (monomer)	**619 (6,100)**
12 (dimer)	**619 (12,400)**

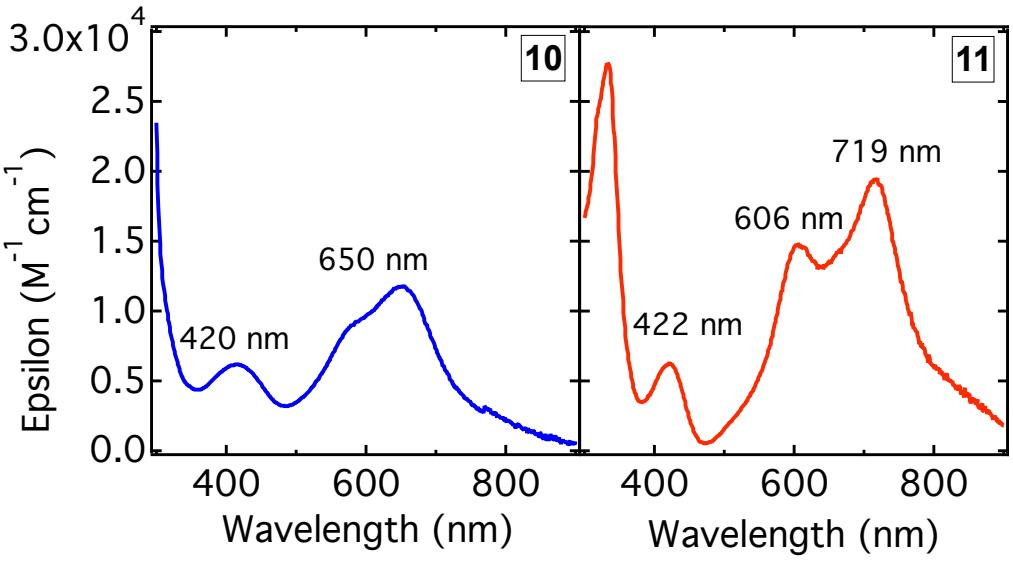

Figure 2.07: Electronic absorption spectra of **10** and **11** at RT in MeCN**.**

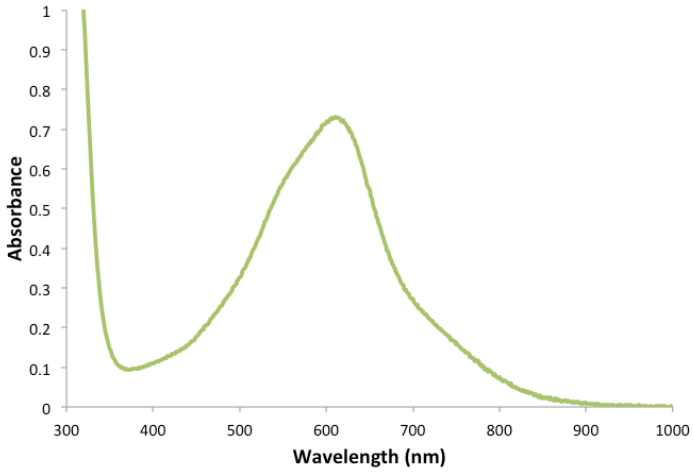

Figure 2.08: Electronic absorption spectra of **12** consiting of 0.114 mM of a proposed monomeric complex and 0.003 mM concentration of a diamagnetic dimeric complex in MeCN at RT.

Intense, low-energy charge transitions are a hallmark of Fe complexes bearing reduced, conjugated ligands. Assigned as ligand-to-ligand charge transfer (LLCT) transitions, the λ_{max}– values are typically in the near infrared region, and extinction coefficients are in excess of 10^4 $M^{-1}cm^{-1}$.[22,23,33,34] In contrast, closed shell L^0 (α-imino)pyridine-ligated iron complexes have Fe→π^* metal to ligand charge transfer (MLCT) bands with extinction coefficients that range from 700-

6000 M^{-1} cm^{-1} and λ_{max}–values in the range 408-600 nm.[19,22] Thus, the large extinction coefficients of **1-3** are more consistent with features expected from a reduced ligand moiety. However, the presence of thiolate ligands has been shown to significantly influence the intensity of MLCT bands to unoccupied π^* ligand orbitals.[35,36] It is therefore possible that the large extinction coefficients found for **10-12** instead reflect enhancement of the MLCT transitions as a result of covalent thiolate donation and will be discussed in full in Chapter 3.

*Reactivity With Small Molecules***:**

While changing the *N*-heterocycle did not produce any desired solid state monomeric species, these could be obtained by the addition of strongly coordinating small molecules. Both **10** and **12** react with $CO_{(g)}$ and this transformation can be monitored by both ^{1}H NMR and ^{13}C NMR spectroscopy. **10** will react with 5 atm of $CO_{(g)}$ in 12 hours but the identification of a single product is difficult with ^{1}H NMR spectroscopy. However, a major product is observed by ^{13}C NMR spectroscopy (**Figure 2.09**). A very small peak at 215 ppm may be the bound CO carbon while the peak at 185 ppm seems to be consistent with free $CO_{(g)}$. The pattern of the NMR peaks suggests that a similar ligand geometry is maintained. With 5 aliphatic peaks it seems that the two imine arms are inequivalent by NMR spectroscopy. Ten aromatic proton peaks are observed which is two fewer than expected. The two missing peaks may be masked by the MeCN (solvent) peak. The number of peaks suggests that the imine arms are inequivalent, and if the $CO_{(g)}$ binds it will be in the position vacated by the bridging thiolate and be *cis* to the remaining thiolate. Upon removal of the CO atm the complex will revert back to the starting dimeric species. This can then be repressurized to reform the CO bound product.

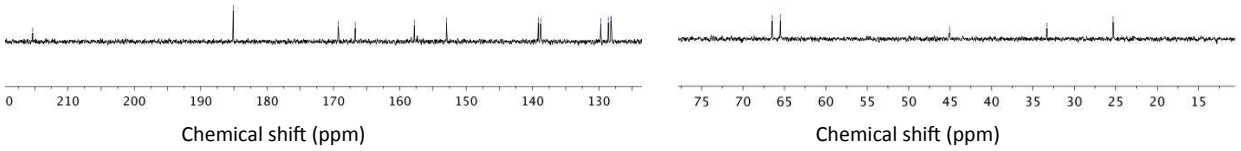

Figure 2.09: ^{13}C NMR spectrum downfield (left) of **10** with the addition of 5 atm $CO_{(g)}$, ^{13}C NMR spectrum upfield (right) in MeCN-d_3.

12 reacts much faster than **10** with 5 atm of $CO_{(g)}$; a noticeable change in the ^{1}H and ^{13}C NMR spectrum in MeCN-d_3 is observed immediately after pressurization. While there are still small paramagnetic peaks present, there is a change in the diamagnetic region. If the $CO_{(g)}$ were to bind *cis* to the thiolate, this six coordinate complex would most likely be low-spin, thus giving rise to a diamagnetic spectrum (**Figure 2.10**). Although the aliphatic region contains many peaks, there do seem to be six unique peaks in the aromatic region (**Figure 2.10**). These six peaks represent the four protons on the two asymmetric imidazole rings along with the two imine protons. Similar to **10**, the ^{13}C NMR of **12** seems to only have one major species present. In the aliphatic region all peaks are accounted for including a weak signal at around 45 ppm could be the quaternary carbon of the ligand backbone. Downfield there is a weak signal observed at 218 ppm which is likely the bound CO. There are 7 other peaks but it would be expected to have eight: three carbons within each the imidazole, and the two imine carbons. Two peaks could be too close to each other to resolve or the MeCN solvent peak could mask the last signal. Upon releasing the pressure this complex releases CO and reverts back to the starting species.

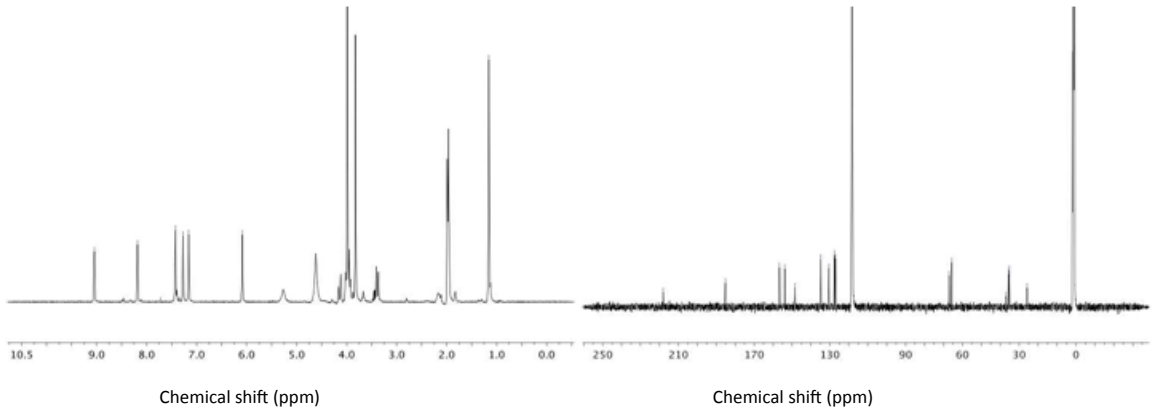

Figure 2.10: ^{1}H NMR spectrum (left) of **12** with the addition of 5 atm $CO_{(g)}$, ^{13}C NMR spectrum of same reaction on right in MeCN-d_3.

The stronger binding, anionic CN^- substrate will also cleave the dimer but binds strongly enough to isolate a solid sample. This complex can be synthesized by adding one equivalent of NaCN at the completion of the metal templated Schiff base condensation instead of the usual non-coordinating counterion ($NaPF_6$ or $NaBPh_4$). Using **10**, a new product is observed by ^{1}H NMR suggesting that CN is bound (**Figure 2.11**). In accord with the eight unique aromatic protons, this indicates that the complex would have two asymmetric α-(imino)pyridine arms. The aliphatic region still has a doublet 4.7 ppm and a multiplet 3.8 ppm due to the four protons on the methylene carbons adjacent to the imine. The methyl group on the tame backbone has a large singlet at 1.2 ppm however it seems the two methylene protons adjacent to the thiolate are obscured by the MeCN peak. These protons do indeed appear when the solvent is changed from MeCN-d_3 to CD_2Cl_2 at 2.10 and 2.0 ppm. Indeed, the ^{13}C NMR in MeCN-d_3 confirms that there is one major product with 15 signals. Unfortunately the cyanide complex is not stable and even isolated as a solid will decompose within days at RT in an inert atmosphere. The strong binding

of cyanide could lead to the leaching of the Fe metal center and decomposition of the desired complex.

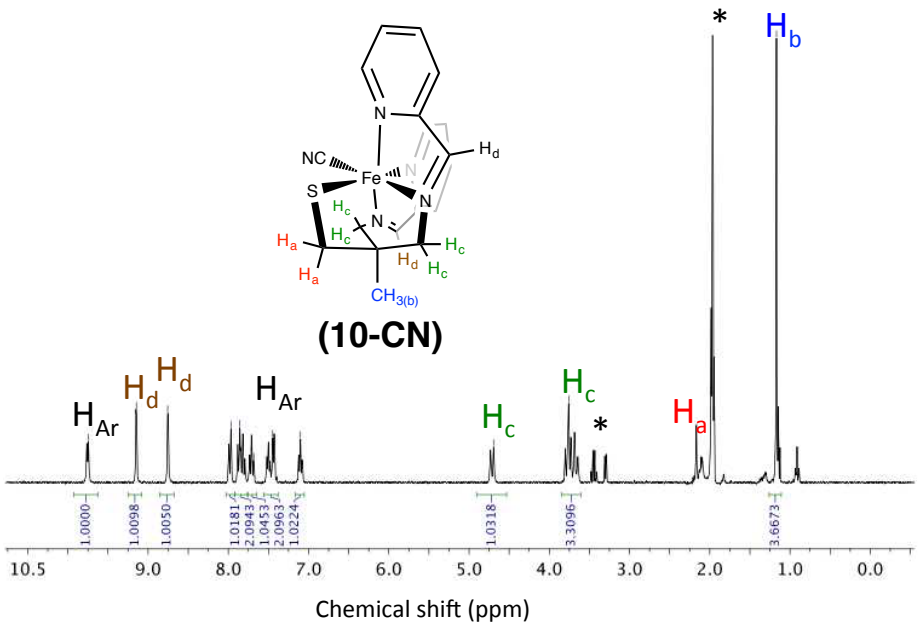

Figure 2.11: ^{1}H NMR spectrum of **10-CN** in MeCN-d_3.

In addition to NMR spectroscopy, a strong CN stretching feature should be observed by infrared (IR) spectroscopy if CN^- is part of this complex. Indeed, in a solution of CH_2Cl_2 a peak for the CN^- stretch is observed at 2087 cm^{-1}. This is in the region that would be expected if CN^- were to be bound to the ferrous metal center. Que has observed a CN stretch at 2101 cm^{-1} for a ferrous CN complex and "free" CN is expected to be 2052 cm^{-1}.[37] When the CN is isotopically enriched with ^{13}C the expected decrease in stretching frequency to 2044 cm^{-1} is observed, consistent with Hooke's law (**Figure 2.12**).

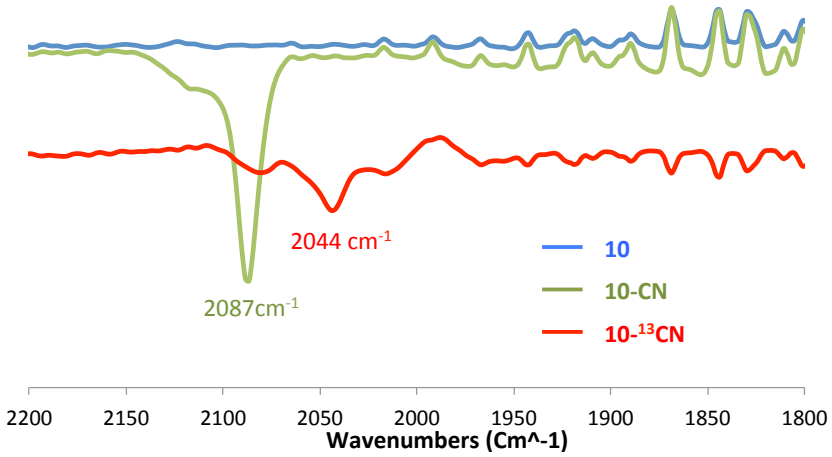

Figure 2.12: FT-IR spectra of **10** (Blue), **10-CN** (green) and isotopically labeled **10-^{13}CN** (Red). Solution IR DCM.

The identity of this complex was unambiguously identified by the isolation of a single crystal (**Figure 2.13**). Unlike the complexes isolated with less coordinating solvents, this forms as a monomer in the solid state. The CN is bound *cis* to the thiolate and in agreement with the NMR spectrum. Although this shows that a monomer may not form with an apical thiolate *trans* to the open site as was the starting goal of this project, it does indicate that some of these dimers may be cleaved.

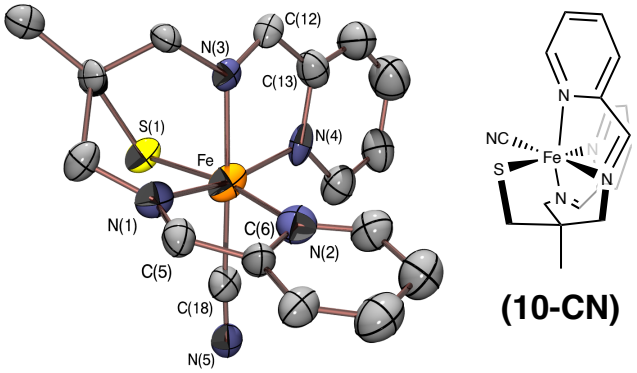

Figure 2.13: Crystal structure of **10-CN** (left). Elipsoids at 50% probability. Hydrogens and solvent atoms are omitted for clarity. Corresponding structural representations (right).

Similar to the dimeric complexes, this complex seems to have bond lengths consistent with a low-spin metal center, which would be expected with the coordination of a strong field

ligand such as CN^-. The Fe-N bond lengths range from 1.916(9)-1.968(9) Å while the Fe-S bond is short at 2.287(9) Å (**Table 2.05**). Since this has a lower spin-state than that reported by Lawrence Que, a shorter Fe-C bond at 1.945(11) Å is observed in **10-CN,** compared to Que's which has a bond length of 2.21293 Å.[28] In agreement with the weaker CN^- stretching frequency compared to Que's, we observe a lengthening of the C-N bond length by 0.014(Å). A weaker and longer C-N bond is expected due to the more significant backbonding in **10-CN** compared to Que. The lower spin state of **10-CN** will populate the t_{2g}-like orbitals which are capable of backbonding into the π^* orbitals of the CN substrate. Additionally the strongly covalent thiolate will increase the electron density of the metal and as such increase the metals ability to backbond.

Table 2.05: selected bond distances (Å) for **10-CN**.

Metal-Ligand Bond Lengths	Distance (Å)
Fe-S(1)	2.287(9)
Fe-N(1)	1.932(9)
Fe-N(2)	1.961(10)
Fe-N(3)	1.916(9)
Fe-N(4)	1.968(9)
Fe-C(18)	1.945(11)
Intra-Ligand Bond Lengths	
C(18)-N(5)	1.164(12)
N(1)-C(5)	1.308(12)
C(5)-C(6)	1.410(15)
N(3)-C(12)	1.290(12)
C(12)-C(13)	1.402(14)

While the metal-ligand bond lengths are comparable between **10-CN** bound and **10**, there are some noticeable differences in the intra-ligand bond lengths. With the CN coordinated to the Fe, the two α-(imino)pyridine arms do have distinct intra-ligand bond lengths. The imine that is *trans* to the cyanide has a much shorter imine bond at 1.290(12) Å compared to the imine *cis* to the CN, which now lengthens to 1.308(12) Å. Both arms have relatively short C-C bonds at

1.402(14) Å and 1.410(15) Å, respectively. The removal of a π-donating thiolate for a strongly π-accepting CN will perturb the t_{2g}-like orbitals and the CN^- should have a stronger interaction with the imine arm coordinated *trans* to the CN. As such the CN may influence the electron density in this plane and lessen the amount of electron density within the imine arm compared to the dimeric structure.

Although a crystal structure has been obtained for the pyridine derivative, this complex is not stable and decays over a couple days while in solution, as monitored by ^{1}H NMR spectroscopy. In a similar fashion the **12-CN** can be observed but seems to decay faster than the pyridine moiety. The strongly coordinating CN could lead to the decomposition of these species. In contrast the C_{2h} symmetric **11** shows no affinity for these small molecules. This is most likely due to the different bridging mode that prevents easy coordination of small molecules to the metal center.

*Reactivity With Dioxygen***:**

Our group has previously shown that thiolate ligation to ferrous complexes lowers the reduction potential and increases its affinity to bind and reduce O_2.[38,39] These three complexes react distinctly with this oxidant; the divergence in reactivity is most likely dependent on the solution state structure of each complex. Akin to its reactivity with small substrates, **11** is inert to O_2 and is stable for months. In contrast, **10** reacts slowly with O_2 (over the course of several hours) while **12** reacts within minutes, which is similar to our group's other monomeric thiolate ligated ferrous complexes.

The reaction between **12** and O_2 can be easily monitored by the disappearance of the charge transfer band at 619 nm (**Figure 2.14**). This reaction takes 5 minutes to fully convert and

leaves a small feature at 539 nm. The intensity is much lower than that of the starting band. If the ferrous metal is being oxidized, a thiolate to metal charge transfer should be observed in the visible region. However ESI-MS indicates a small peak that is +32 AMU and could suggest a doubly oxygenated sulfur product. Investigations are ongoing to determine the identity of this product.

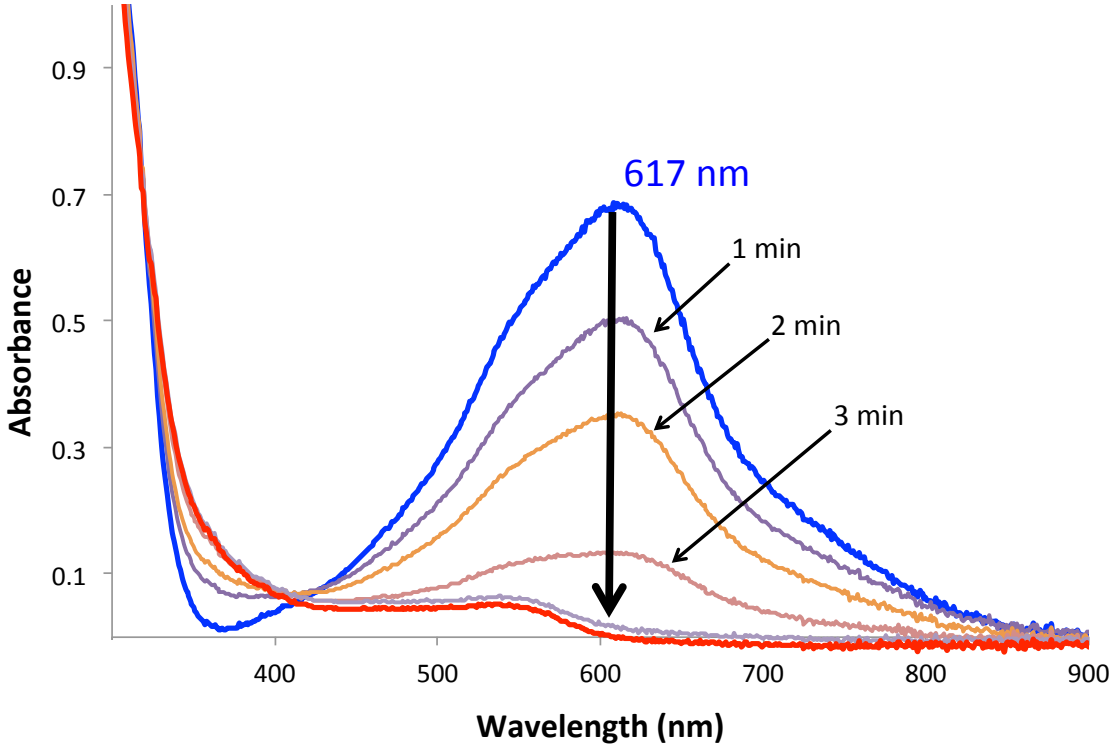

Figure 2.14: Reaction between **12** and O_2 at RT in MeCN 0.045mM. Scans taken at 1 min intervals.

While this reaction is complete within minutes at RT, the reaction takes longer at -15°C (**Figure 2.15**). With no observable intermediates it would be likely that the rate determining step (RDS) of this reaction is O_2 reacting with the ferrous starting material. With excess O_2, the expected pseudo first-order kinetic fit for the disappearance of the starting material (**Figure 2.15**). An induction period is observed but is likely a result of O_2 dissolution into the solvent. The similar fast reactivity with O_2 compared with other monomeric thiolate ligated ferrous

complexes further supports the hypothesis that a significant portion of **12** consists of a monomeric ferrous thiolate in solution as observed with the paramagnetic ^{1}H NMR spectrum.

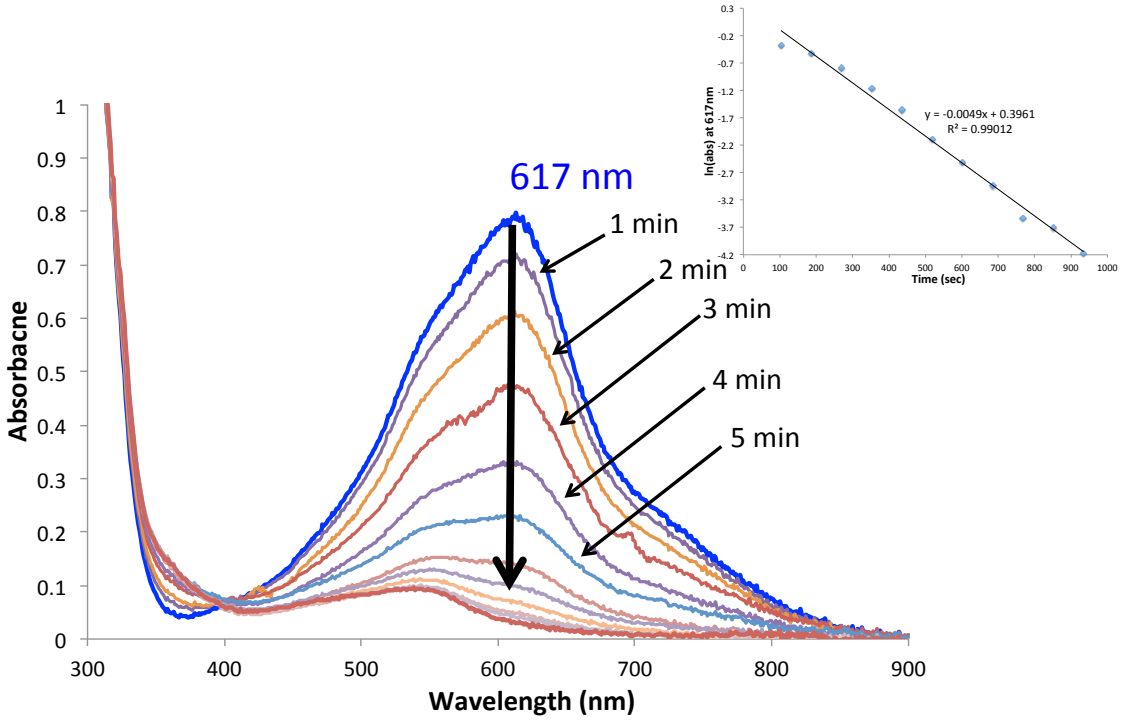

Figure 2.15: Reaction between **12** and O_2 at -15°C in MeCN (0.045mM). Inset shows pseudo-first order dependence. Scans taken at 1 min intervals.

While the ^{1}H NMR spectra of **10** supports a solution state dimer consistent with the solid state structure, this species will still react with O_2. Similar to **12**, the reaction can be monitored by UV-Vis through the disappearance of the main charge transfer transition at 640 nm. This reaction takes about 12 hours at RT and the product of this reaction has a weaker feature at 560 nm. This rate can be increased by raising the temperature, but there are no observable intermediates. The reaction appears to be pseudo zeroth-order with respect to the ferrous complex however at higher temperatures the reaction becomes pseudo-first order (**Figure 2.16**). The much slower reactivity could be due to the fact that O_2 binds less easily with less facile oxidation at the ferrous metal center as the dimeric solid state structure seems to be retained in solution. Alternatively, there may also be an equilibrium between a monomer and dimer for the

10 as well but, unlike **12,** it is almost exclusively favored toward the dimer. This leaves only a small portion of complex that is capable of reacting with O_2. As this monomeric species is consumed it will push the equilibrium to favor the monomeric species. This gradual build-up of monomeric species could be why the reactivity is so much slower for **10** than **12**.

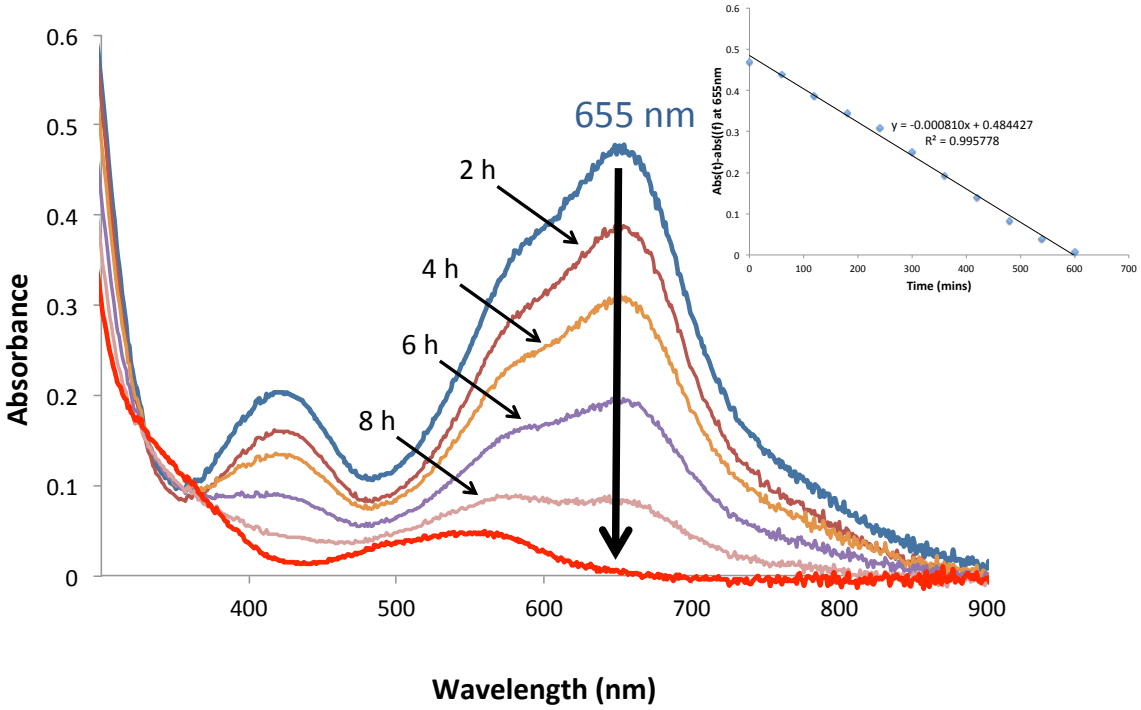

Figure 2.16: Reaction between **10** and O_2 at RT in MeCN. Inset shows zeroth order dependence. Scans taken at 2 hour intervals.

Conclusions:

A novel tameN_2S backbone has been used to synthesize three different ferrous species. All three form solid state dimers with bridging μ-thiolates with bond lengths that are consistent with a low-spin ferrous metal center. The condensation of an *N*-heterocyclic arms affords a unique redox-active ligand arm with unusual ligand bond length perturbations. The bond lengths seem to indicate that there is an increase in electron density present in the ligand backbone. The

activation of this ligand could be due to a metal spin state that is favorable for backbonding to the π^* α-imino-*N*-heterocycle. In addition, the inclusion of the π-donating thiolate can increase and "push" electron density into the α-(imino)-*N*-heterocycle orbitals.

The diamagnetic ^{1}H NMR spectra of **10** and **11** indicate that the solid state structure seems to be retained in solution. However, it seems that the paramagnetic solution state properties of **12** indicate that in coordinating solvents (MeCN and MeOH), this species will cleave and potentially form a monomeric complex. Indeed, its reactivity in solution with O_2 is similar to other monomeric ferrous thiolates which further confirms that a monomeric species is indeed present in solution. The O_2 reaction product has not been fully characterized but does seem to be a ferric thiolate complex due to a visible charge transfer which is most likely a sulfur to Fe(III) charge transfer. Although no intermediates were observed in this reaction, fully characterizing the final product may yield a better understanding of how this reaction proceeded.

Unlike most previously prepared ferrous thiolates in our group, which have few visible features, these three complexes contain significant charge transfer transitions with large extinction coefficients. The nature of these charge transfers will be discussed in Chapter 3 but seem to include all three of the redox-active functionalities in these molecules. The dimeric structure of the **10** and **12** can be cleaved by the addition of strongly coordinating substrates such as $CO_{(g)}$ and CN^-. It would be interesting to investigate these further as well as other biologically relevant substrates. One promising result could be achieved by treating **10** and **12** with $NO_{(g)}$.

Notes to Chapter 2

1. Leipzig, B. K.; Rees, J. A.; Nyrov, A.; Theisen, R.; Flowers, S. E.; Kaminsky, W.; DeBeer, S.; Kovacs, J. A. *In Preparation*

2. Holm R. H.; Kennepohl P.; Solomon E. I. *Chem. Rev.* **1996**, *96*, 2239-2314.

3. Kovacs, J. A. *Chem. Rev.* **2004**, *104*, 825–848.

4. Kovacs, J. A.; Brines, L. M. *Acc. Chem. Res.* **2007**, *40*, 501–509.

5. Shearer, J.; Nehring J.; Lovell, S.; Kaminsky, W.; Kovacs, J. A. *Inorg. Chem.* **2001**, *40*, 5483-5484.

6. Shearer, J.; Scarrow, R. C.; Kovacs, J. A. *J. Am. Chem. Soc.* **2002**, 11709-11717.

7. Rodrigues, J. V.; Abreu, I. A.; Cabelli, D.; Teixeira, M. *Biochemistry* **2006**, *45*, 9266-9278.

8. Yeh, A. P.; Hu, Y; Jenney, F. E.; Adams, M. W.; Rees, D. C. *Biochemistry* **2000**, *39*, 2499–2508.

9. Kitagawa, T.; Dey, A.; Lugo-Mas, P.; Benedict, J. B.; Kaminsky, W.; Solomon, E. I.; Kovacs, J. A. *J. Am. Chem. Soc.* **2006**, *128*, 14448-14449.

10. Mathé, C.; Mattioli, T. A.; Horner, O.; Lombard, M.; Latour, J.; Fontecave, M.; Nivière, V. *J. Am. Chem. Soc.* **2002**, *124*, 4966-4967.

11. Theisen, R. M. Synthetic Models and Reactivity of Sulfur-Ligated Iron Metalloenzymes, University of Washington, 2005.

12. Lugo-Mas, P.; Taylor, W.; Schweitzer, D.; Theisen, R. M.; Xu, L.; Shearer, J.; Swartz, R. D.; Gleaves, M. C.; DiPasquale, A.; Kaminsky, W.; Kovacs, J. A. *Inorg. Chem.* **2008**, *47*, 11228–11236.

13. Altomare, A.; Cascarano, G. L.; Giacovazzo, C.; Guagliardi, A. *J. Appl. Crystallogr.* **1993**, *26*, 343–350.

14. Altomare, A. Burla, C. Camalli, M., Cascarano, G. L., Giacovazzo, C. Guagliardi, A., Moliterni, A. G. G., Polidori, G., Spagna, R. *J. Appl. Crystallogr.* **1999**, *32*, 115–119.

15. Sheldrick, G. M. SHELXL-97: Program for the Refinement of Crystal Structures, University of Göttingen, Germany, 1997.

16. Mackay, S.; Edwards, C.; Henderson, A.; Gilmore, C.; Stewart, N.; Shankland, K.; Donald, A. University of Glasgow, Scotland 1997.

17. Waasmaier, D.; Kirfel, A. *Acta Crystallogr. A.* **1995**, *51*, 416–430.

18. Jackson, H. L.; Shoner, S. C.; Rittenberg, D.; Cowen, J. A.; Lovell, S.; Barnhart, D.; Kovacs, J. A. *Inorg. Chem.* **2001**, *40*, 1646–1653.

19. Brines, L. M.; Shearer, J.; Fender, J. K.; Schweitzer, D.; Shoner, S. C.; Barnhart, D.; Kaminsky, W.; Lovell, S.; Kovacs, J. A. *Inorg. Chem.* **2007**, *46*, 9267-9277.

20. Roelfes, G.; Vrajmasu, V.; Chen, K.; Ho, R. Y. N.; Rohde, J.; Zondervan, C.; la Crois, R. M.; Schudde, E. P.; Lutz, M.; Spek, A. L.; Hage, R.; Feringa, B. L.; Münck, E.; Que, L. *Inorg. Chem.* **2003**, *42*, 2639-2653.

21. Widger, L. R.; Davies, C. G.; Yang, T.; Siegler, M. A.; Troeppner, O.; Jameson, G. N. L.; Ivanović-Burmazović, I.; Goldberg, D. P. *J. Am. Chem. Soc.* **2014**, *136*, 2699–2702.

22. Lu, C. C.; Weyhermüller, T.; Bill, E.; Wieghardt, K. *Inorg. Chem.* **2009**, *48*, 6055–6064.

23. Lu, C. C.; Bill, E.; Weyhermüller, T.; Bothe, E.; Wieghardt, K. *J. Am. Chem. Soc.* **2008**, *130*, 3181-3197.

24. Chirik, P. J.; Wieghardt, K. *Science* **2010**, *327*, 794-795.

25. Bouwkamp M. W.; Bowman, A. C.; Lobkovsky, E.; Chirik, P. J. *J. Am. Chem. Soc.* **2006**, *128*, 13340-13341.

26. Wu, J. Y.; Stanzl, B. N.; Ritter, T. *J. Am. Chem. Soc.* **2010**, *132*, 13214–13216.

27. Nienkemper, K.; Kotov, V. V.; Kehr, G.; Erker, G.; Fröhlich, R. *Eur. J. Inorg. Chem.* **2006**, *2006*, 366–379.

28. Vedder, C.; Schaper, F.; Brintzinger, H.-H.; Kettunen, M.; Babik, S.; Fink, G. *Eur. J. Inorg. Chem.* **2005**, 1071–1080.

29. Butschke, B.; Fillman, K. L.; Bendikov, T.; Shimon, L. J. W.; Diskin-Posner, Y.; Leitus, G.; Gorelsky, S. I.; Neidig, M. L.; Milstein, D. *Inorg. Chem.* **2015**, *54*, 4909–4926.

30. Widger, L. R.; Jiang, Y.; Siegler, M. A.; Kumar, D.; Latifi, R.; de Visser, S. P.; Jameson, G. N. L.; Goldberg, D. P. *Inorg. Chem.* **2013**, *52*, 10467–10480.

31. Shejwalkar, P.; Rath, N. P.; Bauer, E. B. *Dalton Trans.* **2011**, *40*, 7617-7631.

32. Huang, Y.-P.; Kassner, R. J. *J. Am. Chem. Soc.* **1979**, *101*, 5807–5810.

32. Chłopek, K.; Bill, E.; Weyhermüller, T.; Wieghardt, K. *Inorg. Chem.* **2005**, *44*, 7087-7098.

33. Ghosh, P.; Bill, E.; Weyhermüller, T.; Wieghardt, K. *J. Am. Chem. Soc.* **2003**, *125*, 3967-3979.

34. Gale, E. M.; Narendrapurapu, B. S.; Simmonett, A. C.; Schaefer, H. F.; Harrop, T. C. *Inorg. Chem.* **2010**, *49*, 7080–7096.

35. Broering, E. P.; Dillon, S.; Gale, E. M.; Steiner, R. A.; Telser, J.; Brunold, T. C.; Harrop, T. C. *Inorg. Chem.* **2015**, *54*, 3815–3828.

36. England, J.; Farquhar, E. R.; Guo, Y.; Cranswick, M. A.; Ray, K.; Münck, E.; Que, L. *Inorg. Chem.* **2011**, *50*, 2885–2896.

37. Theisen, R. M.; Shearer, J.; Kaminsky, W.; Kovacs, J. A. *Inorg. Chem.* **2004**, *43*, 7682-7690.

38. Toledo, S. A. Synthesis and Reactivity of an Expanded Family of Superoxide Reductase (SOR) Model Complexes Using N-Heterocyclic, Thiolate Containing Ligands: Towards a Better Understanding of Structural-Functional Relationships, University of Washington, 2009.

Chapter 3.

Spectroscopic Insight Into a Thiolate *cis*-Type "Push Effect" and its Influence on Auxiliary Redox-Active Ligands.

Portions of this chapter have been adapted from: Leipzig, B. K.; Rees, J. A.; Nyrov, A.; Theisen, R.; Flowers, S. E.; Kaminsky, W.; DeBeer, S.; Kovacs, J. A. *In Preparation*.[1]

Introduction:

Cytochrome P450 has inspired a wealth of synthetic models containing redox-active ligands.[2] Nature has engineered this enzyme to make use of an organic based reductant in the form of a porphyrin and an axial thiolate.[3] This affords the heterolytic O-O bond cleavage of compound 0 and the generation of the high-valent ($Por/S_{cys}^{\bullet}$)Fe(IV)=O.[4,5] This additional redox reservoir expands the formal oxidation states available for this enzyme but also affords the potential to do the necessary direct $2e^-$ redox reactions.

Numerous synthetic models have been prepared in an attempt to mimic this integral property of cytochrome P450. Performing $2e^-$ chemical conversions is desirable because this is the required amount of electrons needed to execute both bond making and bond breaking transformations. These transformations are commonly observed with 2nd row transition metals, which generally undergo oxidative addition and reductive elimination to make and break bonds.[6] The redox-active ligand portion of these complexes expands $2e^-$ chemistry to earth-abundant 1st row transition metal complexes which tend to undergo sequential $1e^-$ redox processes.

A necessary feature of these complexes is the ability to modulate the redox-potentials of both the metal and ligand to make all redox-reservoirs accessible. This is typically accomplished with high energy filled π orbitals or low energy empty π^* orbitals.[7,8] However, many of these complexes do not incorporate a thiolate which is essential in generating and stabilizing compound I. The axial cysteinate is proposed to help modulate electron density of both the radical, and the peroxo σ^*, suggesting it could also regulate the electron density of these redox active ligands.

Exploring the effects of ancillary ligands on reduction potentials and the reactivity of redox-active ligands can aid the design of second-generation catalysts. As explained in the

introductory chapter, these redox-active ligands can accept electron density to mitigate the electronic demands at the metal center.[9] The addition of a coordinated thiolate or other supporting ligand could help tune the electronic demands and modulate the redox-potentials of these complexes even further. Additionally, the size and electronics of the π^* systems can be tuned to alter the properties of these ligand frameworks.

Experimental:

General considerations: ^{1}H NMR spectra were obtained on a Bruker AV300, AV301, DRX499, or AV500. Chemical shifts are listed in parts per million and were reported relative the residual protio solvent. UV/Vis spectra were recorded on a Varian Cary 50 spectrophotometer equipped with a fiber optic cable connected to a "dip" ATR probe (C-technologies). A custom-built two-neck solution sample holder equipped with a threaded glass connector was sized specifically to fit the "dip" probe. Electrospray ionization mass spectrometry (ESI-MS) was performed on a Bruker Esquire LC-Ion Trap. Electron paramagnetic resonance (EPR) spectra were recorded on a Bruker E580 CW-EPR spectrometer operating at X-band frequency between 4 and 10 K with an Oxford helium cryostat. EPR spectra were collected with the following spectrometer parameters: frequency 9.396 GHz, power=2.008 mW, attenuation=20 dB sweep width=6,000 G, gain=1x10^3, conversion time 5.4 ms, time constant=5.4 ms. Spectra were fit using EasySpin. Cyclic voltammograms were recorded in MeCN (0.1M ^{n}Bu$_4$N[PF$_6$] supporting electrolyte) on a PAR 263A potentiostat or a CHI 600E electrochemical work station using a glassy carbon working electrode, platinum auxiliary electrode and an $Ag^+/AgNO_3$ reference electrode. X-ray crystallographic data was recorded on a Bruker APEX II single crystal X-ray diffractometer

using Mo-radiation. All manipulations were performed using Schlenk techniques or under a N_2 atmosphere in a glovebox.

Synthesis of $[(Fe^{III}(Tame\text{-}N_2SIm_2))_2](PF_6)_4$ (12^{ox}): **12** (50 mg, 0.048 mmols) was added to MeCN (5 mL). To this $FcPF_6$ (0.033 g, 0.096 mmols) was added as a solid. The solution changed from a deep blue to a reddish brown color and was stirred for 15 hours. The solvent was removed and Et_2O (3 x 4 mL) was added. The solution was filtered and the filtrate and the Fc product discarded. The solid was washed with DCM (2 x 3 mL) and then redissovled in MeCN (1 mL) and layered with Et_2O (3 mL) to obtain X-ray diffraction quality crystals. **12^{ox}** was obtained in 47% yield (30mg, 0.023mmol)

Sulfur K-edge X-Ray Absorption Spectroscopy: The samples were taken at beam line ID26 at the ESRF using a double crystal Si(111) monochromator. X-Ray size was 250μm (H) x 50μm (V). A Si PIN diode was fixed above the analyzer crystal to allow for additional XANES measurements in total fluorescence yield (TFY). Both the sample and the spectrometer were mounted in a vacuum chamber and kept at about 10^{-6} mbar. Solid samples of **10-12** were diluted in boron nitride and fixed on an aluminum plate by a double sided carbon tape. A 5μm thick polypropylene foil was put on the sample surface to prevent the samples from air during sample mounting. Prior to RIXS measurements, **10-12** were found to be stable for up to 8 minutes of X-ray exposure time by additional XANES measurements. Consequently, RIXS planes were collected in about 100 minutes at different sample positions to exclude radiation damage.

Computational Methods: All calculations were performed using the ORCA quantum chemistry package developed by Neese and coworkers.[10] All calculations employed the def2-TZVP(-f) basis set and the def2-TZVP/J auxiliary basis set for Coulomb fitting, the atom-pairwise dispersion correction of Grimme (D3BJ),[11,12] and tight convergence criteria were required for the SCF solutions. All calculations used the Grid5 (GridX5) integration grid size, the zeroth-order regular approximation (ZORA),[13] and the conductor-like screening model (COSMO)[14] with acetonitrile as a solvent. Geometries were optimized for all complexes using the BP86 functional with the resolution of the identity (RI) approximation, and initiated from crystallographic coordinates when available.[15,16] The calculation was converged to tight optimization criteria. Selected calculations employed the broken-symmetry formalism to model coupled paramagnetic sites. For the calculation of ^{57}Fe Mössbauer parameters, the specialized core properties basis set (CP-PPP) with an integration grid of 7 was selected for Fe. The quadrupole splitting parameters were obtained from the output of the calculation, and the calculated isomer shifts were determined using the calibration study of Römelt et al.[17] Time-dependent DFT (TD-DFT) calculations utilized the same parameters but with the CAM-B3LYP[18] range-separated hybrid density functional and the RI chain-of-spheres (RIJCOSX) approximation.[19,20] Calculation of the electronic absorption and sulfur K-edge X-ray absorption spectra were performed by selecting all available donors and acceptors or by localizing the donor space to the 1s orbitals of sulfur, respectively.[21] A Gaussian broadening of 3200 cm^{-1} (respectively 0.5 eV) full width at half max was applied to the discrete transition moments. Molecular orbital isosurfaces and transition difference densities were visualized using UCSF Chimera.[22]

^{57}Fe Mössbauer Spectroscopy Mössbauer spectra were recorded in transmission mode with a constant-acceleration Wissel Mössbauer spectrometer, with a ^{57}Co source in a Rh matrix and a Janis closed-cycle He cryostat operating at 80 K. Samples were anaerobically prepared by grinding crystalline solid into a powder using a mortar and pestle. The powder was then sealed in a shallow Teflon cup. Isomer shifts are reported in mm/s and referenced to iron metal at room temperature. Quadrupole splittings are also reported in mm/s. Experimental data were simulated and fit using the Mfit program.

X-Ray Crystallographic Structure Determination

A black prism, **12^{ox}** measuring 0.02 x 0.01 x 0.01 mm^3 was mounted on a loop with oil. Data was collected at -173^{o}C on a Bruker APEX II single crystal X-ray diffractometer, Mo-radiation. Crystal-to-detector distance was 40 mm and exposure time was 240 seconds per frame for all sets. The scan width was 1^o. Data collection was 99.2% complete to 25^o in ϑ. A total of 66859 reflections were collected covering the indices, -47<=h<=47, -47<=k<=47, -14<=l<=14. 6482 reflections were symmetry independent and the R_{int} = 0.1149 indicated that the sample was quite small. Indexing and unit cell refinement indicated a rhombohedral lattice. The space group was found to be R $\bar{3}$ (No. 148).

The data was integrated and scaled using SAINT, SADABS within the APEX2 software package by Bruker. Solution by direct methods (SHELXS, SIR97[23,24]) produced a complete heavy atom phasing model consistent with the proposed structure. The structure was completed by difference Fourier synthesis with SHELXL97.[25,26] Scattering factors are from Waasmair and Kirfel.[27] Hydrogen atoms were placed in geometrically idealised positions and constrained to

ride on their parent atoms with C---H distances in the range 0.95-1.00 Angstrom. Isotropic thermal parameters U_{eq} were fixed such that they were $1.2U_{eq}$ of their parent atom Ueq for CH's and $1.5U_{eq}$ of their parent atom U_{eq} in case of methyl groups. All non-hydrogen atoms were refined anisotropically by full-matrix least-squares. Crystal Data is presented in **Table 3.01**

Table 3.01: Crystallographic data for **12^{ox}**

	12^{ox}
Formula	$C_{30}H_{42}F_{24}Fe_2N_{12}P_4S_2$
MW (g/mol)	1326.46
Crystal System	Trigonal
Space Group	R-3
Unit Cell Dimensions	
a (Å)	39.1499(14)
b (Å)	39.1499(14)
c (Å)	11.8458(5)
α (deg)	90
β (deg)	90
γ (deg)	120
Final R indices	0.0764
R indices (all Data)	0.1312

Results and Discussion:

*Redox Properties of **10**, **11** and **12***:

Complexes **10-12** all have multiple redox events within the acetonitrile window. Oxidation and reductions of these complexes can aid in the understanding of the electronic picture of these metal complexes. The Kovacs group has demonstrated that thiolates lower the reduction potential of ferrous complexes and **10-12** behave similarly (**Table 3.02**).[28,29] Compound **10** has two well defined oxidation features; a lower potential that is reversible with an $E_{1/2}$ of -116mV and an irreversible feature at +466 mV (both vs. Fc/Fc^{+}). The first feature is likely to be a Fe^{II}/Fe^{III} redox couple and the reversibility suggests that there is no change

structurally upon the oxidation in the electrochemical experiment; and reversibility is maintained through many different scan rates (**Figure 3.01** Right). Since ^{1}H NMR spectroscopic studies suggest that the dimeric structure is maintained in solution, there may be no immediate chemical change upon the oxidation, and we could have generated a mixed valent Fe^{II}-Fe^{III} complex. The second irreversible feature could be the oxidation of the second ferrous metal center forming a Fe^{III}-Fe^{III} dimeric species. Due to steric factors, this oxidation could force the dimeric structure to cleave, resulting in the observed irreversible redox feature. A similar trend is observed for **11**, as it has a reversible feature at +112 mV and an irreversible +830 mV (both vs. Fc/Fc^{+}) (**Figure 3.02** and **Table 3.02**). The same trend should apply to this system also, in which the first redox feature is the oxidation of only one of the Fe atoms making a mixed valence Fe^{II}-Fe^{III} complex and the second is the irreversible oxidation to an Fe^{III}-Fe^{III} dimeric species, which cleaves.

Table 3.02: Selected Redox Potentials for **10-12** (vs. Fc/Fc^{+}.)

	10	**11**	**12**
1st $E_{1/2}$	-0.116 V	0.112 V	-0.491 V
2nd $E_{1/2}$	-	-	0.113 V
i_{pa}	0.466 V	0.830 V	0.656 V
1st Reduction	-1.74 V	-1.39 V	-1.89 V

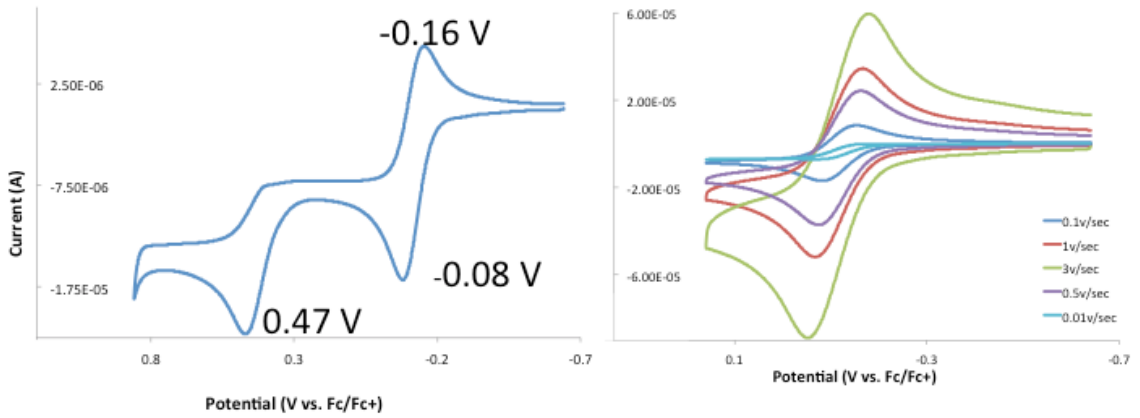

Figure 3.01: 1mM solution cyclic voltamagram of **10** at room temperature (left). Scans taken in MeCN at 0.1V/s with a glassy carbon working electrode and platinum counter electrode. Potentials referenced to Fc^{+}/Fc and a 0.1M solution of $^{n}Bu_4N[PF_6]$ supporting electrolyte. Variable scan rate of feature with $E_{1/2}$ at -.116 V (right).

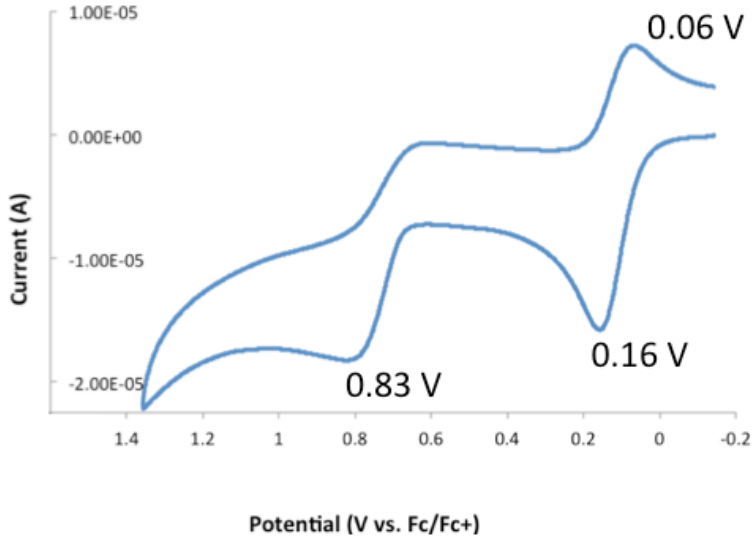

Figure 3.02: 1mM Cyclic voltamagram of **11** at room temperature. Scans taken in MeCN at 0.1V/s with a glassy carbon working electrode and platinum counter electrode. Potentials referenced to Fc^{+}/Fc and a 0.1M solution of $^{n}Bu_4N[PF_6]$ supporting electrolyte.

As discussed in Chapter 2, the structure of **12** in an MeCN solution may not be the same as the solid state structure. This is reflected in the cyclic voltammogram (**Figure 3.03**). Unlike **10** and **11**, which both have two prominent oxidation features, the CV of **12** has three notable features in this same region (**Table 3.02**). The first feature is quasi-reversible with an $E_{1/2}$ of -

491 mV. There is a second smaller feature that is quasi-reversible at +113 mV. The final feature at +656 mV is more reversible than **10** and **11** observed at 656 mV (all vs. Fc/Fc^{+}). Since both ^{1}H NMR spectroscopy and reactivity studies suggest that there may be an equilibrium between a monomer and dimer in solution, each species should have distinct redox potentials. A similar trend for the dimeric species in solution compared to **10** and **11** should be observable, wherein one feature is assigned to an oxidation of the Fe^{II}-Fe^{II}/Fe^{II}-Fe^{III} couple and a second one between the Fe^{II}-Fe^{III}/Fe^{III}-Fe^{III} couple is also expected. As such, the third redox feature observed should consist of the monomeric Fe^{II}/Fe^{III} couple.

The highest redox potential should be the second oxidation of the dimeric species (the Fe^{II}-Fe^{II}/Fe^{II}-Fe^{III} couple) and it may be more reversible than the other two complexes due to the steric factors. If the Fe^{III}-Fe^{III} dimer cleaves due to the decrease in bond lengths of the higher oxidation state then the steric constraint associated with this species could be the cause for the irreversibility. Since an imidazole is less sterically encumbered than a pyridine or quinolone this would provide reason for a more reversible feature than seen in **10** and **11**. The lowest potential may represent the Fe^{II}-Fe^{II}/Fe^{II}-Fe^{III} couple. These Fe metal centers in the dimer are ligated by 2 thiolates which would lower the redox potential compared to the monomer, which is ligated by a single thiolate. Also, the 1 mM concentration is more concentrated compared to UV-Vis solutions and should favor dimer formation, which is observed with the larger peak current.

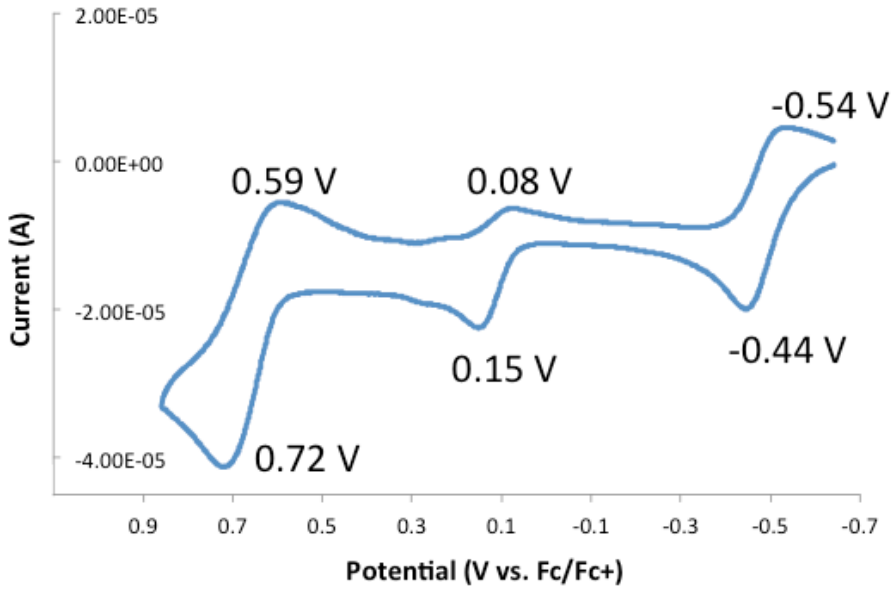

Figure 3.03: Cyclic voltamagram of **12** at room temperature. Scans taken in MeCN at 0.1V/s with a glassy carbon working electrode and platinum counter electrode. Potentials referenced to Fc^{+}/Fc and a 0.1M solution of $^{n}Bu_4N[PF_6]$ supporting electrolyte.

The lowest redox potential of these three complexes correlates with the size of the *N*-heterocycle. As the conjugation of the *N*-heterocyclic ring increases this will stabilize and lower the energy of the empty π^*-orbital making it closer in energy match to the metal d orbitals. Since these empty π^* orbitals have a π-bonding interaction with the Fe d-orbitals, they will interact with the orbitals that consist primarily of the d_{xy}, d_{xz}, and d_{yz} which are filled and consist of the HOMO orbitals being probed by CV. The closer in energy these orbitals are to each other the more energy stabilization will be seen in the bonding orbitals, thus stabilizing the filled metal orbitals. This pattern is observed with the $E_{1/2}$ as **11**, which should have the most stabilized metal orbitals, is the hardest to oxidize while **12** has the weakest π-acceptor is the easiest to oxidize.

Chemical oxidation of these complexes allowed for the spectroscopic observation of the oxidized products. Due to the dimeric structure of **11**, and the reversibility of the first wave, it

should be possible to isolate a mixed-valent species by treatment with a mild oxidant. Electrochemical oxidation was performed with a 0.4 mM solution of **11** in MeCN in a 1 mm path length cell with a tin-doped indium oxide (ITO) slide as a working electrode, Pt wire counter electrode and a Ag wire reference electrode. The $E_{1/2}$ reversible couple was observed at 570 mV (vs. Ag^+/Ag). Holding the potential at 0.7 V (vs. Ag^+/Ag) results in the formation of a new species, $\mathbf{11^{ox}}$, with UV/Vis features at 632 nm and 507 nm (**Figure 3.04**). Isosbestic points at 549 nm, 452 nm, and 407 nm suggest the clean conversion of **11** to $\mathbf{11^{ox}}$. Complete reversibility from **11** to $\mathbf{11^{ox}}$ and back to **11** can be accomplished by varying the potential from 0.4-0.7 V vs. Ag^+/Ag and back to 0.4 V at slow scan rates. The same isosbestic points are observed during both the oxidation and reduction.

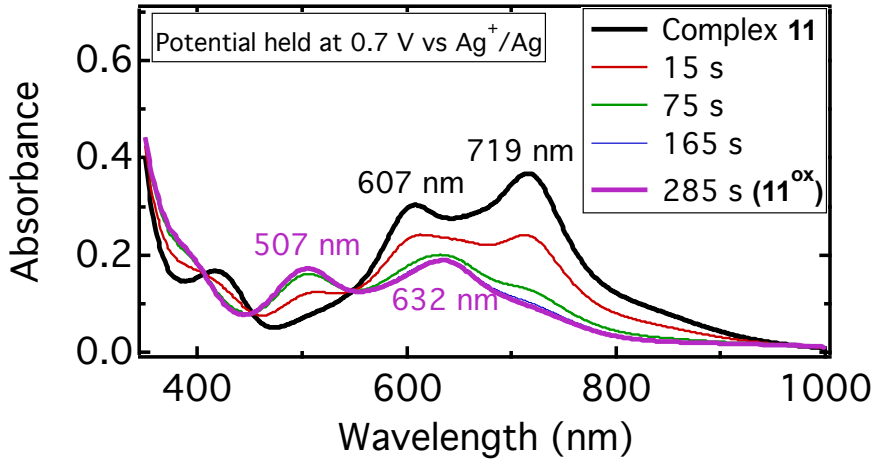

Figure 3.04: Conversion of **11** to $\mathbf{11^{ox}}$ through electrochemical oxidation. Isosbestic conversion suggests a single species is formed.

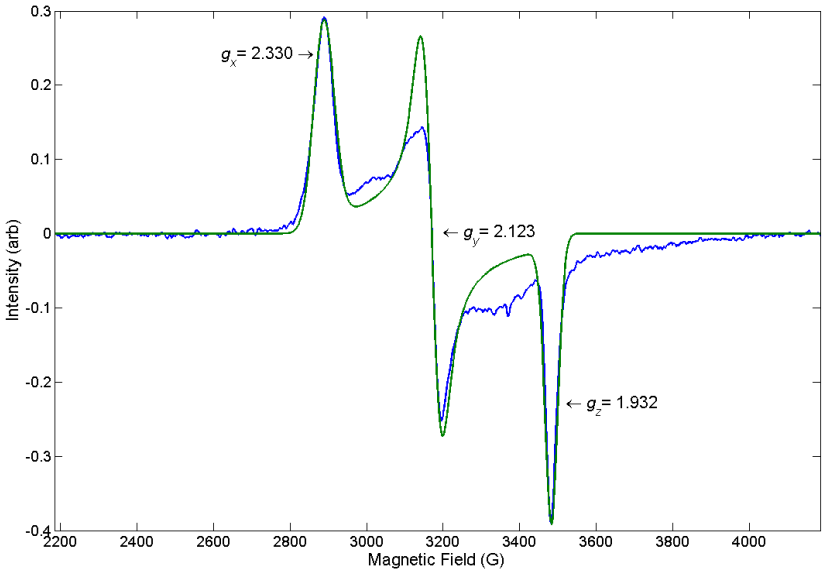

Figure 3.05: EPR spectrum (9.4 GHz) of **11**^{ox} in MeCN:toluene (1:1) glass at 10K with an Easy-Spin simulated spectrum.

Chemical oxidation of **11** with tri-(*p*-tolyl)aminium hexafluorophosphate ([(*p*-$CH_3C_6H_4)_3N][PF_6]$, $E°'$ = 0.4 V vs. Fc/Fc^+ in MeCN) generates the same **11**^{ox} with a paramagnetic ^1H NMR spectrum and an EPR spectrum consistent with an S=1/2 system (**Figure 3.05**). The EPR spectrum (10 K, 9.396 GHz) was simulated with EasySpin to give a rhombic signal with g_1 = 2.330, g_2 = 2.123 and g_3 = 1.932.[30] Interestingly, **11**^{ox} is unstable and converts back to **11** after a period of approximately three hours. Quantitation using the molar absorptivity of the peak at 719 nm indicates that 80% of **11** is regenerated.

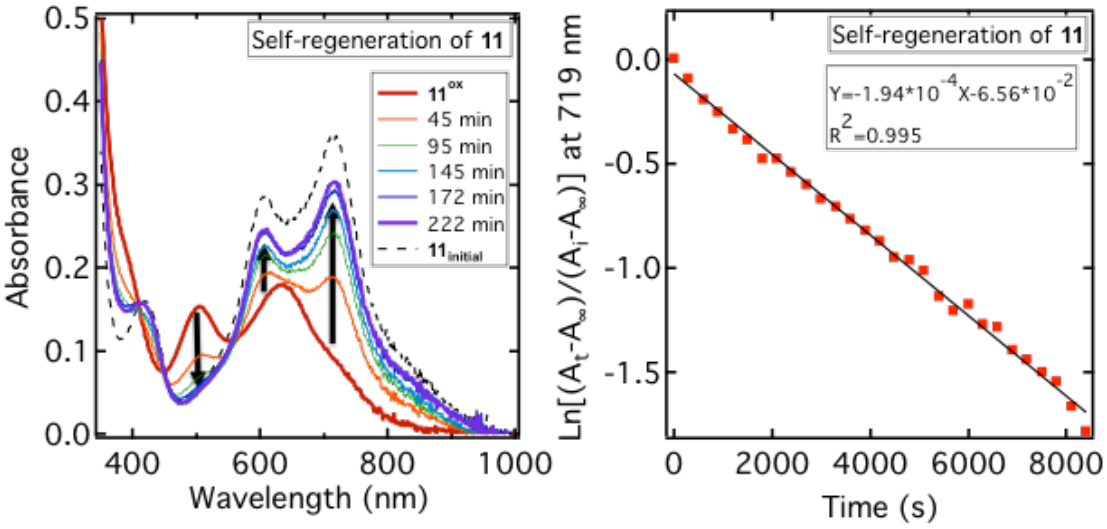

Figure 3.06: Regeneration of **11** after oxidation with tri-(*p*-tolyl)aminium hexafluorophosphate (left). First order kinetics of the reduction of $\mathbf{11^{ox}}$ monitored at 719 nm (right).

The linear relationship between $\ln[(A_t-A_\infty)/(A_i-A_\infty)]$ at 719 nm vs. time implies that the regeneration is first order ($k_{obs}(1) = 2.0\times10^{-4}$ s^{-1}) with respect to **11** (**Figure 3.06**). The regenerated **11** can be oxidized again to generate the same $\mathbf{11^{ox}}$. This $\mathbf{11^{ox}}$ will again reduce back to **11** in comparable yields (80%) with approximately the same rate ($k_{obs}(2) = 1.2\times10^{-4}$ s^{-1}) as the first reduction. This conversion back to **11** is solvent dependent as the k_{obs} is two orders of magnitude slower in DCM ($k_{obs}(DCM) = 6.9\times10^{-4}$ s^{-1}) than MeCN whereas in MeOH there is no observed conversion to $\mathbf{11^{ox}}$. The regrowth of **11** suggests there is a sacrificial reductant in solution. One possibility is that a disproportionation reaction is responsible for the regeneration of **11**. If $\mathbf{11^{ox}}$ is an Fe^{II}-Fe^{III} mixed valent bimetallic species, a disproportionation would generate 50% Fe^{III}-Fe^{III} and 50% Fe^{II}-Fe^{II} (**11**), which is not consistent with the observed yield. However, the mixed valence, Fe^{II}-Fe^{III}, species may be a source for more than 1 e^-. The thiolates can act as a reductant and as such more than $1e^-$ could be obtained from the Fe^{II}-Fe^{III} bimetallic species, affording a higher yield than would be predicted from a simple disproportionation.

While **10** has what seems to be a reversible 1e$^-$ feature in the CV, it takes 2 equivalents of a chemical oxidant ([Fc]PF_6) to fully convert it to a new species. This new species has a feature at 520 nm at half the intensity of the initial feature at 650 nm (**Figure 3.07**). This new feature will shift upon the addition of small anionic substrates and suggests that it is a monomeric Fe^{III} thiolate complex. So far attempts to crystalize this new product have been unsuccessful preventing unambiguous assignment. The observation of a visible charge transfer does suggest that this may be a thiolate ligated ferric complex similar to others that have been previously observed in the Kovacs lab.[31,32]

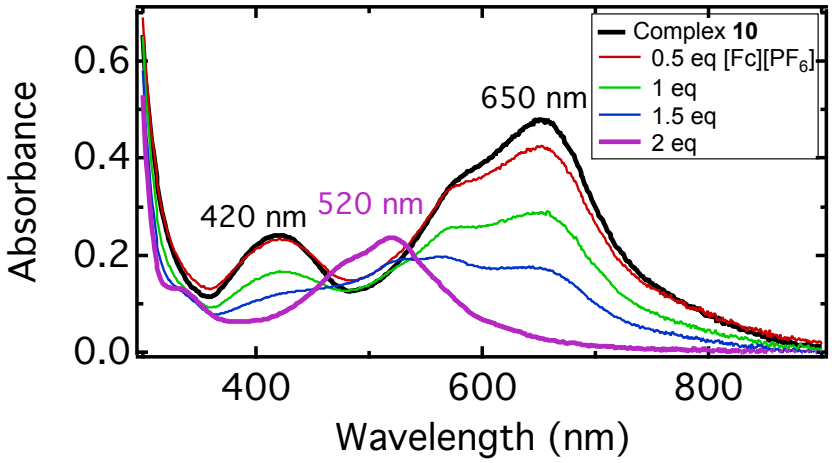

Figure 3.07: Chemical oxidation of **10** with [Fc]PF_6 in MeCN RT.

In a similar manner the oxidation of **12** also requires 1 equivalent of chemical oxidant ([Fc^+]PF_6) per Fe equivalent to fully convert to a new species with less intense visible charge transfer transition that is most likely due to a sulfur to metal charge transfer. Interestingly an X-ray quality single crystal was obtained from this reaction however, it had an unusual geometry (**Figure 3.08**). This solid-state structure maintained a dimeric core with two bis-μ-thiolotes. However, unlike the reduced solid state structure which had overall C_2 symmetry, this Fe^{III} core has C_{2h} symmetry, akin to **11**. The four counterions support the increase by 1 oxidation state of each Fe. The Fe-S bonds decrease slightly from the reduced **12**, however the Fe-N bond lengths

actually elongate slightly (**Table 3.03**). This is most likely due to the fact that both systems contain a low-spin Fe ion. 1 e^- would be removed from orbitals that are t_{2g}-like and do not impact bond lengths as much as the e_g-like orbitals, which are σ^* in character. However, the e^- could be removed from a metal orbital that has a π^* interaction with the thiolates, which would be responsible for the contraction of the Fe-S bond lengths.

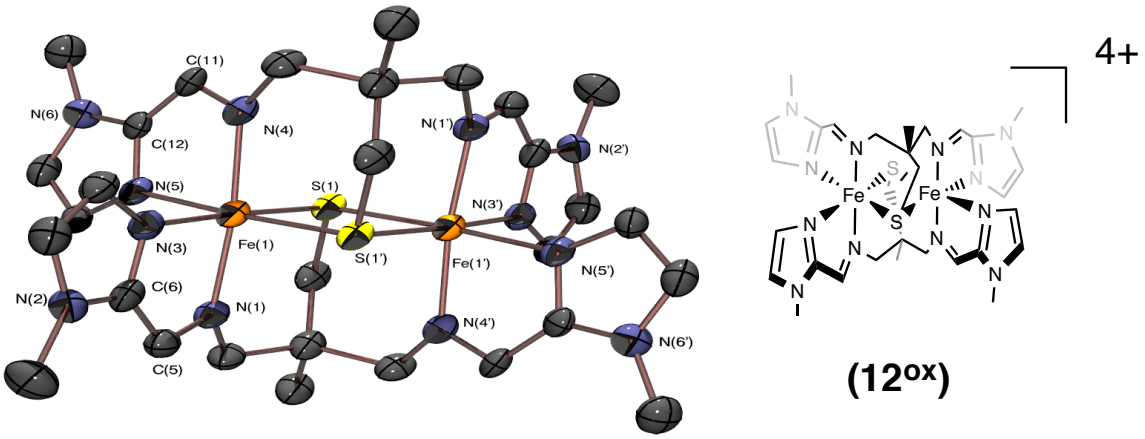

Figure 3.08: X-ray crystal structures of **12**^{ox} with 50% probability ellipsoids. Counterions, cosolvents and hydrogens omitted for clarity (Left). Unlike **12**, which crystalized in C_2 symmetry, this crystalized in a C_{2h} symmetry in the solid state. Corresponding structural representations (Right).

Table 3.03: Selected bond lengths for **11**^{ox}.

Metal bonds	Bond lengths (Å)
S(1)-Fe(1)	2.2426(16)
S(1)-Fe(1')	2.2406(15)
N(1)-Fe(1)	1.983(4)
N(3)-Fe(1)	1.973(5)
N(4)-Fe(1)	2.000(4)
N(5)-Fe(1)	1.979(4)
Intra-Ligand bonds	
N(1)-C(5)	1.300(7)
C(5)-C(6)	1.421(8)
N(4)-C(11)	1.295(6)
C(11)-C(12)	1.406(7)

Interestingly, the intra-ligand bond lengths do not change much. Even in the oxidized complex, the bond lengths are consistent with an elongated imine, which potentially has electron density residing in the ligand orbitals. This could be due to the fact that the complex is still well suited to have significant backbonding into the imine π^* orbital. This complex will still have electron pairs in orbitals that may interact in a backbonding fashion with the imine π^* orbital. In addition, the planar Fe_2S_2 core may cause the thiolates to have significant electron donating ability to the metal and delocalized onto the imine π^* orbital, resulting in bond length contraction.

A simple oxidation of this complex would seem unlikely to change the symmetry of the resulting dimeric product. It seems that the geometry and solid state structure of this complex can be controlled by the concentration of the initial metal template condensation. Doubling the concentration of the reaction to make **12** will produce a different ^{1}H NMR spectrum and instead of a paramagnetic species in solution, there is primarily a diamagnetic product (**Figure 3.09**). This diamagnetic product has a splitting pattern that is consistent with a C_{2h} symmetric structure, as in **11**. For the C_{2h} symmetric solution state structure, two doublets at 4.83 ppm and 4.30 ppm are associated with the 4 protons on the methylene carbons adjacent to the imine nitrogen. In addition, the methylene protons on the carbon adjacent to the sulfur are not split into two doublets, but instead are a singlet at 1.01 ppm.

However, there is a conversion from the diamagnetic C_{2h} symmetric dimer to the paramagnetic **12** over time (**figure 3.09**). This conversion is dependent on concentration and, with the addition of an internal standard, is second order with respect to the starting dimeric

complex. A second order rate constant for reactions of this type is unusual, and further studies are ongoing in an attempt to understand the mechanism of this transformation.

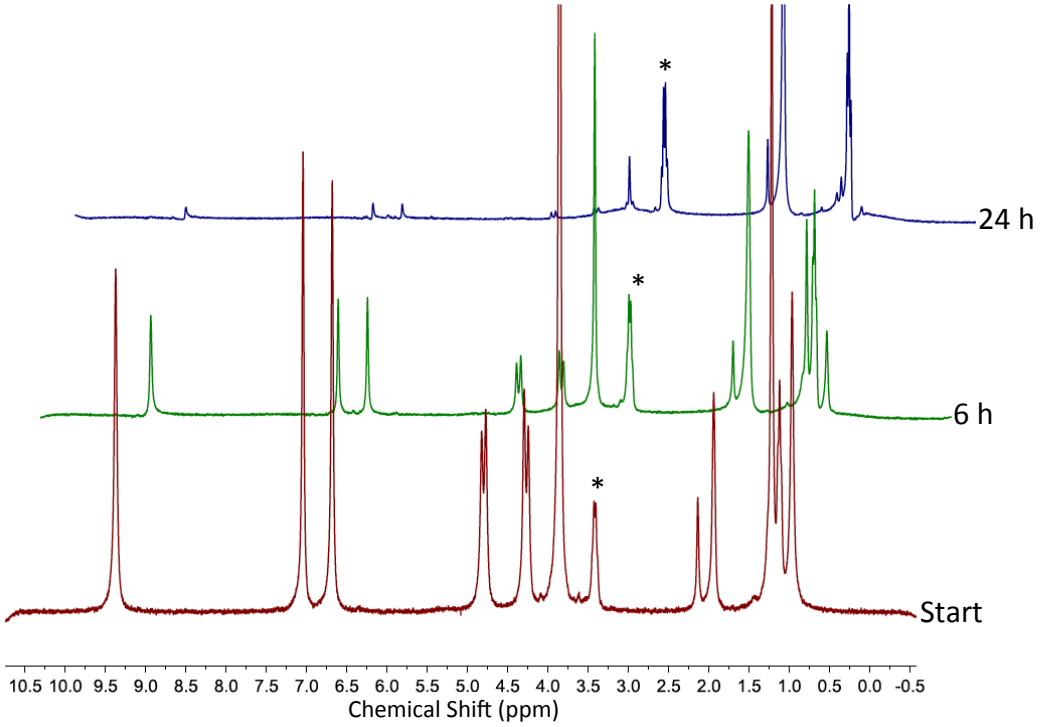

Figure 3.09: Conversion of diamagnetic C_{2h} **12** to the paramagnetic species overtime in anaerobic MeCN-d_3. *Et_2O internal standard.

The change between the two species can also be observed by UV-Vis spectroscopy. The diamagnetic complex has a red-shifted λ_{max} (642 nm) with a slightly larger extinction coefficient (15000 M^{-1} cm^{-1}) (**Figure 3.10**). This could be due to the better orbital overlap between the thiolate, Fe and imine π^* orbital. Comparing the solid state structures of **11** and **12,** it is observed that the bis-thiolate bis-Fe core is slightly puckered in **12** compared to the planar C_{2h} **11.** This will increase the orbital overlap and can be seen in the electronic absorption spectra, as **11** has the highest molar absorptivity of these complexes. Thus, the observed higher molar absorptivity in the diamagnetic **12** would be consistent with this theory. In addition the better π overlap of the thiolate should raise the HOMO metal *d* orbitals resulting in a lower energy charge transfer. The

diamagnetic species reacts slowly with O_2 while after it converts to the paramagnetic species, the same fast reactivity with O_2 is observed. This suggests that the C_{2h} geometry impacts the ability for these complexes to be oxidized by O_2, most likely due to the lack of a vacant coordination site.

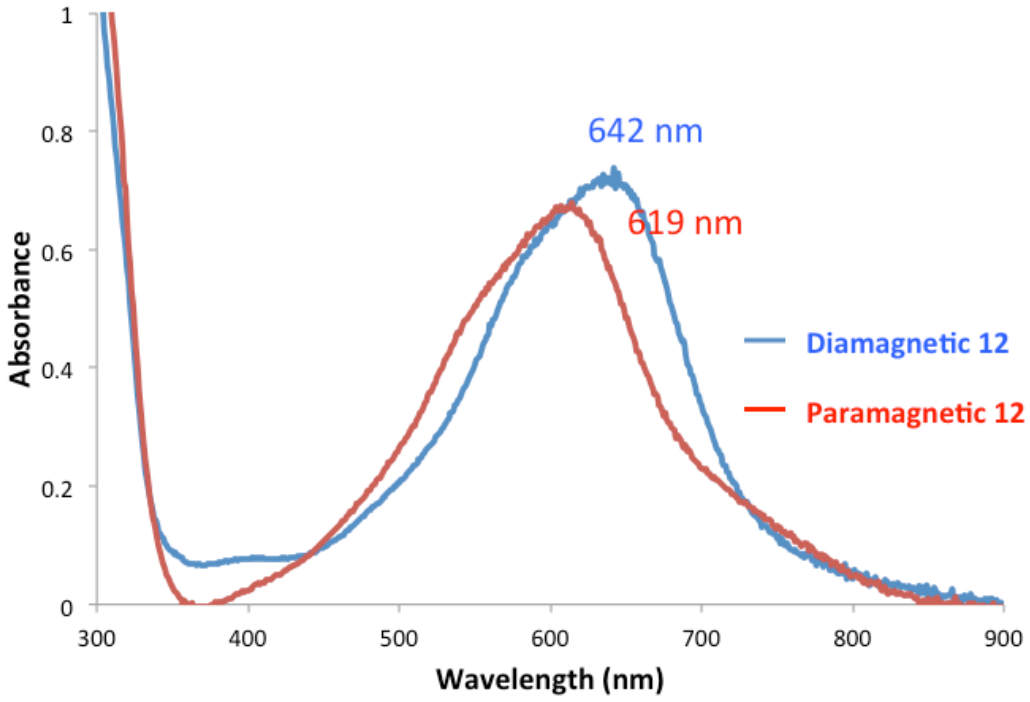

Figure 3.10: Electronic absorption spectrum comparing paramagnetic **12** (red) and diamagnetic **12** (blue). The charge transfer is red shifted for the diamagnetic **12**. Starting Fe dimer concentration is 0.058 mM for paramagnetic **12** and 0.047 mM for diamagnetic **12**.

Negative Region of CV of **10**, **11**, and **12** *and Ligand Based Reductions*:

One well-documented aspect of α-(imino)pyridine ligands is the ability to accept an electron. These reductions are observed at negative redox potentials in the cyclic voltammograms. Weighardt has observed reduction potentials around -1 V vs. Fc/Fc^+ for a variety of first row metals containing α-(imino)pyridine.[7,33] Complexes **10-12** all contain similar features (**Figure 3.11**). The reduction potentials seem to have the opposite trend of the oxidation potentials with the E^0 **11** > E^0 **10** > E^0 **12** (**Table 3.02**).

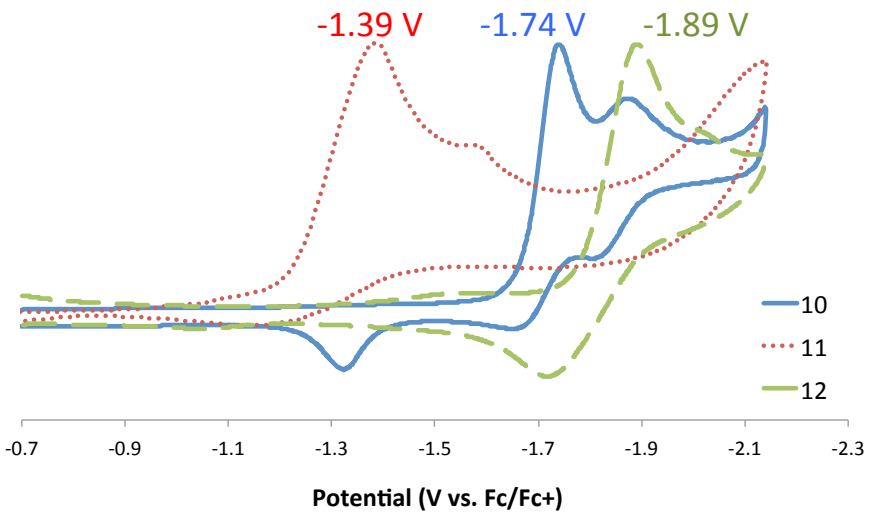

Figure 3.11: 1mM cyclic voltamagrams of **10-12** from -0.7 V to -2.1 V indicating the proposed ligand reduction. The current is normalized. Scans taken in MeCN at 0.1V/s with a glassy carbon working electrode and platinum counter electrode. Potentials referenced to Fc^{+}/Fc and a 0.1M solution of $^{n}Bu_4N[PF_6]$ supporting electrolyte.

The reduction will depend on the imine and the conjugated *N*-heterocycle. As the conjugation increases, it should lower the energy of the of this ligand acceptor orbital. As such, **11** has a redox potential observed at -1.39 V vs. Fc/Fc^{+} due to the much larger 10-atom quinoline. The 6-atom pyridine in **10** is harder to reduce at -1.74V vs. Fc/Fc^{+}, while the smallest 5-atom imidizole, **12**, has the most negative reduction potential at -1.89V vs. Fc/Fc^{+}. It should be noted that these reduction potentials are much more negative and harder to reduce than the α-(imino)pyridine complexes that Weighardt *et al.* observed.[6] This may be due to the overall charge of the molecule. While **10-12** are mono-cationic, Weighardt's un-reduced complexes are dicationic suggesting it should be easier to add electrons to these molecules. Also, when looking at the specific α-(imino)pyridine, it seems that the thiolate and Fe may already be donating electron density to the π^{*} redox orbital, suggesting it would be harder to add further reduce this moiety.

Sulfur X-ray Absorption Spectroscopy of **10**, **11**, and **12***:*

Sulfur K-edge X-ray absorption spectroscopy (XAS) has been well-established as a sensitive measure of sulfur-metal covalency.[34,35] Excitation of a sulfur 1*s* electron to the LUMOs probes both the energy of the acceptor orbital, typically a metal 3*d* in the case of first-row transition metals, as well as the extent of sulfur 3*p* mixing into that acceptor wavefunction and can be observed in the pre-edge region.[36,37] The sulfur K-edge XAS spectra of solid samples of **10-12** are shown in (**Figure 3.12**), and exhibit two intense transitions in the 2471-2475 eV region (**Figure 3.13** top, **Table 3.04**). Intriguingly, the first peak, which is assigned as a pre-edge feature, differs in both energy and intensity between compounds, and similar to the electrochemical reduction potentials, is found to correlate with the size of the ligand *N*-heterocycle. Changes in the reduction potentials roughly correspond to changes in the energy of the LUMO. Thus, the similar trend observed in these data suggests that the first S XAS peak may arise from sulfur 1s to LUMO transitions (**Figure 3.14**).

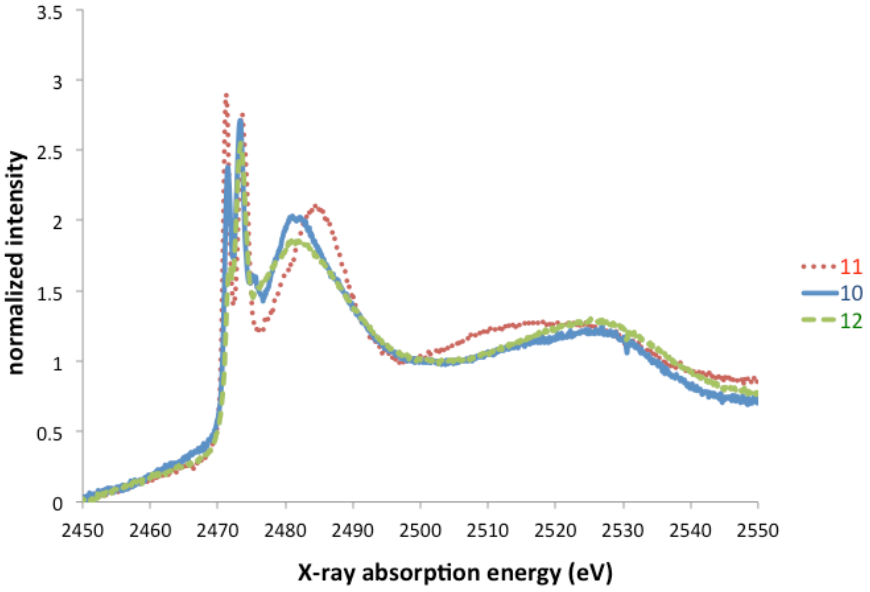

Figure 3.12: Sulfur K-edge X-ray absorption spectra for **10-12**. The spectra are normalized to the EXAFS region.

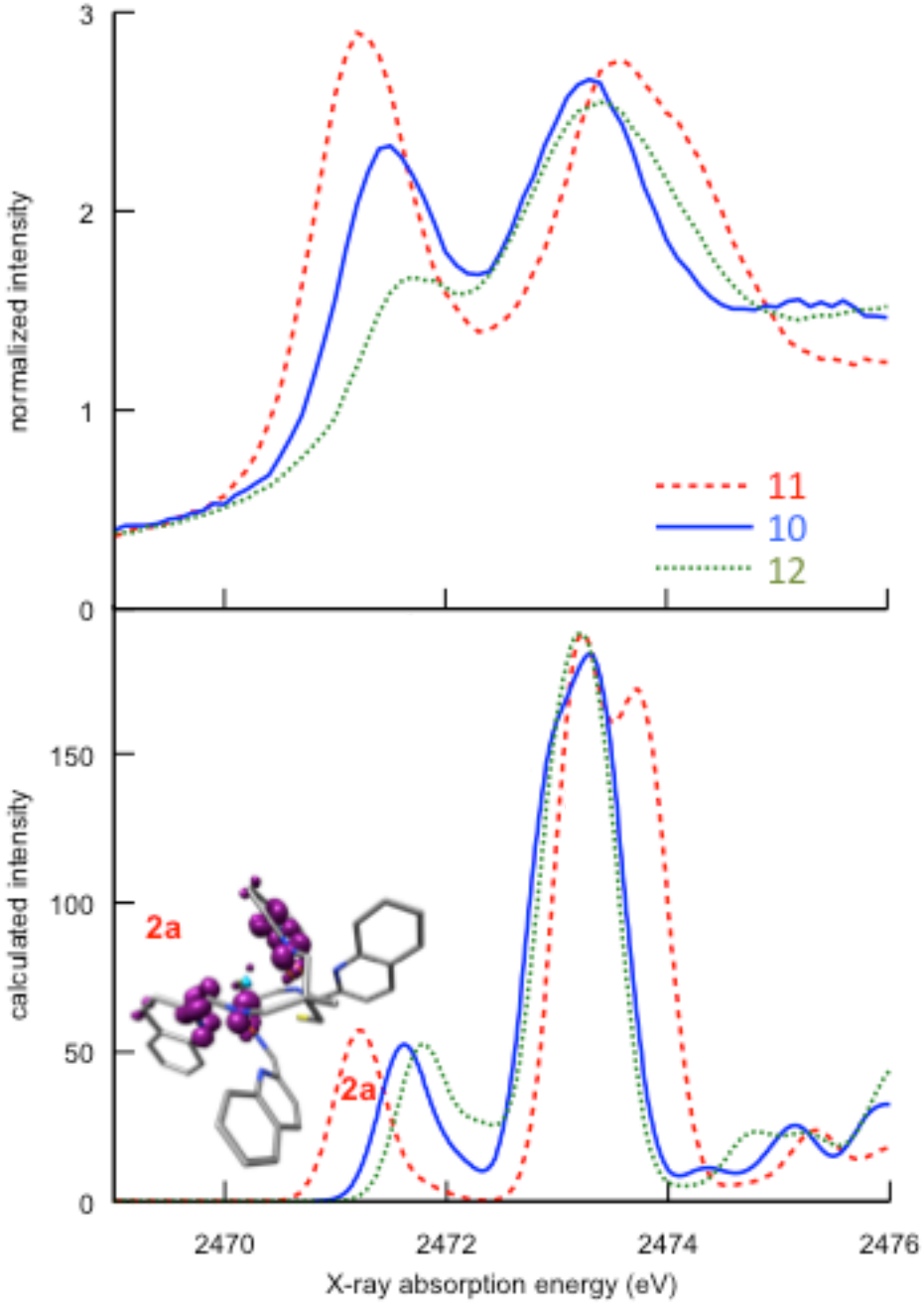

Figure 3.13: Pre-edge transitions of sulfur K-edge X-ray absorption spectra for **10-12** (top). The lower energy transition tracks well with ring size. Calculated spectra (bottom) compares favorably with the experimental data and have two transitions (2a and 2b). Visualization of the donor and acceptor states for the first transitions of **11** are shown in inset of bottom spectrum.

Table 3.04: Energy of the two transitions obtained from Sulfur K-edge XAS for **10-12**.

	1st Transition (eV)	2nd Transition (eV)
10	2471.5	2473.3
11	2471.2	2473.6
12	2471.7	2473.4

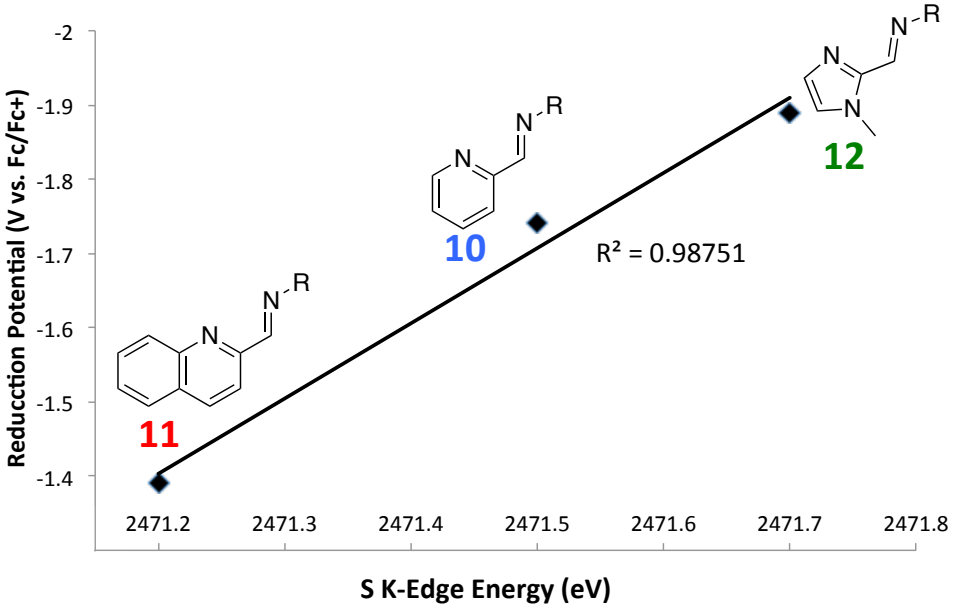

Figure 3.14: Correlation plot between the S K-edge energy and reduction potential showing good correlation between these two techniques probing the LUMO orbital.

Changes in the higher energy peak do not display the same trend; the peak of quinoline-ligated **11** is highest in energy. In a low-spin ferrous complex, the t_{2g} orbitals would be completely filled, however transitions into the unoccupied Fe e_g^* are anticipated. The blue-shifted peak of **11** indicates destabilization of the e_g^* relative to **10** and **12**, which is consistent with **11** having the shortest iron-sulfur bond length. The donor states of this transition were found computationally to contain e_g^* character in addition to both C-S σ^* and some small amount of sulfur 4p character. This would then be a mixture of pre-edge and edge type transitions and will be discussed in the next section.

Density Functional Theory Calculations:

Density functional theory (DFT) calculations were performed to investigate the structural, spectroscopic, and electrochemical properties of these complexes. Geometry optimizations were initiated from crystallographic coordinates, using both closed-shell and broken-symmetry singlet configurations. In all cases the lowest energy closed-shell solution, with neutral ligands and S=0 Fe(II) ion. In particular, the distinct crystallographic metrics associated with both the Fe-ligand bond lengths and the intra-ligand bond lengths are reasonably close to the crystallographic metrics (**Table 3.05**), suggesting that the electronic effects responsible for these structural features are successfully reproduced by the calculations. A qualitative MO diagram for **10** and **12** is shown in **Figure 3.15** with **11** having a similar diagram. Consistent with the diamagnetic ground state, all t_{2g}-type orbitals are doubly occupied. The significant mixing between the Fe and S atomic orbitals is observed in the d_{xy} and d_{xz} orbitals as well as the S p-orbital, and is typical for thiolate-ligated Fe sites.[11] Again, consistent with the conjugated portion of the ligand scaffold being π-acidic in nature, the LUMO was found to be imine π^*, with Fe e_g orbitals higher in energy. Analogous electronic structures were found for **11**.

Table 3.05: Selected DFT bond metrics for **DFT 10-12**. Note that the **DFT 10** and **DFT 11** had symmetric structures while **DFT 12** had asymmetry around each Fe atom.

	DFT 10 (Å)	DFT 11 (Å)	DFT 12 Fe(1) (Å)	DFT 12 Fe(2) (Å)
Fe-S(1)	2.270	2.243	2.323	2.320
Fe-S(2)	2.283	2.243	2.322	2.328
Fe-$N_{heterocycle}$(1)	1.957	1.937	1.982	1.980
Fe-$N_{heterocycle}$(2)	1.962	1.936	1.990	1.982
Fe-N_{imine}(1)	1.900	1.925	1.949	1.956
Fe-N_{imine}(1)	1.890	1.927	1.954	1.960
N_{imine}(1)-C	1.310	1.313	1.293	1.293
Intra-Ligand Bond Lengths				
C-C	1.432	1.439	1.426	1.428
N_{imine}(2)-C	1.306	1.313	1.290	1.290
C-C	1.434	1.439	1.429	1.430

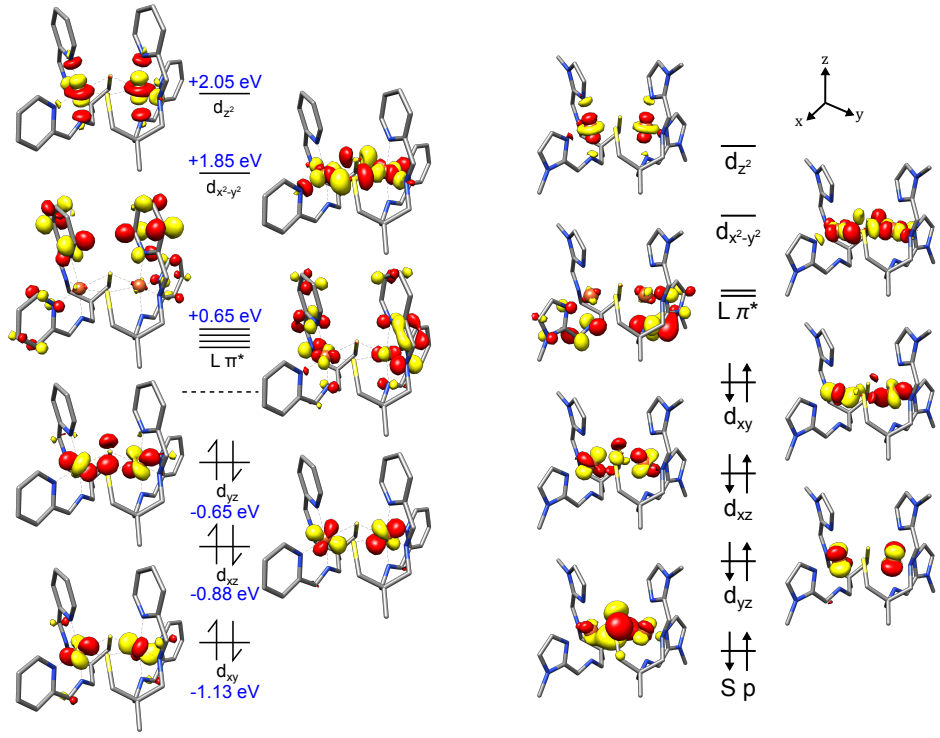

Figure 3.15: DFT calculated molecular orbital for **10** (Left) and **12** (right) with the contributions from each atomic orbital present on the sides. **11** has a very similar electronic structure and all three optimize to a diamagnetic Fe metal center. The LUMO orbitals seem to be composed primarily of ligand based redox orbitals.

These results are consistent with the correlations between LUMO energy and the ring size of the *N*-heterocycle observed in the electrochemical reduction potentials and the first sulfur XAS transitions. While this energetic ordering of the molecular orbitals is not surprising in light of the abundant literature precedent in this field,[7,8] the apparent involvement of the thiolate in these redox-active orbitals is unusual. In particular, strong optical and X-ray absorption transitions imply substantial orbital communication between the sulfur 3p and ligand π^* orbitals. The nature of the underlying electronic transitions in both absorption spectroscopies was investigated using TD-DFT calculations.

The putative charge-transfer nature of the transitions in the electronic absorption spectra prompted the use of the range-separated hybrid density functional CAM-B3LYP for these calculations. As shown in **Figure 3.16**, the TD-DFT-calculated electronic absorption spectra of **10** and **11** both have intense transitions in the visible region. The relative energies and intensities are in good agreement, though the absolute transition energies are overestimated by approximately 200 nm when compared to the experimental electronic absorption spectra; a well-known shortcoming of TD-DFT.[38] However, the nature of these transitions can be examined with reasonable fidelity via the transition difference densities. For both complexes, the intense visible CT transitions are found to have donors and acceptors that are mixed Fe/S and imine π^* in character, respectively. The iron 3d-orbitals thus appear to mediate charge transfer from the thiolate 3p to the formally orthogonal ligand π^* LUMO.

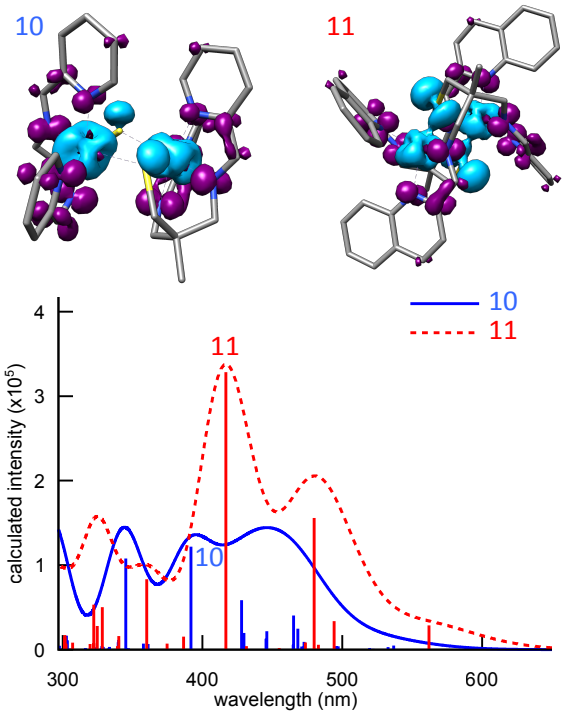

Figure 3.16: CAM-B3LYP TD-DFT computed electronic absorption spectra for **10** and **11** (bottom) along with the difference states diagrams of these transitions(top). Donor states in teal blue and acceptor states in purple.

As discussed previously, sulfur K-edge XAS provides a more focused probe of the thiolate bonding in these complexes. **Figure 3.13** bottom shows the TD-DFT-calculated S K-edge XAS spectra of **10-12**. Comparison with the experimental spectra above reveals that the energetic trends observed in both peaks are successfully reproduced. Examination of the transition difference densities reveals that the lower-energy feature indeed corresponds to sulfur 1*s* → ligand π^* LUMO transitions, as proposed above. The higher-energy feature in the sulfur XAS spectra of **10-12** is found to be due to transitions to the unoccupied Fe e_g-type orbitals but does have mixing of the C-S σ^* and even sulfur 4*p* character as shown in the full assignment stick spectra for all three complexes (**Figure 3.17**). This would make the peak a mixture of both edge and pre-edge features. While the TD-DFT calculations do not reproduce the intensity trend of the first pre-edge peak, the dramatic charge-transfer nature of these transitions make them subject to another known methodological shortcoming of TD-DFT. The experimental intensities provide clear evidence of decreased sulfur 3*p* / ligand π^* LUMO mixing within the series, with **11** > **10** > **12**. Importantly, the intensities of the higher-energy transitions are relatively unchanged compared to the variations in the low-energy pre-edge peak. This implies that the covalency of the Fe-S bonds is mostly constant for all three complexes, and that the changes in sulfur 3*p* / ligand π^* mixing are not due to decreased iron-thiolate interactions. Instead, thiolate π donation into the LUMO ligand π^* could be mediated by backbonding of the Fe t_{2g}-type orbitals, which presumably changes as a function of ring size and LUMO energy.

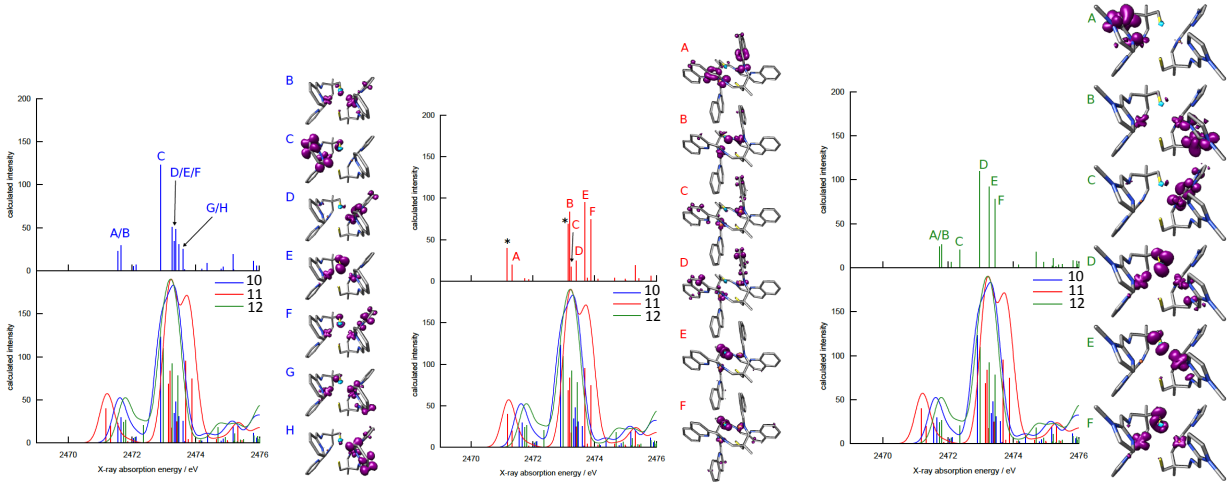

Figure 3.17: Full assignment of the second transition in sulfur K-edge XAS for **10-12**. Stick spectra shows contribution of all acceptor orbitals and indicates the complex mixture of transitions for the higher energy peak including e_g^*, C-S σ* and even sulfur 4 *p* character.

Role of the Thiolate and an Observation of a cis "Push Effect":

The direct involvement of thiolate-based electron density in promoting the activation of the ligand π* orbitals in **10-12** is shown by the S K-edge XAS data, wherein electronic transitions from the localized thiolate 1s orbital into the LUMO π* can be observed. This transition intensity is engendered by the presence of thiolate 3p character in the unoccupied π* orbitals; thus ligand π* character is expected in the occupied thiolate 3*p* orbitals. The absence of direct thiolate-π* bonds predicates this interaction on orbital mixing mediated by the metal 3*d* orbitals of appropriate symmetry. This is akin to the proposed "push effect" in cytochrome P450, where electronic donation from the thiolate orbitals into the iron 3*d* populates the O-O *σ** orbital of the ferric hydroperoxo compound 0.[39,40] Notably, while this thiolate π push effect in cytochrome P450 activates the *trans* ligand, the 4-fold symmetry of the relevant t_{2g} orbital should enable similar activation of *cis* ligands, as observed in the present system.

Assignment of the first feature in the S K-edge XAS spectra of **10-12** is supported by the correlation of the transition energy and intensity with ring size. These data suggest that energies of the ligand-based redox-active orbitals can be effectively tuned via modulation of the size of the conjugated π system. Given this interpretation, the relative energies of these same LUMO orbitals can also be probed by electrochemical reduction. In fact, quantitative comparison of the first reduction potentials of **10-12** with the corresponding first transition energies, from S K-edge XAS, and the LUMO (α-imino)*N*-heterocycle orbital energies, obtained from the DFT calculations, are in excellent agreement (**Figure 3.18**). An important aspect of this class of base metal catalysts is the ability to mitigate electronic demands at the metal via facile redox communication with ligand-based orbitals. Therefore, tuning the energies of these ligand-based orbitals through altering the size of the ligand π system may present an effective design strategy.

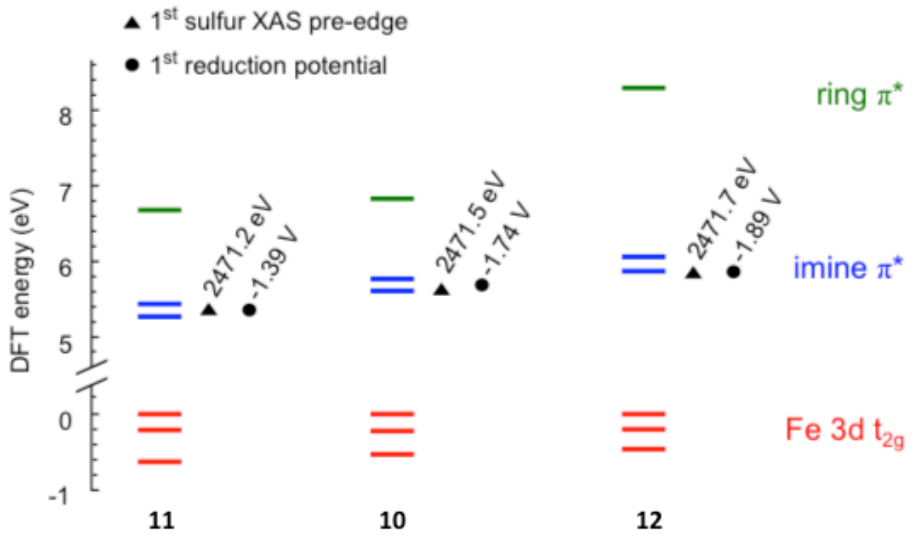

Figure 3.18: DFT calculated energy levels overlaid with normalized S XAS and the 1st reduction potential of **10-12**.

Additionally, Betley and coworkers have shown that communication between ligand and metal orbitals is predicated on effective orbital overlap.[41,42] Thus, modulating the extent of

metal-ligand redox orbital coupling may provide a means to fine tune the cooperativity of the molecular redox orbitals. The intensities of electronic transitions provide an effective means of quantifying orbital coupling. As observed in the S K-edge XAS spectra of **10-12**, diminished sulfur 1s → LUMO π* transition intensity is found to correlate with decreasing ring size. It should be noted that the intensities of the UV-visible charge-transfer transitions of **10** and **11** display the same trend, however the ambiguous solution-state speciation of **12** precludes similar comparison. While it may not be surprising that an improved orbital energetic match leads to better overlap, the importance of this coupling for effective redox cooperativity should not be overlooked.

*^{57}Fe Mössbauer Spectroscopy of **10**, **11** and **12**:*

The local electronic structure of the Fe atoms was also investigated by ^{57}Fe Mössbauer spectroscopy.[43,44] The zero-field ^{57}Fe Mössbauer spectra of **10** is shown in **Figure 3.19** while, **11** and **12** are shown in **Figure 3.20** and the calculated and experimental parameters are reported in **Table 3.06**. The isomer shift δ (the midpoint of the quadrupole doublet) is primarily sensitive to perturbations in Fe 4*s* electron density ρ_0 at the Fe nucleus, which can be modulated by the 3*d* orbital population due to shielding. While the $3d^6$ electron count of Fe(II) ions often results in larger isomer shifts than those observed for **10-12**, values in the range δ = 0.3 – 0.45 mm/s are typical for low-spin Fe(II) hemes.[45] The π-acidic nature of the heme prosthetic group promotes π backbonding, which lowers the effective 3d orbital population. As discussed above, the α-(imino)-*N*-heterocycle moieties in **10-12** also act as π backbonding acceptors. Importantly, the extent of π backbonding can be expected to manifest in the value of δ, with decreased backbonding leading to more electron-rich 3d orbitals and a high isomer shift. Thus, π

backbonding appears to be smallest in **12** (δ = 0.41 mm/s) and comparable in **10** and **11** (both δ = 0.36 mm/s). While the former conclusion is in good agreement with the previous spectroscopic data, **11** could be anticipated to have more π backbonding than **10**, based on the sulfur K-edge XAS spectra and TD-DFT calculations. However, just as π-accepting ligands can depopulate the 3*d* orbitals, π-donating ligands, like thiolates, can increase the effective 3*d* orbital population. Comparison of the metrical parameters of **10** and **11** indeed reveals that the Fe-S bonds in **11** are shorter; indicative of increased π donation. Thus, the thiolate ligands in **11** compensate for the increased π-backbonding through more significant π donation, leading to the identical isomer shifts of **11** and **12**.

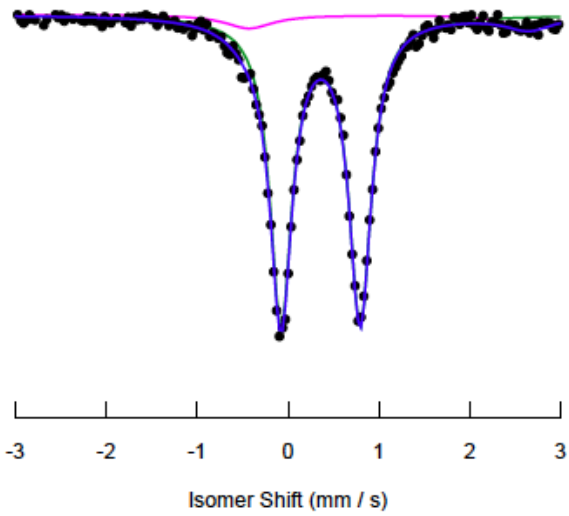

Figure 3.19: Mössbauer spectrum of **10.** Mössbauer spectra were taken in the solid state.

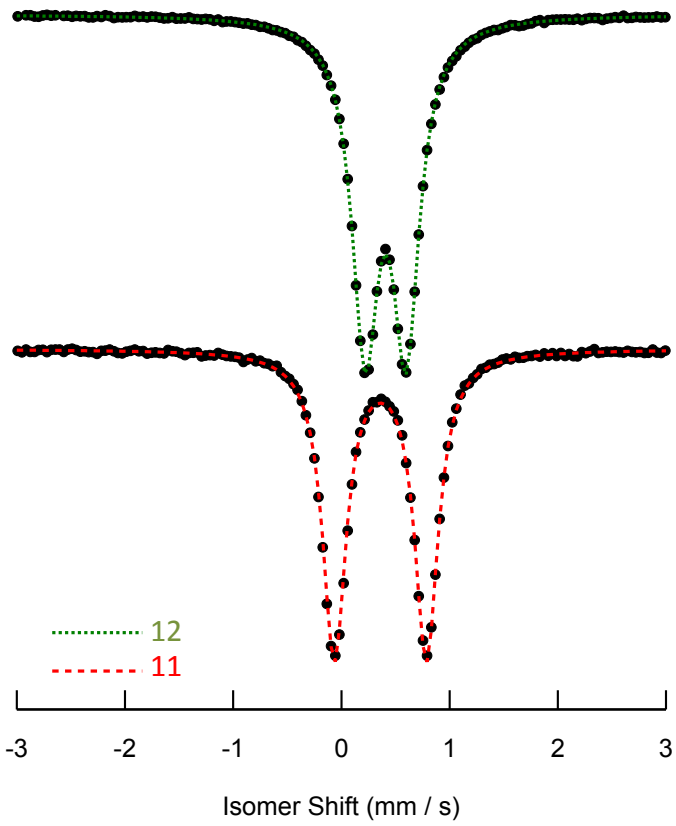

Figure 3.20: Mössbauer spectra of **11** (bottom) and **12** (top). Isomer shift is consistent with a π-acidic ligand framework low-spin Fe(II). Mössbauer spectra were taken in the solid state

Table 3.06: Mössbauer parameters for **10-12** and the computed parameters.

	Isomer shift (δ) (mm/s)	Quadrupole Splitting (ΔE_q) (mm/s)	DFT Isomer shift (δ) (mm/s)	DFT Quadrupole Splitting (ΔE_q) (mm/s)
10	0.36	0.87	0.22	1.07
11	0.36	0.85	0.22	-1.09
12	0.41	0.38	0.39	0.82

While δ, is sensitive to the electron density at the ^{57}Fe nucleus, the quadrupole splitting ΔE_Q provides a measure of the asymmetry of the electric field gradient (EFG) at the nucleus. In the limit of crystal field theory, an S=0 d^6 Fe ion has a spherically symmetric EFG that should

result in the coalescence of the two peaks of the quadrupole doublet. However, the π-donating thiolate and π-accepting α-(imino)-*N*-heterocycle should perturb the effective d-orbital populations and the symmetry of the EFG. As with the isomer shift, the quadrupole splitting parameter of **12** (ΔE_Q = 0.38 mm/s) is smaller than that of **10** (ΔE_Q = 0.87) and **11** (ΔE_Q = 0.85). This is again consistent with decreased π-backbonding in **12**. Interestingly, the quadrupole splitting of **11** is smaller than that of **10**. While the 0.02 mm/s difference is perhaps not so significant, it is contrary to the expected change resulting from increased π-backbonding in **11**. It should be noted, that in fact, the zero-field ^{57}Fe Mössbauer experiment measures the absolute value of ΔE_Q, despite the quadrupole splitting being a signed quantity. The quadrupole splitting arises from the interaction of the I=3/2 nuclear excited state quadrupole moment with the EFG tensor. The main component of the EFG tensor, V_{zz}, is influenced by both the bonding orbitals of the ligands and the effective d-orbital population. The competing contributions from these two sources, modulated by covalency and π backbonding, can determine the sign of V_{zz} as detailed in a recent study of Fe-N_2 complexes.[46]

The DFT-calculated Mössbauer parameters are given in **Table 3.06**, and show excellent agreement with the experimentally observed trends. Interestingly, the calculated ΔE_Q of complexes **10** and **12** are positive, while that of **11** is negative. Importantly, the magnitudes of ΔE_Q for **10** and **11** are comparable, consistent with experiment.[16] The calculations thus suggest that in complexes **10** and **12**, the dominant contribution to EFG asymmetry is from the covalent ligand orbitals (the thiolates), while in **11** strong perturbations to the local d shell from π backbonding invert the sign of ΔE_Q. Indeed, the unique geometry of **11** (*vide supra*) provides excellent rationale for this conclusion. The seemingly activated imine bonds of all three complexes suggest that the imine π* serves as a π backbonding acceptor. The imine ligands are

positioned *cis* to each other in the C_2 geometries of **10** and **12**, and thus π backbonding occurs from two distinct t_{2g}-type 3*d* orbitals (along two axes). In contrast, they are in fact *trans* in the C_{2h} geometry of **11**, and so only a single 3*d* orbital has the correct symmetry to π backbond. This "double" depopulation of one of the t_{2g}-type 3*d* orbitals along a single axis engenders significant asymmetry to the local 3*d* shell; so much so that it becomes the stronger contributor to V_{zz} and inverts the sign of ΔE_Q. In summary, the ^{57}Fe Mössbauer data and accompanying DFT calculations suggest that the extent of π backbonding correlates with the size of the *N*-heterocycle, as proposed above, and evidence a compensatory contraction of the Fe-S bonds in **11** due to stronger π backbonding. Furthermore, the unique geometry of **11** inverts the sign of the quadrupole splitting, and leads to an observed $|\Delta E_Q|$ that is coincidentally similar in magnitude to **10**.

Conclusions:

The combined spectroscopic, electrochemical and computational experiments provide insight into the complicated electronic pictures of these complexes. Each of these complexes redox orbitals are convoluted by the inclusion of the redox-active α-(imino)-*N*-heterocycle and sulfur as well as the metal *d*-orbitals. The solid-state structure displays a lengthening of the imine and C-C bond lengths which suggests that electron density is populating that ligand orbital. The reduction potentials at -1.38 to -1.89 V for **10-12** suggest that the LUMO orbital is indeed ligand based, as observed with other literature complexes. The ability of the thiolate to push electron density was one potential reason for the bond lengthening and the observation of a second peak in the sulfur K-edge XAS suggests that there is some degree of covalency between

the two ligand based redox orbitals. The observed pattern of increase in the LUMO orbitals energy tracks well with the ligand reduction potentials, the S K-edge XAS and the DFT energies.

The potential ability of the thiolate to modulate the electron density around the metal and help push electron density into ligand redox orbitals may prove beneficial for the design of future catalysts incorporating redox-active ligand frameworks. These organic redox orbitals are designed to limit the amount of electronic demands located at the 1st row metal centers aiding them in performing sequential 2e$^-$ redox reactions.[4] The thiolate may increase the ability of these complexes to promote the movement of electron density from the metal center. Additionally it is shown that the size of the *N*-heterocycle clearly effects the LUMO of these redox orbitals. As such, larger ring sizes will lower the energy of these LUMO's making them a better match with the orbitals of the metal center. Matching the ligand orbitals with the metal orbitals can help facilitate the transfer of electron density between the two redox centers.

Notes to Chapter 3

1. Leipzig, B. K.; Rees, J. A.; Nyrov, A.; Theisen, R.; Flowers, S. E.; Kaminsky, W.; DeBeer, S.; Kovacs, J. A. *Prep.*

2. Chirik, P. J.; Wieghardt, K. *Science* **2010**, *327* (5967), 794–795.

3. Green, M. T. *J. Am. Chem. Soc.* **1999**, *121*, 7939.

4. Shaik, S.; Cohen, S.; Wang, Y.; Chen, H.; Kumar, D.; Thiel, W. *Chem. Rev.* **2010**, *110*, 949–1017.

5. Denisov, I. G.; Makris, T. M.; Sligar, S. G.; Schlichting, I. *Chem. Rev.* **2005**, *105*, 2253-2278.

6. Labinger, J. A. *Organometallics* **2015**, *34*, 4784–4795.

7. Bart, S. C.; Chłopek, K.; Bill, E.; Bouwkamp, M. W.; Lobkovsky, E.; Neese, F.; Wieghardt, K.; Chirik, P. J. *J. Am. Chem. Soc.* **2006**, *128*, 13901–13912.

8. Lu, C. C.; Bill, E.; Weyhermüller, T.; Bothe, E.; Wieghardt, K. *Inorg. Chem.* **2007**, No. 46, 7880–7889.

9. Wu, J. Y.; Stanzl, B. N.; Ritter, T. *J. Am. Chem. Soc.* **2010**, *132*, 13214–13216.

10. Neese, F. *Wiley Interdiscip. Rev. Comput. Mol. Sci.* **2012**, *2*, 73–78.

11. Grimme, S.; Ehrlich, S.; Goerigk, L. *J. Comput. Chem.* **2011**, *32*, 1456–1465.

12. Grimme, S.; Antony, J.; Ehrlich, S.; Krieg, H. *J. Chem. Phys.* **2010**, *132*, 154104-154117.

13. van Wüllen, C. *J. Chem. Phys.* **1998**, *109*, 392-399.

14. Klamt, A.; Schüürmann, G. *J. Chem. Soc., Perkin Trans. 2* **1993**, *5*, 799–805.

15. Becke, A. D. *Phys. Rev. A* **1988**, *38*, 3098–3100.

16. Perdew, J. P. *Phys. Rev. B* **1986**, *33*, 8822–8824.

17. Römelt, M.; Ye, S.; Neese, F. *Inorg. Chem.* **2009**, *48*, 784–785.

18. Neese, F.; Wennmohs, F.; Hansen, A.; Becker, U. *Chem. Phys.* **2009**, *356*, 98–109.

19. Dunlap, B. I.; Connolly, J. W. D.; Sabin, J. R. *J. Chem. Phys.* **1979**, *71*, 3396–3402.

20. Feyereisen, M.; Fitzgerald, G.; Komornicki, A. *Chem. Phys. Lett.* **1993**, *208*, 359–363.

21. Neese, F.; Olbrich, G. *Chem. Phys. Lett.* **2002**, *362*, 170–178.

22. Pettersen, E. F.; Goddard, T. D.; Huang, C. C.; Couch, G. S.; Greenblatt, D. M.; Meng, E. C.; Ferrin, T. E. *J. Comput. Chem.* **2004**, *25*, 1605–1612.

23. Altomare, A.; Cascarano, G. L.; Giacovazzo, C.; Guagliardi, A. *J. Appl. Crystallogr.* **1993**, *26*, 343–350.

24. Altomare, A. Burla, C. Camalli, M., Cascarano, G. L., Giacovazzo, C. Guagliardi, A., Moliterni, A. G. G., Polidori, G., Spagna, R. *J. Appl. Crystallogr.* **1999**, *32*, 115–119.

25. Sheldrick, G. M. SHELXL-97: Program for the Refinement of Crystal Structures, University of Göttingen, Germany, 1997.

26. Mackay, S.; Edwards, C.; Henderson, A.; Gilmore, C.; Stewart, N.; Shankland, K.; Donald, A. University of Glasgow, Scotland 1997.

27. Waasmaier, D.; Kirfel, A. *Acta Crystallogr. A.* **1995**, *51*, 416–430.

28. Kovacs, J. A.; Brines, L. M. *Acc. Chem. Res.* **2007**, *40*, 501–509.

29. Kitagawa, T.; Dey, A.; Lugo-Mas, P.; Benedict, J. B.; Kaminsky, W.; Solomon, E. I.; Kovacs, J. A. *J. Am. Chem. Soc.* **2006**, *128*, 14448-14449.

30. Stoll, S.; Schweiger, A. *J. Magn. Reson. Ser. A* **2006**, *178* (1), 42–55.

31. Kennepohl, P.; Neese, F.; Schweitzer, D.; Jackson, H. L.; Kovacs, J. A.; Solomon, E. I. *Inorg. Chem.* **2005**, *44*, 1826-1836.

32. Lugo-Mas, P.; Dey, A.; Xu, L.; Davin, S. D.; Benedict, J.; Kaminsky, W.; Hodgson, K. O.; Hedman, B.; Solomon, E. I.; Kovacs, J. A. *J. Am. Chem. Soc.* **2006**, *128*, 11211–11221.

33. Lu C. C.; Bill E.; Weyhermüller, T.; Bothe, E.; Wieghardt, K. *J. Am. Chem. Soc.* **2008**, *130*, 3181–3197.

34. Glaser, T.; Hedman, B.; Hodgson, K. O.; Solomon, E. I. *Acc. Chem. Res.* **2000**, *33*, 859–868.

35. Solomon, E. I.; Szilagyi, R. K.; DeBeer George, S.; Basumallick, L. *Chem. Rev.* **2004**, *104*, 419–458.

36. Dey, A.; Jenney, F. E.; Adams, M. W.; Johnson, M. K.; Hodgson, K. O.; Hedman, B.; Solomon, E. I. *J. Am. Chem. Soc.* **2007**, *129*, 12418–12431.

37. Rose, K.; Shadle, S. E.; Eidsness, M. K.; Kurtz, D. M.; Scott, R. A.; Hedman, B.; Hodgson, K. O.; Solomon E. I. *J. Am. Chem. Soc.* **1998**, *120*, 10743–10747.

38. Neese, F. *Coord. Chem. Rev.* **2009**, *253*, 526–563.

39. Ogliaro, F.; de Visser, S. P.; Shaik, S. *J. Inorg. Biochem.* **2002**, *91*, 554–567.

40. Yoshioka, S.; Takahashi, S.; Ishimori, K.; Morishima, I. *J. Inorg. Biochem.* **2000**, *81*, 141–151.

41. Sazama, G. T.; Betley, T. A. *Inorg. Chem.* **2010**, *49*, 2512–2524.

42. Sazama, G. T.; Betley, T. A. *Inorg. Chem.* **2014**, *53*, 269–281.

43. Que, L. *Physical Methods in Bioinorganic Chemistry*; University Science Books: Sausalito, CA, 2000.

44. Cranshaw, T. E. *J. Phys. E.* **1974**, *7*, 497–505.

45. Harris, D.; Loew, G.; Waskell, L. *J. Am. Chem. Soc.* **1998**, *120*, 4308–4318.

46. Ye, S.; Bill, E.; Neese, F. *Inorg. Chem.* **2016**, *55*, 3468–3474.

Chapter 4.

Electronic and Geometric Factors Influencing the Structural Metrics of α-(Imino)-Imidizoles.

Portions of this chapter have been adapted from: Leipzig, B. K.; Rees, J. A.; Nyrov, A.; Theisen, R.; Flowers, S. E.; Kaminsky, W.; DeBeer, S.; Kovacs, J. A. *In Preparation*.[1]

Introduction:

Redox-active ligands will have bond lengths that elongate and shorten due to the amount of electron density within the molecular orbitals. The structural and spectroscopic data for **10**-**12** suggests there is unusual electronic activation of the ligand framework that may be, in part, due to the effect of the thiolate and the low-spin state of the ferrous metal center. The bond lengths are suggestive either of significant π-backbonding or a reduction of the imine backbone. Preparation of a number of complexes with this ligand environment can help highlight the major factors that influence the redistribution of electron density.

A reduction could be caused by an electron transfer from the metal redox orbital to the ligand π^*-orbital.[2,3] For this to occur the ligand π^* orbitals were to fall lower in energy than the filled metal orbitals. The incorporation of a coordinated thiolate could buffer the electron density on the metal, lower the redox potential and, as a π-donor, raise the energy of the metal t_{2g}-like orbitals.[4,5] Alternatively, backbonding from the metal to the imine π^* orbital has been observed previously and is possible in this system.[1] This will be heavily influenced by the electronic arrangement of the metal's *d* orbital electrons. Additionally, the thiolate could also play a significant role and push electron density into the metal *d* orbitals, which in turn donate onto the π-accepting imine bond. This would be akin to the "push" effect in cytochrome P450.[6,7]

Altering the electronic configuration and the number of electron pair's was accomplished by oxidation reactions, and the sole crystalized example of this, $\mathbf{12^{ox}}$, showed no change in the intra-ligand bond lengths, potentially indicating the influence of the coordinating thiolates. To assess the importance of the configuration, different metal complexes were synthesized. The effect of the thiolate was investigated with two complexes that do not incorporate a coordinated thiolate.

Experimental:

General Considerations: DMSO-d_6 and $CDCl_3$ were purchased from Cambridge Isotope Labs and used as received. EtOH was purchased from Decon and degassed prior to use. Et_2O was purchased from Fischer Scientific and purified using solvent purification columns housed in a custom stainless steel cabinet and dispensed by a stainless steel Schlenk-line (GlassContour). All other solvents were purchased from Sigma Aldrich. MeOH, MeCN and CH_2Cl_2 were dried and distilled prior to use. A 48% aqueous solution of hydrobromic acid was purchased from Alfa-Aesar and used as received. Ammonia was obtained from Praxair while all other material was purchased and used as received from Sigma Aldrich.

^{1}H NMR spectra were obtained on a Bruker AV300, AV301, DRX499, or AV500. Chemical shifts are listed in parts per million and were reported relative the residual protio solvent. UV/Vis spectra were recorded on a Varian Cary 50 spectrophotometer equipped with a fiber optic cable connected to a "dip" ATR probe (C-technologies). A custom-built two neck solution sample holder equipped with a threaded glass connector was sized specifically to fit the "dip" probe. Electrospray ionization mass spectrometry (ESI-MS) was preformed on a Bruker Esquire LC-Ion Trap. Cyclic voltammograms (CV were recorded in MeCN (0.1M ^{n}Bu$_4$N[PF_6] supporting electrolyte) on a PAR 263A potentiostat or a CHI 600E electrochemical work station utilizing a classy carbon working electrode, platinum auxiliary electrode and an $Ag^+/AgNO_3$ reference electrode. X-ray crystallographic data was recorded on a Bruker APEX II single crystal X-ray diffractometer using Mo-radiation. Elemental analysis were preformed by Atlantic Microlab, Inc. Norcross, Ga. All manipulations were performed using Schlenk techniques or under a N_2 atmosphere in a glovebox.

Synthesis of $[(Co^{II}(Tame\text{-}N_2SIm_2))_2](PF_6)_2$ (13). **9** (0.2 g, 1 mmol) was added to a vial containing a stirred solution of sodium methoxide (0.156 g, 3 mmol) in methanol (10 mL). 1-methyl-2-imidizolecarboxaldehyde (0.21 g, 2 mmol) was then added and the stirred suspension was cooled to -40° C. In a separate vial cobalt (II) chloride dissolved in MeOH (5mL) and cooled to -40° C. The cobalt solution was then slowly added to the organic solution. This was stirred for 1h, at which time sodium hexafluorophosphate (0.168 g, 1 mmol) was added. This solution was stirred overnight at which time an orange solid had precipitated. The MeOH was removed *in vacuo* and the solid was dissolved in MeCN (2 mL), and filtered through celite. The MeCN was removed to a minimal volume and layered with Et_2O (5 mL) to isolated a red powder in 93% yield (265 mg). A slow diffusion of MeCN:Et_2O X-ray quality crystals λ_{max} (nm) (ε ($M^{-1}cm^{-1}$)): (MeCN): 512 sh (654). Magnetic moment (solution, MeCN, 298K) 3.98μ_B/Co ESI-MS: expected *m/z* for $[C_{30}H_{43}N_{12}S_2Co_2]^{2+}$= 376.1, found *m/z* = 376.2. Elemental Analysis for $C_{30}H_{43}F_{12}N_{12}P_2S_2Co_2$ Calculated: C, 34.56; H, 4.06; N, 16.12. Found: C, 34.41; H, 4.04; N; 15.95.

Synthesis of $[(Co^{III}(Tame\text{-}N_2SIm_2))_2](PF_6)_4$ (13^{ox}). **13** (55mg , 0.05 mmol) was dissolved in MeCN (5 mL). To this, stoichiometric amounts $[Fc]PF_6$ (35mg, 0.1mmol) per cobalt was added. This solution was allowed to stir for 15h, after which the volatiles were evaporated. The resulting red solid was washed with Et_2O (3 x 4 mL) to yield a yellow filtrate containing the Fc byproduct. The red precipitate was once again dissolved in MeCN (1 mL), and layered with Et_2O (3 mL) and cooled in a freezer (-40° C). Red crystals were obtained in 71% yield (50 mg). ^{1}H NMR (300 MHz, MeCN-*d*$_3$) δ 8.62 (s, 1H), 8.97 (s, 1H) 8.35, (S, 1H), 7.57 (s, 1H), 7.43 (s,

1H), 7.10 (s, 1H), 6.48 (s, 1H) 4.08 (s, 6H), 3.76 (m, 2H), 3.51 (m, 2H), 1.25 (s, 3H), 1.05(d, ^2J =15 Hz, 1H), 0.91 (d, ^2J = 15 Hz, 1H).

Synthesis of Thioether-ligated [Fe^{II}(tame-(N_2S^{Bz}(^{Me}Im)$_2$(MeCN))] (PF_6)$_2$ (14). 6 (0.1 g, 0.44 mmol) was added to a vial and dissolved in MeOH (8 mL). 1-methyl-2-imidizolecarboxaldehyde (0.1 g, 0.88 mmol) was then added and the solution was cooled to -40° C. In a separate vial iron (II) chloride (0.055 g, 0.44 mmol) was dissolved in MeOH (3 mL) and cooled to -40° C. The iron solution was then slowly added to the organic solution. Immediately, the solution became red. This was stirred for 1h at which time sodium hexafluorophosphate (0.148 g, 0.88 mmol) was added. The MeOH was removed *in vacuo* and the solid was dissolved in MeCN (2 mL), and filtered through celite. The red solution was concentrated to a minimal volume (2ml) upon which Et_2O (5 mL) was layered to isolate a deep red solid in 45% yield (150 mg). λ_{max} (nm) (ε ($M^{-1}cm^{-1}$): (MeCN): 512 (2850). Magnetic moment (solution, MeCN, 298K) 5.04μ_B Elemental Analysis for $C_{24}H_{31}F_{12}N_7P_2SFe$ Calculated: C, 36.24; H, 3.93; N, 12.33 Found: C, 35.74; H, 3.97; N; 12.41.

Synthesis of [Mn^{II}(tame-(N_2S(^{Me}Im)$_2$Cl] (PF_6) (15). 9 (0.2 g, 1 mmol) was added to a vial containing a stirred solution of sodium methoxide (0.156 g, 3 mmol) in MeOH (10 mL). 1-methyl-2-imidizolecarboxaldehyde (0.21 g, 2 mmol) was then added and the stirred suspension was cooled to -40° C. In a separate vial manganese (II) chloride dissolved in MeOH (5 mL) and cooled to -40° C. The manganese solution was then slowly added to the organic solution. This was stirred for 1h, at which time sodium hexafluorophosphate (0.168 g, 1 mmol) was added. This solution was stirred for 15h, at which time a white solid precipitated. The MeOH was

removed *in vacuo* and the solid was dissolved in MeCN (5 mL), and filtered through celite. This was reduced to 1 ml, layered with Et_2O (3 ml) and cooled to -40° C for 48h. White crystals were isolated in 70% yield (193 mg). A slow diffusion of MeCN:Et_2O yielded X-ray quality crystals. ESI-MS: expected *m/z* for $[C_{30}H_{43}N_6SMn]^{2+}$= 372.1, found *m/z* = 372.1.

X-Ray Crystallographic Structure Determination

A red piece, **13,** measuring 0.15 x 0.05 x 0.05 mm^3 was mounted on a loop with oil. Data was collected at -173°C on a Bruker APEX II single crystal X-ray diffractometer, Mo-radiation. Crystal-to-detector distance was 40 mm and exposure time was 5 seconds per frame for all sets. The scan width was 0.5°. Data collection was 99.9% complete to 25° in ϑ. A total of 107396 reflections were collected covering the indices, h = -15 to 15, k = -18 to 18, l = -25 to 25. 15125 reflections were symmetry independent and the R_{int} = 0.0643 indicated that the data was of better than average quality (0.07). Indexing and unit cell refinement indicated a triclinic lattice. The space group was found to be P $\bar{1}$ (No. 2).

A clear red prism, **13^{ox}**, measuring 0.12 x 0.03 x 0.03 mm^3 was mounted on a loop with oil. Data was collected at -173°C on a Bruker APEX II single crystal X-ray diffractometer, Mo-radiation. Crystal-to-detector distance was 40 mm and exposure time was 240 seconds per frame for all sets. The scan width was 0.5°. Data collection was 99.8% complete to 25° in ϑ. A total of 34803 reflections were collected covering the indices, h = -15 to 15, k = -22 to 22, l = -19 to 27. 10456 reflections were symmetry independent and the R_{int} = 0.2136 indicated that the data was of less than average quality (0.07). Indexing and unit cell refinement indicated a primitive orthorhombic lattice. The space group was found to be P 21 21 21 (No.19).

A purple block, **14**, measuring 0.08 x 0.03 x 0.03 mm^3 was mounted on a loop with oil. Data was collected at -173°C on a Bruker APEX II single crystal X-ray diffractometer, Mo-radiation. Crystal-to-detector distance was 40 mm and exposure time was 30 seconds per frame for all sets. The scan width was 0.5°. Data collection was 99.2% complete to 25° in ϑ. A total of 21050 reflections were collected covering the indices, h = -13 to 13, k = -15 to 15, l = -15 to 15. 6841 reflections were symmetry independent and the R_{int} = 0.0820 indicated that the data was of average quality. Indexing and unit cell refinement indicated a triclinic lattice. The space group was found to be P $\bar{1}$ (No. 2).

A colorless prism, **15**, measuring 0.03 x 0.01 x 0.01 mm^3 was mounted on a loop with oil. Data was collected at -173°C on a Bruker APEX II single crystal X-ray diffractometer, Mo-radiation. Crystal-to-detector distance was 40 mm and exposure time was 240 seconds per frame for all sets. The scan width was 1.0°. Data collection was 99.3% complete to 25° in ϑ. A total of 13868 reflections were collected covering the indices, h = -9 to 9, k = -13 to 13, l = -17 to 17. 4521 reflections were symmetry independent and the R_{int} = 0.1009 indicated that the data was appropriate. Indexing and unit cell refinement indicated a triclinic lattice. The space group was found to be P -1 (No.2).

All data was integrated and scaled using SAINT, SADABS within the APEX2 software package by Bruker.[8] All solution by direct methods (SHELXS, SIR97[9,10]) produced a complete heavy atom phasing model consistent with the proposed structure. The structure was completed by difference Fourier synthesis with SHELXL97.[11,12] Scattering factors are from Waasmair and Kirfel.[13] Hydrogen atoms were placed in geometrically idealised positions and constrained to ride on their parent atoms with C---H distances in the range 0.95-1.00 Angstrom. Isotropic thermal parameters U_{eq} were fixed such that they were $1.2U_{eq}$ of their parent atom Ueq for CH's

and 1.5U_{eq} of their parent atom U_{eq} in case of methyl groups. All non-hydrogen atoms were refined anisotropically by full-matrix least-squares. Crystal Data is presented in **Table 4.01**.

Table 4.01: Crystallographic data for **13-15** and **13^{ox}**.

	13	**13^{ox}**	**14**	**15**
Formula	$C_{30}H_{42}Co_2F_{12}N_{12}P_2S_2$	$C_{30}H_{42}Co_2F_{24}N_{12}P_4S_2$	$C_{26}H_{34}F_{12}FeN_8PS$	$C_{17}H_{25}ClF_6MnN_7PS$
MW (g/mol)	1165.84	1470.93	836.46	594.86
Crystal System	Triclinic	Orthorhombic	Triclinic	Triclinic
Space Group	P-1	P 21 21 21	P-1	P-1
Unit Cell	**Dimensions**			
a (Å)	10.9597(3)	13.1337(12)	11.2287(11)	7.8232(12)
b (Å)	13.0171(4)	18.726(2)	12.2948(13)	11.4274(16)
c (Å)	17.9975(5)	22.973(3)	12.7375(14)	14.851(2)
α (deg)	93.948(2)	90	88.369(5)	70.691(9)
β (deg)	102.099(2)	90	74.465(5)	88.291(9)
γ (deg)	95.177(2)	90	84.959(5)	82.748(10)
Final R indices	0.0374	0.0712	0.0598	0.0602
R indices (all Data)	0.0657	0.2034	0.1222	0.1268

Results and Discussion:

*Cobalt Derivative of **12**:*

Variation of the d-electron count was accomplished by isolating a cobalt derivative of **12**. This Co complex, **13**, was synthesized in the same Schiff base condensation as **12** (Chapter 2) and shown to form a similar C_2 symmetric dimer in the solid state (**Figure 4.01**). The Co-ligand bond lengths are consistent with a high-spin Co (II) metal ion. Unlike the Fe complexes, that have a very uniform bis-μ-thiolate core, **13** does not. One Co-S bond length is much shorter (2.393(1) Å) than the other Co-S bond (2.465(1) Å). This lengthening of the bridging Co may allow more facile cleavage of this dimeric structure. In addition to the asymmetry of the bond

lengths, the Co_2S_2 core is much more puckered as observed by a much larger calculated least squares plane fit. The distance between the M-M and S-S centroids is 0.72 Å for **13** whereas it is 0.34 Å for the Fe_2S_2 core of **12** (**Table 4.02**).

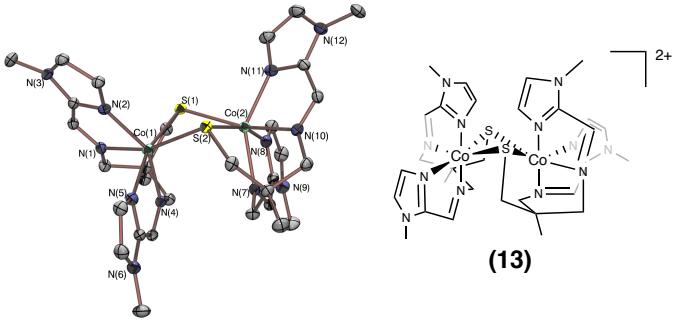

Figure 4.01: X-ray crystal structures of **13** with 50% probability ellipsoids. Counterions, cosolvents and hydrogens omitted for clarity (Left). Corresponding structural representations (Right).

Table 4.02: Selected Metal-ligand bond lengths and metrical parameters for **13** and **13^{ox}**.

Bonds	13	13^{ox}
Co-S(1)	2.393(1)	2.229(3)
Co-S(2)	2.465(1)	2.232(3)
Co-N(1)	2.162(2)	1.903(8)
Co-N(2)	2.121(2)	-
Co(1)-N(3)	-	1.934(8)
Co(1)-N(4)	2.145(2)	-
Co(1)-N(5)	2.141(2)	1.934(8)
Co(1)-N(6)	-	1.898(8)
Co(2)-S(1)	2.462(1)	2.225(3)
Co(2)-S(2)	2.391(1)	2.226(3)
Co(2)-N(7)	2.123(2)	1.891(9)
Co(2)-N(8)	2.156(2)	-
Co(2)-N(9)	-	1.953(7)
Co(2)-N(10)	2.209(2)	-
Co(2)-N(11)	2.121(2)	1.915(8)
Co(2)-N(12)	-	1.924(8)
Least square fit Co_2S_2	0.34	0.15

A solution state magnetic moment of 3.98 BM would be consistent with a high spin Co(II) metal ion and be indicative of either a monomeric species, where the bridging thiolates are cleaved in solution, or dimeric species, with no coupling through this puckered core. The high-spin state of the Co complex seems to influence the intra-ligand bond lengths. Unlike Fe complexes **10-12**, this Co complex has a very short average imine bond length of 1.276 Å (**Table 4.03**). This contraction of the imine bond may, in part, be a result of the change in electronic configuration and will be discussed further in this chapter. While the Fe complexes have intense electronic absorption features in the visible region, **13** has only a small shoulder at 512 nm with a much smaller extinction coefficient of around 600 $M^{-1}cm^{-1}$ (**Figure 4.02**). If mixing of the sulfur contributes to the large intensity seen in complexes **10-12**, then the weakening of the orbital overlap by the distorted geometry of the **13** could cause the intensity to decrease significantly.

Table 4.03: Intra-ligand bond lengths for **13** and **13^{ox}**.

	13 (Å)		**13^{ox} (Å)**
N(1)-C(5)	1.275(2)	**N(5)-C(5)**	1.277(10)
C(5)-C(6)	1.447(3)	**C(5)-C(3)**	1.458(13)
N(4)-C(11)	1.274(2)	**N(6)-C(11)**	1.293(12)
C(11)-C(12)	1.449(3)	**C(11)-C(13)**	1.431(14)
N(7)-C(20)	1.283(2)	**N(11)-C(20)**	1.316(12)
C(20)-C(21)	1.442(3)	**C(20)-C(19)**	1.427(13)
N(10)-C(26)	1.272(2)	**N(12)-C(26)**	1.309(11)
C(26)-C(27)	1.451(3)	**C(26)-C(28)**	1.373(12)

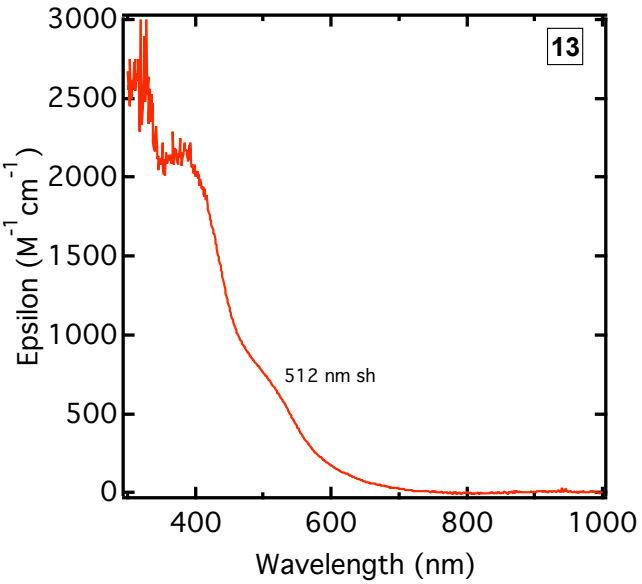

Figure 4.02: Electronic absorption of **13** in MeCN at RT.

Although there could be monomeric species in solution, the electrochemical CV shows two reversible features at $E_{1/2}$=-466mV and $E_{1/2}$=-824mV vs. Fc/Fc^{+} (**Figure 4.03**). Since there are two reversible features, one possibility exists that the dimer is present in solution. The first oxidation would form a mixed valent Co^{II}-Co^{III} species with the second oxidation forming a Co^{III}-Co^{III} dimeric species. Since there is no geometric change to this dimeric species upon oxidation, a reversible feature would be expected with each oxidation at different potentials. A monomeric Co(II) species would be unlikely to have two reversible features. An electrochemical oxidation would likely result in a Co(III) species, which would most likely have a spin-state change to a low-spin electronic configuration. Chemically, a low-spin Co(III) would typically prefer to be six coordinate and bind an MeCN solvent molecule. This type of oxidation would be unlikely to maintain the geometry throughout the electrochemical experiment which would probably involve an irreversible reduction event. However, this complex is ligated by a thiolate, which may stabilize a coordinatively unsaturated five coordinate Co(III) complex, as has been observed previously our group before and accounts for the reversible reduction feature.[14,15] The

observance of two sequential reversible features seem unlikely to portend a monomeric species in solution.

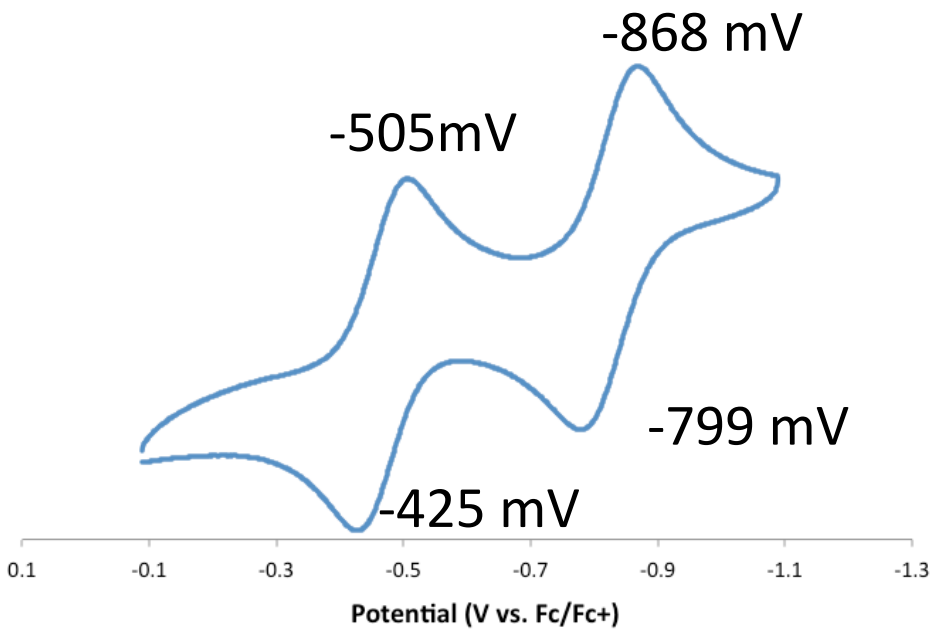

Figure 4.03: 1mM Cyclic voltamagram of **13** at RT. Scans taken in MeCN at 0.1V/s with a glassy carbon working electrode and platinum counter electrode. Scan from 1 V to -1 V and potentials referenced to Fc/Fc^{+} and a 0.1M solution of $^{n}Bu_4N[PF_6]$ supporting electrolyte.

Similar to the Fe complexes, there seems to be a large reduction feature at more negative values (**Figure 4.04**). There is a cathodic peak potential, E_{pc}, of -1.59V and a very small anodic peak potential, E_{pa}, of -1.44V. The anodic and cathodic peak current for these two features (I_{pc} and I_{pa} respectfully) are clearly indicative of an irreversible process. As seen with the Fe complexes, this irreversible feature may be due to the change in the chemical environment due to the change from a π-acceptor imine orbital to a π-donating amide ligand. There is a significant decrease in the energy required to reduce this complex compared to the analogous ferrous complex **12**, this trend seems to hold based on the limited electronic activation of the imine and will be discussed later.

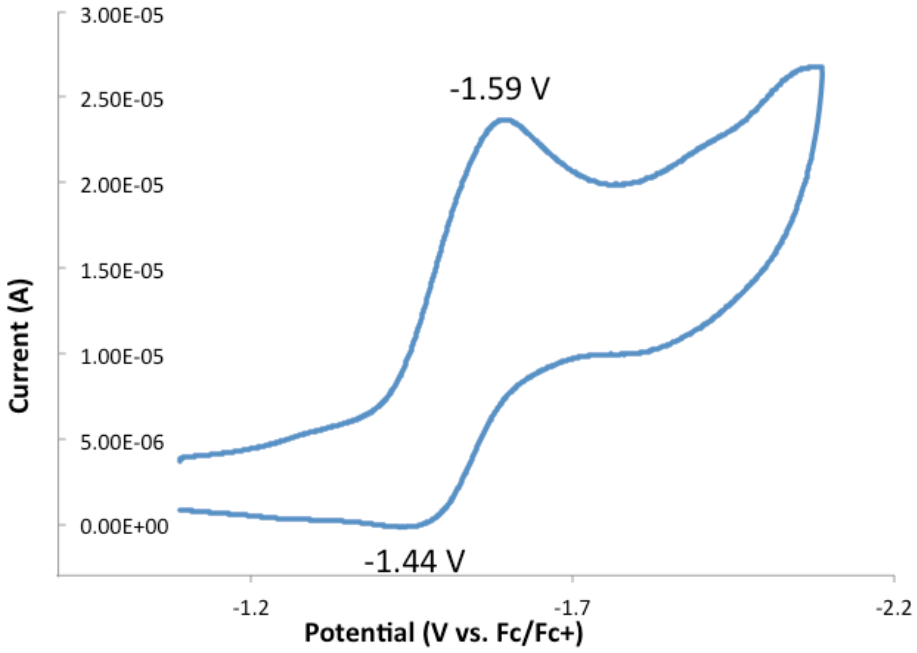

Figure 4.04: 1mM Cyclic voltamagram of **13** at RT. Scans taken in MeCN at 0.1V/s with a glassy carbon working electrode and platinum counter electrode. Scan from -1.1V to -2V and potentials referenced to Fc/Fc^+ and a 0.1M solution of $^nBu_4N[PF_6]$supporting electrolyte.

A small change is observed in the electronic absorption spectrum when 2 equivalents of Fc^+ are added to the dimeric **13**. However, a clear indication that the desired reaction took place was observed by ^1H NMR spectroscopy, where an observed diamagnetic product is consistent with a low-spin Co(III) species (**Figure 4.05**). The peaks in the ^1H NMR spectrum are consistent with two unique imidazole arms, similar to the C_2 symmetric **10**. The imine protons are observed at 8.54 and 8.26 ppm while four distinct aromatic peaks are observed at 7.57, 7.42, 7.04 and 6.46 ppm. There are two unique methyl groups on the imidazole rings which are seen as two singlets at 4.09 and 4.06 ppm while a multiplet between 3.70 and 3.39 ppm is the result of the methylene protons adjacent to the nitrogen of the imine. Finally, a singlet at 1.20 ppm would be consistent with the methyl group on the tame backbone and two roofing doublets at 0.92 and 0.82 ppm are the result of the protons of the methylene adjacent to the thiolate.

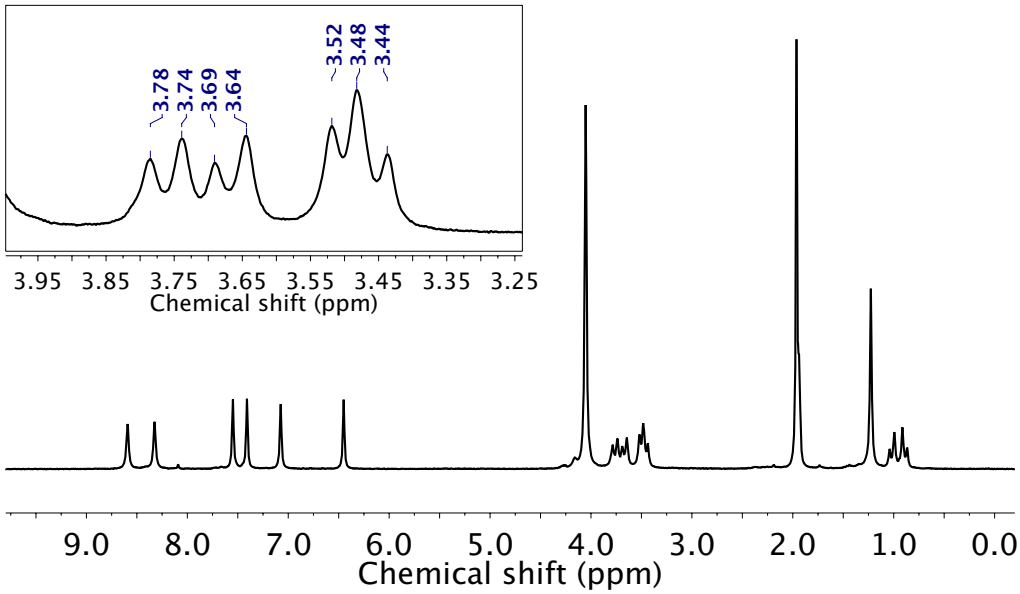

Figure 4.05: ^{1}H NMR spectrum of **13^{ox}** in MeCN at RT**.**

The solid-state structure was verified crystallographically (**Figure 4.06**). In the solid state, this complex, **13^{ox}**, has the same C_2 symmetry as the reduced version, **13**, and is consistent with the splitting pattern observed in the ^{1}H NMR spectrum (**Figure 4.05**). There is a noticeable decrease in the Co-N bond lengths compared to **13**. On average the Co-N bond length decreased from 2.15 Å in the high spin Co(II) of **13** to 1.92 Å in **13^{ox}** (**Table 4.02**). This suggests that, not only has the Co been oxidized to Co(III), but also that it is low-spin, consistent with the diamagnetic NMR spectrum. This low-spin Co(III) complex would be isoelectronic to the low spin ferrous derivative **12**. Similarly, the thiolate bond lengths contract with bond lengths ranging from 2.225(3) to 2.232(3) Å. In addition to the shorter Co-S bond lengths, the asymmetry of the Co_2S_2 core that was observed in **13** is now much more symmetric for the oxidized product. Finally, unlike **13**, **13^{ox}** has a very planar Co_2S_2 suggesting a more octahedral like structure and better π-overlap between the Co and ligands with the least square plane fit now 0.15 (0.35 in **13**) (**Figure 4.07**).

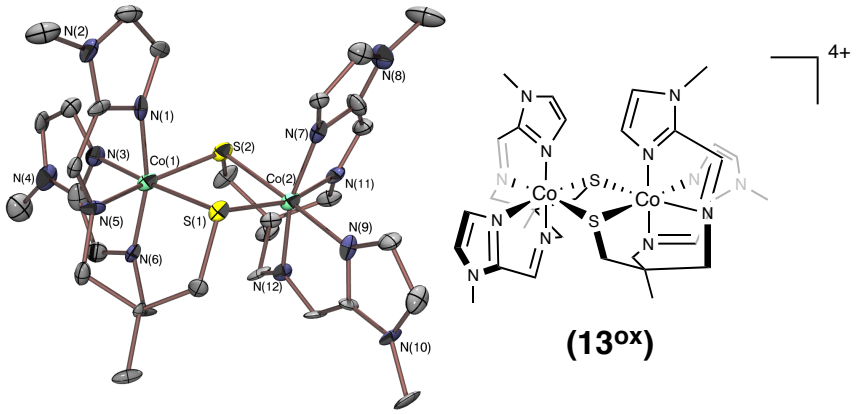

Figure 4.06: X-ray crystal structures of **13**^{ox} with 50% probability ellipsoids. Counterions, cosolvents and hydrogens omitted for clarity (Left). Corresponding structural representations (Right).

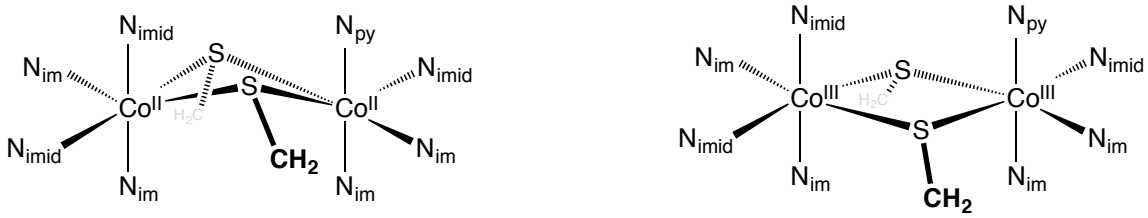

13 **13**^{ox}

Figure 4.07: chemdraw depiction of the four atom core (Co_2S_2) of **13** and **13**^{ox} indicating the methyl carbon adjecent to the thiolates.

While the contraction of the Co-ligand bond lengths are expected, the lengthening of the imine bonds are somewhat unexpected. Around Co(1) the two imine bond lengths are 1.277(10) and 1.293(12) Å suggesting some activation when compared to **13** (**Table 4.03**). However, the imine bond lengths are lengthened around Co(2), with an imine bond length of 1.309(11) and 1.316(12) Å indicating a possible activation of this ligand fragment.

The observed ligand bond lengths in **12, 13** and **13**^{ox} can be explained through the differences in both spin state and geometry around the metal ion. It seems that the low-spin state of **12** and **13**^{ox} suggests that the metal ion is capable of backbonding into the π^* imine orbital.

Conversely, **13** has a high spin state and fewer electron pairs (one t_{2g}-obrital is half filled) in metal orbitals capable of backbonding into the accepting imine orbital. Additionally, angular orbital overlap between the π-donating thiolate into the metal ion would be increased as the M_2S_2 core becomes more planar. This increases a "push"-like π-effect from the donating thiolate through the metal orbital and out into the imine π^* orbital. The bent nature of **13** hinders the thiolate ability to donate electron density and activate these ligands. A shorter M-thiolate distance will increase the effect of the thiolate and it is seen that **13**, which has no activation and the longest M-S bond lengths has the least activated intra-ligand bond lengths.

These properties are important to keep in mind when designing future base-metal catalysts. An important feature in these redox-active ligand frameworks is the ability for the ligand to mitigate the amount of electronic demand at the metal center.[16] This will afford 2 e^- redox chemistry for 1st row transition metals which typically undergo sequential 1 e^- redox reactions. This case study indicates that the addition of strong π-donating ligands may be able to influence the amount of electronic activation of the ligands and aid future catalysts in the efficiency of using both redox reservoirs.

The ability for the thiolate to modulate electron density into other ligand orbitals is proposed in the mechanism of cytochrome P450. A critical step is the heterolytic cleavage of the O-O bond which is aided by the "push"-effect of the axial cysteinate.[17,18] The thiolate will donate electron density through the π-framework of the metal and into the peroxide σ^*-orbital, weakening the O-O bond. Even though this density is pushed into a σ^*-bond, it has π overlap with the metal orbitals. Using redox-active ligands that will accept electron density and have changes in bond lengths allows observation of a thiolate effect.

Thiolate Effect:

In order to specifically investigate the importance of the thiolate, a benzyl protected thioether complex, **14**, was synthesized. This complex was prepared using the diamine benzyl protected organic precursor, **6** (**Figure 4.08**). A similar Schiff base condensation yields a monomeric ferrous complex. The geometry of this thioether complex is square pyramidal with the two α-(imino)-imidizoles in the basal plane and an axial thioether (**Figure 4.08**). As evidenced by the Fe-N bond lengths (all < 2.0 Å) and a short Fe-S bond length of 2.27 Å, the ferrous ion appears to be in a low-spin *S*=0 state (**Table 4.04**). However, the ^{1}H NMR spectrum of **14** at room temperature did not display the expected diamagnetic signals; instead, paramagnetically shifted peaks were observed. This could be readily rationalized by solvent dissociation at higher temperatures, however a solution magnetic moment μ_{eff} = 5.04 μ_B by Evan's method suggests a high-spin state in solution. Difference in spin states between solution state and solid state crystal structures are seen in the literature and could be due to the differences in the temperature of these two experimental techniques.[19]

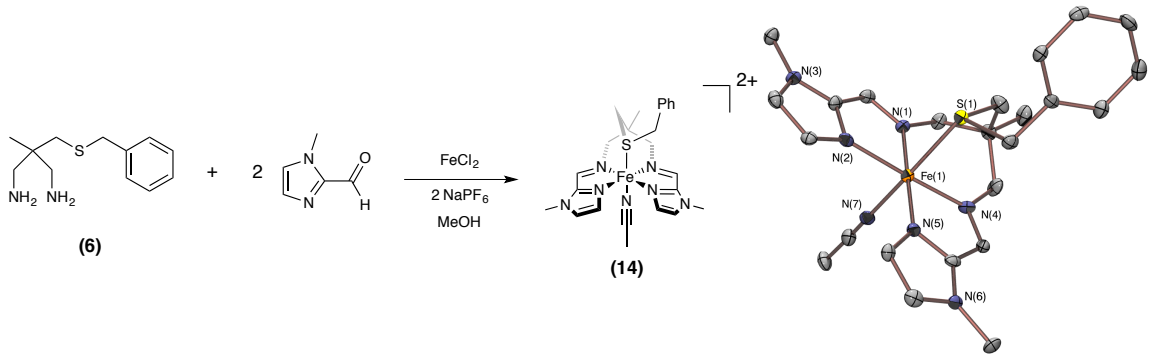

Figure 4.08: Reaction of **6** and 1-methyl-2-imidizolecarboxaldehyde to produce **14** and Corresponding structural representations (Left). X-ray crystal structures of **14** with 50% probability ellipsoids. Counterions, cosolvents and hydrogens omitted for clarity (Right).

Table 4.04: Metrical parameters for **14**.

Metal-Ligand Distances	14 (Å)
Fe-S(1)	2.275(13)
Fe-N(1)	1.948(4)
Fe-N(2)	1.996(4)
Fe-N(4)	1.941(4)
Fe-N(5)	1.981(4)
Fe-N(7)	1.947(4)
Intra-Ligand Distances	
N(1)-C(6)	1.281(5)
C(6)-C(7)	1.432(6)
N(4)-C(12)	1.287(5)
C(12)-C(13)	1.436(6)

Since **14** shares a similar solid-state metal spin state to **12**, the only difference is the change from other ligands, which alters the activation of the intra-ligand bond lengths (**Table 4.04**). The substitution of a neutral L-type thioether for a π-donating anionic thiolate indicates the importance of the thiolate in ligand activation. It seems that, in the right geometry, the thiolate can "push" electron density through the metal t_{2g}-like orbitals into the π-accepting ligand orbital.

Furthermore, while **14** retains a CT transition in the visible region of the electronic absorption spectrum, it is to higher energy and much lower intensity ((λ_{max}(ε, $M^{-1}cm^{-1}$)= 512 (2850)) nm when compared to that of thiolate-ligated **12** ((λ_{max}(ε, $M^{-1}cm^{-1}$)= 619 (11500)) nm. An interpretation of this spectra is that the there is no longer any thiolate-mixing that was observed by DFT for **12**. These differences in the C-N imine bond and the C-C bond metrical parameters, as well as electronic absorption spectra, suggest that the thiolate ligand plays a critical role in promoting the intense optical transitions and distinct intra-ligand metrical parameters observed for **10-12.**

The electrochemistry of **14** is indicative of the difference between thiolate ligation and thioether ligation. A fairly reversible feature is observed at 480 mV vs. Fc/Fc^{+} (**Figure 4.09**).

The more positive reduction potential is expected as the overall charge of the complex is more positive. In addition the thiolate will lower the reduction potential, as has been observed with other systems. Also, unlike **10-12** which had multiple features, this monomeric ferrous complex only has one. Similar to **13**, there is a noticeable shift to higher potentials for the E_{pc} which is observed, at -1.68 V (**Figure 4.10**). There seems to be an E_{pa} at -1.28 V that is dependent on the initial cathodic feature.

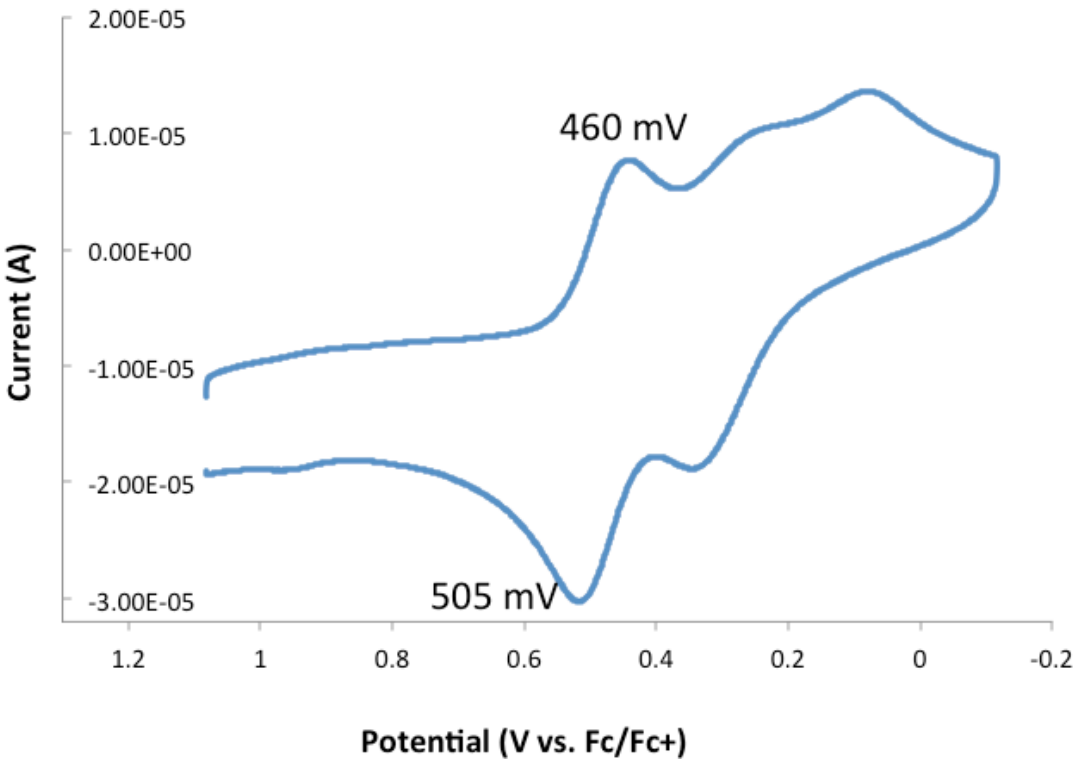

Figure 4.09: 1 mM Cyclic voltamagram of **14** at RT. Scans taken in MeCN at 0.1 V/s with a glassy carbon working electrode and platinum counter electrode. Scan from 1.1 V to -0.1 V and potentials referenced to Fc/Fc^{+} and a 0.1 M solution of $^{n}Bu_4N[PF_6]$ supporting electrolyte.

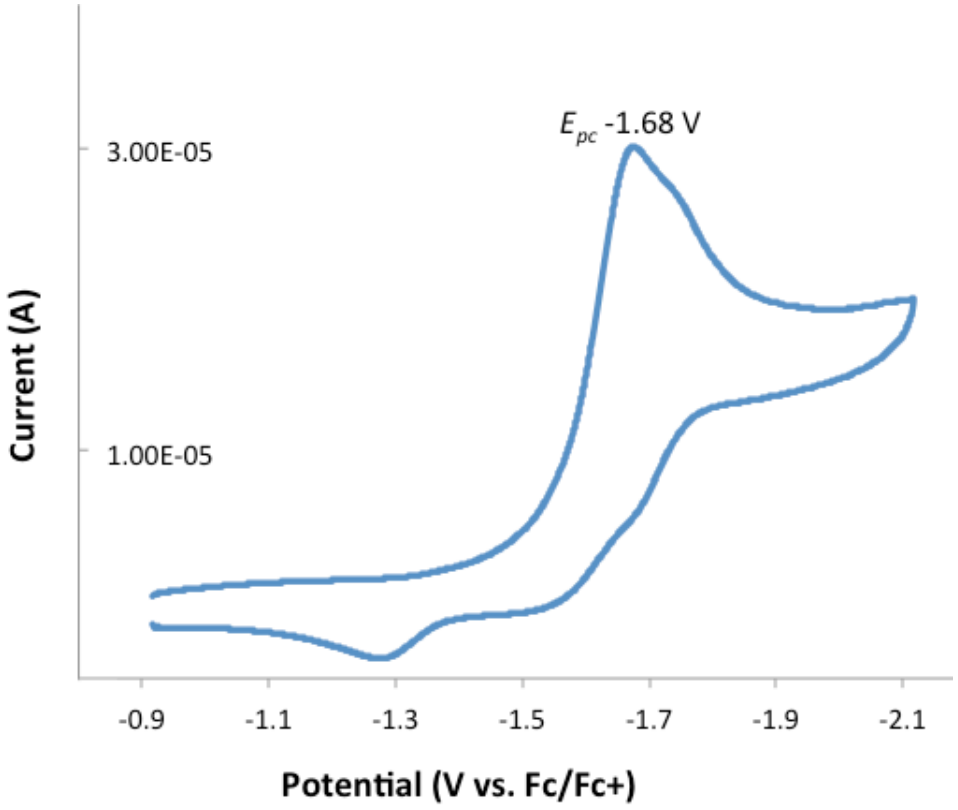

Figure 4.10: 1 mM Cyclic voltamagram of **14** at room temperature (left). Scans taken in MeCN at 0.1 V/s with a glassy carbon working electrode and platinum counter electrode. Scan from -0.8 V to -2.1 V and potentials referenced to Fc/Fc^{+} and a 0.1 M solution of $^{n}Bu_4N[PF_6]$ supporting electrolyte.

*A Manganese derivative of **12**:*

Using $MnCl_2$ in an analogous procedure to the one that was used to isolate **12** and **13**, afforded an unusual complex, **15**. A white solid was isolated, which had a parent peak at 372.1 m/z^{+}, that is consistent with the desired monomeric Mn(II) with the fully condensed ligand present. This product seemed to have no reactivity with O_2, which is in stark contrast to our related Mn(DPEN) system.[20,21] Typically our thiolates afford low reduction potentials that aid in the reactivity of these complexes with O_2. Although as we observed with the analogous Fe complex **10**, there is a possibility that a dimer could be formed, which would leave no open site for O_2 to perform inner-sphere oxidation.

The cyclic voltamagram shows small anodic features that could be the Mn^{III}-Mn^{II} redox couple but they are at high potentials (over 1V vs. Fc/Fc^{+}). This high oxidation potential is unlike similar thiolate ligated Mn complexes that our group has reported.[19,22] This is consistent with the observed lack of O_2 reactivity. However like the **13** and **14** complex, this Mn complex has an E_{pc} of -1.58V which is a more positive compared to **12** and is assigned as the ligand reduction (**Figure 4.11**).

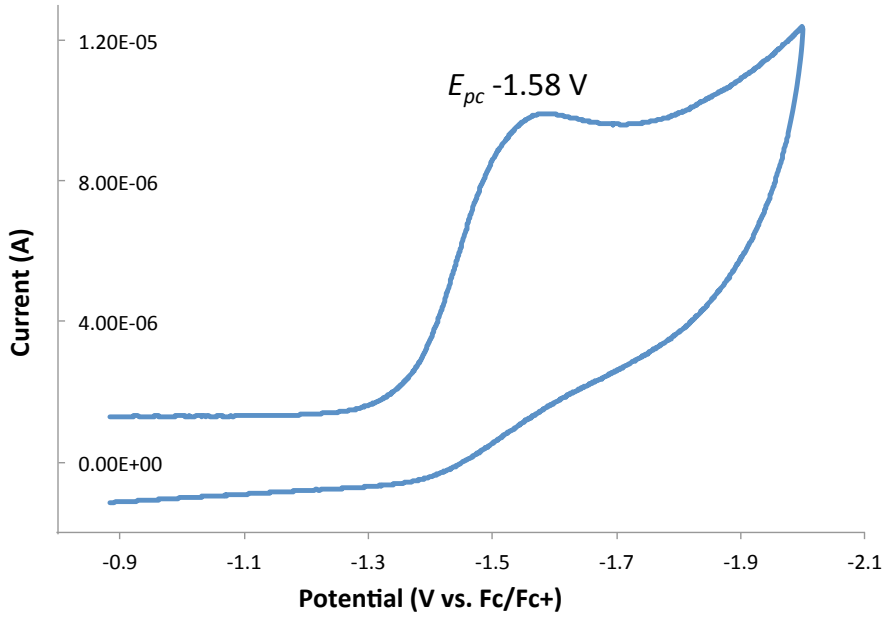

Figure 4.11: 1 mM Cyclic voltamagram of **15** at RT. Scans taken in MeCN at 0.1V/s with a glassy carbon working electrode and platinum counter electrode. Scan from 0 V to -2 V and potentials referenced to Fc/Fc^{+} and a 0.1 M solution of $^{n}Bu_4N[PF_6]$ supporting electrolyte.

A solid-state structure showed that, unlike **12** and **13**, the thiolate does not coordinate to the metal center. It appears that during the Schiff base condensation reaction, the thiolate nucleophillically attacked a carbon forming a six-membered ring and a new C-S bond (**Figure 4.12**). These Mn-ligand bond lengths suggest a high spin Mn ion. There is still a Cl coordinated to the Mn to maintain a distorted trigonal bipyramidal geometry (τ value of 0.072) (**Table 4.05**).

This unexpected thiolate reactivity explains the observed electrochemical patterns and the O_2 reactivity.

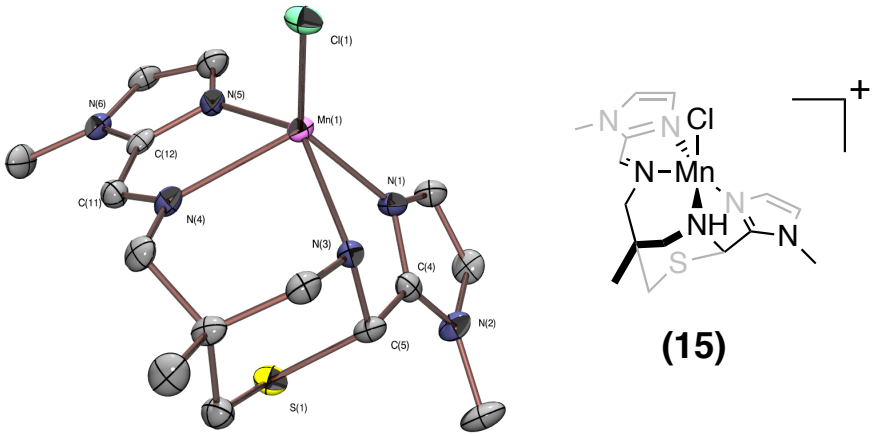

Figure 4.12: X-ray crystal structures of **15** with 50% probability ellipsoids. Counterions, cosolvents and hydrogens omitted for clarity (Left). Corresponding structural representations (Right).

Table 4.05: Selected metrical parameters for **15**

Metal-ligand Bond Lengths	15 (Å)
Mn-N(1)	2.215(4)
Mn-N(3)	2.328(4)
Mn-N(4)	2.366(4)
Mn-N(5)	2.178(4)
Mn-Cl(1)	2.4128(15)
Intra-Ligand Bond Lengths	
N(3)-C(5)	1.468(6)
C(5)-C(4)	1.482(7)
S(1)-C(5)	1.836(5)
N(4)-C(11)	1.275(6)
C(11)-C(12)	1.443(7)
τ value	0.072

The unusual reactivity of the thiolate generates two noticeably different C-N bond lengths. The nucleophilic attack of the sulfur prevents imine formation and it is reflected in an elongated C-N bond. This bond length of 1.468(6) Å is similar to an expected C-N single bond.[2] The other side of this molecule contains an intact α-(imino)-imidazole with no coordinated sulfur

and its bond length is similar to an unactivated imine bond of 1.275(6) Å and a longer 1.443(7) Å C-C bond.

The effect of the thiolate itself was observed in both the **14** and **15**. **14** structurally seems to be isoelectronic to the family of Fe-thiolate complexes. The only difference between these is the variation between the π-donating anionic thiolate to the L-type coordinated thioether. As observed, the imine bond length contracts compared to the related thiolate complex. While the electronic geometry of **12** and **14** in the solid state are equivalent, suggesting that the backbonding effect of the metal is similar the thioether will have significantly less push-effect from the thiolate and this is consistent with observations of the intra-ligand bond lengths. This similar effect is observed in **15** which has no sulfur coordination and the imine bond length is suggestive of an unactivated imine.

Comparison of Redox Trends:

While **13-15** do not indicate much electronic activation of the ligand they are consistent in terms of the reduction feature in the CV (**Table 4.06**). Usually, redox-active ligands have similar redox-features because the reduction potentials do not change between different metal centers.[23,24] However these complexes do have distinct redox features to **12**. These redox features are all shifted to higher potential compared to **12** suggesting that the latter is the hardest to reduce in this family of α-(imino)imidazoles. This fits in with the pattern of ligand activation as if there is less electron density being pushed into the ligand backbone it will be easier to add an electron within this redox reservoir. Thus, the increase in the ligand redox potential suggests that there is less backbonding (or push effect) from the thiolate in **13**, **14** and **15** which parallels the structural parameters that were observed in the X-ray crystal structures.

Table 4.06: Comparison of ligand redox potentials for **12-15**.

Complex	E_{pc} (V vs. Fc/Fc^{+})
12	-1.89
13	-1.59
14	-1.68
15	-1.58

Conclusions:

Four analogues of **12** have been structurally characterized. Unlike **10-12**, **13-15** display little to no ligand activation. This is due to both the mode of thiolate coordination as in **13** or the lack of thiolate coordination as observed for **14** and **15**. In addition, **13** and **15** have a high-spin electronic structure at the metal ion suggesting that activation could result in strong backbonding from a metal center only if it contains filled t_{2g}-like orbitals. The lack of structural activation of the imine is consistent with the much more positive reduction potentials seen in the CVs of **13-15** compared to **12** (**Table 4.06**), which could be promising for attempting to reduce these complexes.

Notes to Chapter 4

1. Leipzig, B. K.; Rees, J. A.; Nyrov, A.; Theisen, R.; Flowers, S. E.; Kaminsky, W.; DeBeer, S.; Kovacs, J. A. *Prep.*

2. Butschke, B.; Fillman, K. L.; Bendikov, T.; Shimon, L. J. W.; Diskin-Posner, Y.; Leitus, G.; Gorelsky, S. I.; Neidig, M. L.; Milstein, D. *Inorg. Chem.* **2015**, *54*, 4909–4926.

3. Lu, C. C.; Weyhermüller, T.; Bill, E.; Wieghardt, K. *Inorg. Chem.* **2009**, *48*, 6055–6064.

4. Kovacs, J. A.; Brines, L. M. *Acc. Chem. Res.* **2007**, *40*, 501–509.

5. Kitagawa, T.; Dey, A.; Lugo-Mas, P.; Benedict, J. B.; Kaminsky, W.; Solomon, E. I.; Kovacs, J. A. *J. Am. Chem. Soc.* **2006**, *128*, 14448-14449.

6. Yoshioka, S.; Takahashi, S.; Ishimori, K.; Morishima, I. *J. Inorg. Biochem.* **2000**, *81*, 141–151.

7. Ogliaro, F.; de Visser, S. P.; Shaik, S. *J. Inorg. Biochem.* **2002**, *91*, 554–567.

8. Bruker (**2007**) APEX(Verson 2.1-4) SAINT (version 7.34A), SADABS (version 2007/4), BrukerAXS Inc, Madison, Wisconsin, USA.

9. Altomare, A. Burla, C. Camalli, M., Cascarano, G. L., Giacovazzo, C. Guagliardi, A., Moliterni, A. G. G., Polidori, G., Spagna, R. *J. Appl. Crystallogr.* **1999**, *32*, 115–119.

10. Altomare, A.; Cascarano, G. L.; Giacovazzo, C.; Guagliardi, A. *J. Appl. Crystallogr.* **1993**, *26*, 343–350.

11. Sheldrick, G. M. SHELXL-97: Program for the Refinement of Crystal Structures, University of Göttingen, Germany, 1997.

12. Mackay, S.; Edwards, C.; Henderson, A.; Gilmore, C.; Stewart, N.; Shankland, K.; Donald, A. University of Glasgow, Scotland 1997.

13. Waasmaier, D.; Kirfel, A. *Acta Crystallogr. A.* **1995**, *51*, 416–430.

14. Shearer, J.; Kung, I. Y.; Lovell, S.; Kovacs, J. A. *Inorg. Chem.* **2000**, *39*, 4998–4999.

15. Kung, I.; Schweitzer, D.; Shearer, J.; Taylor W. D.; Jackson, H. L.; Lovell, S.; Kovacs, J. A. *J. Am. Chem. Soc.* **2000**, *122*, 8299–8300.

16. Wu, J. Y.; Moreau, B.; Ritter, T. *J. Am. Chem. Soc.* **2009**, *131*, 12915–12917.

17. Shaik, S.; Kumar, D.; de Visser, S. P.; Altun, A.; Thiel, W. *Chem. Rev.* **2005**, *105*, 2279-2328.

18. Dey, A.; Jiang, Y.; Ortiz de Montellano, P.; Hodgson, K. O.; Hedman, B.; Solomon, E. I. *J. Am. Chem. Soc.* **2009**, *131*, 7869–7878.

19. McQuilken, A. C.; Jiang, Y.; Siegler, M. A.; Goldberg, D. P. *J. Am. Chem. Soc.* **2012**, *134*, 8758–8761.

20. Coggins, M. K.; Sun, X.; Kwak, Y.; Solomon, E. I.; Rybak-Akimova, E.; Kovacs, J. A. *J. Am. Chem. Soc.* **2013**, *135*, 5631–5640.

21. Coggins, M. K.; Toledo, S.; Shaffer, E.; Kaminsky, W.; Shearer, J.; Kovacs, J. A. *Inorg. Chem.* **2012**, *51*, 6633–6644.

22. Brines, L. M.; Shearer, J.; Fender, J. K.; Schweitzer, D.; Shoner, S. C.; Barnhart, D.; Kaminsky, W.; Lovell, S.; Kovacs, J. A. *Inorg. Chem.* **2007**, *46*, 9267-9277.

23. Lu, C. C.; Bill, E.; Weyhermüller, T.; Bothe, E.; Wieghardt, K. *J. Am. Chem. Soc.* **2008**, *130*, 3181-3197.

24. King, E. R.; Betley, T. A. *J. Am. Chem. Soc.* **2009**, *131*, 14374–14380.

Chapter 5:

Thiazolidine-Ligated Ferrous Metal Complexes.

Introduction:

While the α-(imino)pyridine complexes have found some use in catalytic chemistry,[1] the more common redox-active bis(imino)pyridine ligand backbone has been extensively used in base metal catalysis due to its much more rigid pincer framework. They have been shown to catalyze polymerization,[2,3] hydrogenation,[4,5] and cyclization[6,7] transformations due to the ligand's ability to both accept and donate electron density to and from the metal active site. This pincer ligand also provides a rigid tridentate backbone that can mimic the tri-histidine coordination of a variety of metalloenzymes.[8]

Scheme 5.01: Oxygenation of a coordinated aromatic thiolate at a ferrous metal center using a redox active bis(imino)pyridine ligand backbone reported by Goldberg.

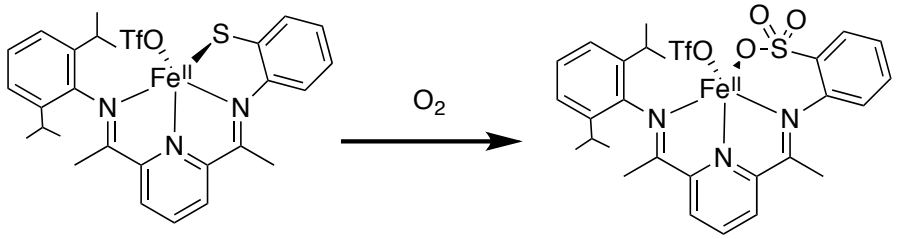

Goldberg has shown that an asymmetric bis(imino)pyridine Fe complex is a competent cysteine dioxygenase mimic (**Scheme 5.01**).[9] They were able to tether on an aromatic thiolate that was coordinated to the bis(imino)pyridine framework to form a tetradentate ligand that, when exposed to O_2, would oxygenate the coordinated thiolate. In a different study, it was observed that, if the thiolate was not tethered to the ligand backbone, different reactivity would be seen depending on the strength of the coordinated counterion.[10] While both the enzyme active species and Goldberg's mimic both contain a coordinated thiolate, there can be subtle differences between an aromatic thiolate and an aliphatic thiolate.[11]

While Goldberg was able to coordinate the aromatic thiolate to an Fe metal center, attempts to coordinate the aliphatic thiolate were unsuccessful. Similar to **15**, there was unusual reactivity in the metal template condensation step. A carbon-sulfur bond similar to **15** was observed in the solid state structure, however the smaller 5 membered ring is structurally similar to the thiazolidine ring structure produced in the enzyme isopennicilin *N*-synthase.[12]

Experimental:

General Considerations: DMSO-d_6 and $CDCl_3$ were purchased from Cambridge Isotope Labs and used as received. Ethanol was purchased from Decon and degassed prior to use. Et_2O was purchased from Fischer Scientific and purified using a solvent purification columns housed in a custom stainless steel cabinet and dispensed by a stainless steel Schlenk-line (GlassContour). All other solvents were purchased from Sigma Aldrich. MeOH, MeCN and CH_2Cl_2 were dried and distilled prior to use.

^{1}H NMR spectra were obtained on a Bruker AV300, AV301, DRX499, or AV500. Chemical shifts are listed in parts per million and were reported relative the residual protio solvent. UV/Vis spectra were recorded on a Varian Cary 50 spectrophotometer equipped with a fiber optic cable connected to a "dip" ATR probe (C-technologies). A custom-built two neck solution sample holder equipped with a threaded glass connector was sized specifically to fit the "dip" probe. Matrix-Assisted Laser Desorption/Ionization (MALDI) mass spectrometry (ESI-MS) was preformed on a Bruker Autoflex II and used pyrene as a charge transfer matrix. All manipulations were performed using Schlenk

techniques or under a N_2 atmosphere in a glovebox. The asymmetric ketone was synthesized according to literature procedure.[11]

Synthesis of [$Fe^{II}N_3$thiazolidineCl]Cl (16): The asymmetric ketone (0.05 g, 0.16 mmol) and $FeCl_2$ (0.020 g, 0.16 mmol) were stirred in THF (2 mL. To this solution 2-propanethiol,1-amino-2-methyl hydrochloride salt (0.022 g, 0.16 mmol) and triethylamine (0.031 g, 0.31 mmol) were added. This solution was stirred for 14 hours and monitored by mass spectroscopy. A peak at 464m/z indicated the formation of the product. The solution was then evacuated *in vacuo* and redissolved in MeCN (4 mL). Salts were filtered and the solution was evacuated to a minimal volume and layered with Et_2O. A blue solid, **16**, was collected in 47% yield (0.04 g, 0.087 mmol). X-ray quality crystals were grown through slow vapor diffusion of Et_2O into an MeCN solution. λ_{max} (nm) (ε ($M^{-1}cm^{-1}$): (MeCN): 599 (500), (MeOH): 638 (545), (DCM): 620 (480), THF: 681 (419). MALDI-MS: expected *m/z* for $[C_{25}H_{35}N_3SFeCl]^+$= 499.5, found *m/z*=464.1 (no chloride coordinated).

Synthesis of [($Fe^{II}N_3$thiazolidineCl)$_2$Cl]OTf (17): 17 was synthesized in the same manner as **16** but $Fe(OTf)_2$ was used instead of $FeCl_2$. λ_{max} (nm) (ε ($M^{-1}cm^{-1}$): (THF): 625 (453). MALDI-MS *m/z* for $[C_{25}H_{35}N_3SFeCl]^+$= 499.5, found *m/z*=464.1. The MS shows a similar pattern to the monomer suggesting that the dimer cleaves under MS conditions.

X-Ray Crystallographic Structure Determination

A blue twinned twinned crystal, **16**, measuring 0.15 x 0.05 x 0.05 mm^3 was mounted on a loop with oil. Data was collected at -173°C on a Bruker APEX II single crystal X-ray diffractometer, Mo-radiation. Crystal-to-detector distance was 40 mm and exposure time was 90 seconds per degree for all sets. The scan width was 0.5°. Data collection was 97.2% complete to 25° in ϑ. The sample seemed to consist of at least three individuals. The raw data appeared conglomerated. With CELL_NOW[13] three individual data sets were isolated which, if not separated, would cause considerable overlap of diffraction peak intensities. Multi-domain integration with SAINT within the APEX2 software package by Bruker and absorption correction with twinabs[14] removed the overlap. A total of 5887 independent reflections were collected covering the indices, h = -11 to 9, k = -16 to 15, l = -9 to 16 with R_{int} = 0.1268 indicated that the twin-refined data was of less than average quality (0.07). Indexing and unit cell refinement indicated then a triclinic P lattice. The space group was found to be P $\bar{1}$ (No.2).

A red prism, **17**, measuring 0.22 x 0.07 x 0.05 mm^3 was mounted on a loop with oil. Data was collected at -173°C on a Bruker APEX II single crystal X-ray diffractometer, Mo-radiation. Crystal-to-detector distance was 40 mm and exposure time was 10 seconds per frame for all sets. The scan width was 0.5°. Data collection was 99.6% complete to 25° in ϑ. A total of 225743 reflections were collected covering the indices, h = -15 to 15, k = -27 to 28, l = -38 to 37. 17222 reflections were symmetry independent and the R_{int} = 0.0904 indicated that the data was of slightly less than average quality (0.07). Indexing and unit cell refinement indicated a primitive monoclinic lattice. The space group was found to be P $2_1/c$ (No.14).

Solution by direct methods (SHELXS, SIR97[15,16]) produced a complete heavy atom phasing model consistent with the proposed structure. The structure was completed

by difference Fourier synthesis with SHELXL97.[17, 18] Scattering factors are from Waasmair and Kirfel.[19] Hydrogen atoms were placed in geometrically idealised positions and constrained to ride on their parent atoms with C---H distances in the range 0.95-1.00 Angstrom. Isotropic thermal parameters U_{eq} were fixed such that they were $1.2U_{eq}$ of their parent atom Ueq for CH's and $1.5U_{eq}$ of their parent atom U_{eq} in case of methyl groups. All non-hydrogen atoms were refined anisotropically by full-matrix least-squares. Crystal Data is presented in **Table 5.01**.

Table 5.01: Crystallographic data for **16** and **17**.

	16	**17**
Formula	$C_{25}H_{35}Cl_2FeN_3S$	$C_{111}H_{162}Cl_{14}Fe_4N_{12}O_8S_6$
MW (g/mol)	621.30	2818.59
Crystal System	Triclinic	Monoclinic
Space Group	P-1	P 1 21/c 1
Unit Cell Dimensions		
a (Å)	9.3775(18)	11.6846(13)
b (Å)	12.758(3)	21.003(2)
c (Å)	12.987(4)	28.470(3)
α (deg)	82.409(12)	90
β (deg)	83.916(7)	97.247(6)
γ (deg)	73.056(8)	90
Final R indices	0.0727	0.0738
R indices (all Data)	0.1731	0.1174

Results and Discussion:

Thiazoldine Ligated Iron Complexes:

The unsymmetrical ketone was prepared following an adapted literature procedure by performing an acid catalyzed mono condensation to 2,6-diacetylpyridine (**Scheme 5.02**).[20] The imine substituent was 2,6-diisopropylphenyl, which imparts significant steric

bulk around the metal center. Although the yield was low (34%) the low cost of the starting materials led to the facile and inexpensive preparation of large quantities of this precursor.

Scheme 5.02: Synthesis of asymmetric ketone (top), and metal template Schiff base condensation (bottom).

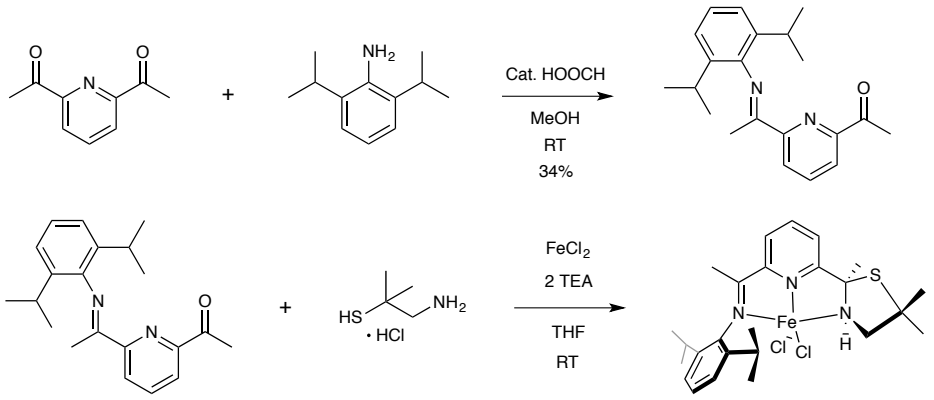

Treating 2-propanethiol,1-amino-2-methyl hydrochloride salt with this precursor in the presence of an Fe(II) source produced a deep blue mixture suggesting that there was coordination to the metal in the templated Schiff base condensation. MALDI-mass spectroscopy provided evidence that the condensed ligand was coordinated to the ferrous metal ion (**Figure 5.01**). The peak is consistent with the entire ligand coordinated to the metal ion and the isotopic pattern matches with what would be expected for a monomeric Fe metal complex due to the M-2 peak at 462.1 *m/z*.

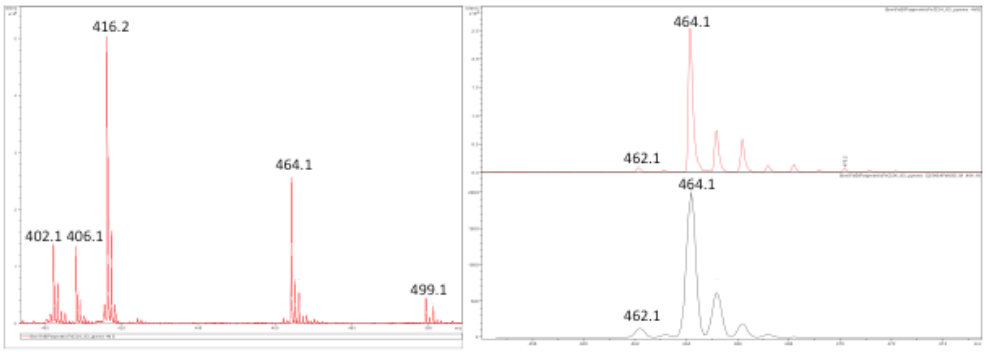

Figure 5.01: MALDI-MS of **16** (left) indicating the peak associated with the coordinated complex at 464.1 *m/z*. Comparison of the isotopic pattern of the peak at 464.1 and the theoretical *m/z* of **16** (right).

Using ferrous chloride as the initial Fe source afforded the crystals of the template product, **16** (**Figure 5.02**). X-ray diffractometry identified this as a monomeric ferrous complex. This five coordinate complex has the three nitrogens of the ligand backbone coordinated to the metal and two chlorides creating a distorted square pyramidal geometry with a τ-value of 0.092 (**Table 5.02**). Unlike many other complexes from our group that form strong covalent Fe-S bonds, this complex does not have a thiolate coordinated to the metal center. Instead, a new carbon-thiolate single bond is formed making a five-membered thiozolidine ring.

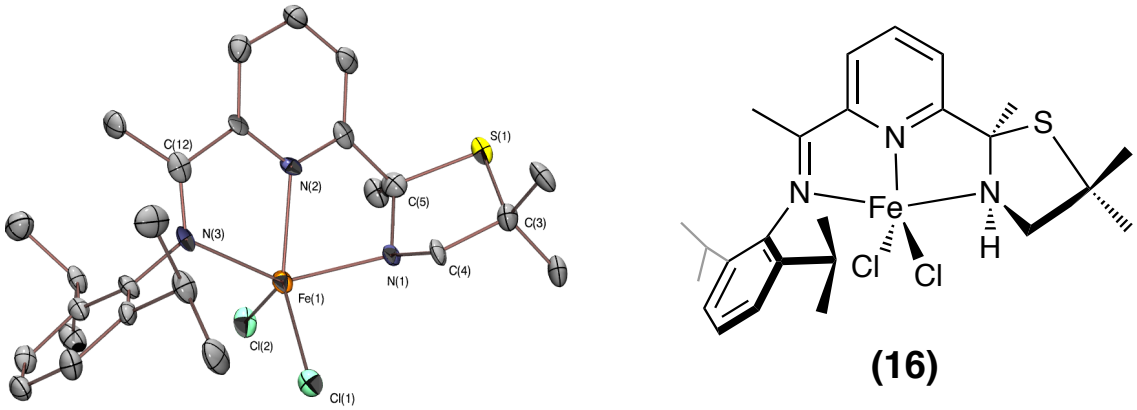

Figure 5.02: ORTEP of **16** showing 50% probability ellipsoids (Left). Hydrogen atoms and solvents of crystallization were removed for clarity. Corresponding structural representation of **16** (Right).

It seems that, during the Schiff base condensation, instead of the thiolate coordinating to the metal it participates in the condensation reaction by nucleophillically attacking the partially positive carbon atom. A plausible mechanism for this reactivity would be that the Fe serves as a Lewis acid to activate the carbonyl for nucleophilic attack of the primary amine. Instead of the imine formation to release water, the thiolate will participate in an intramolecular nucleophillic attack at the carbon releasing the water (path A, **Scheme 5.03**). Alternatively the thiolate could attack first followed by the primary amine to release the water (path B, **Scheme 5.03**).

Scheme 5.03: Possible thiazolidine ring cyclization at the Fe center. Path A (top) has initial nucleophilic attack by the primary imine while Path B (bottom) has the initial nucleophillic attack by the thiolate.

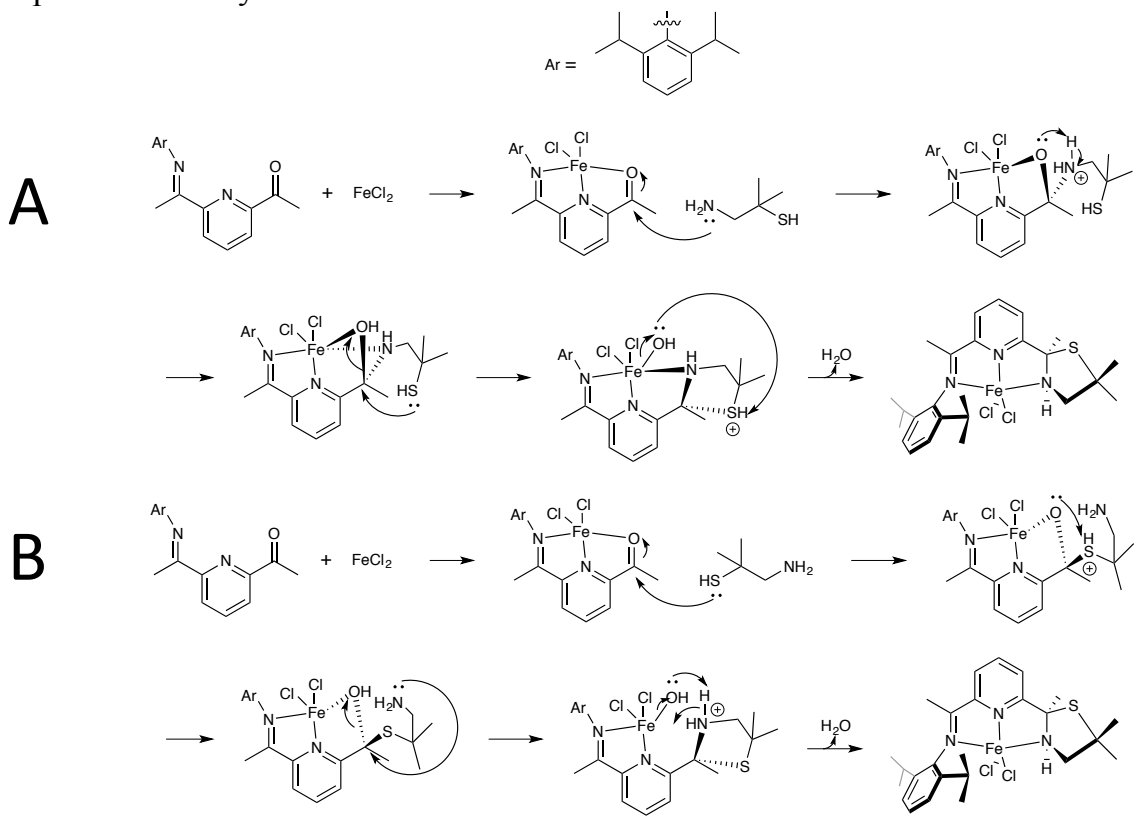

The formation of a thermodynamically stable 5-membered ring may the driving force for this type of reactivity. Typically our group uses 3-methyl,3-mercapto-2-butanone to add the thiolate during the Schiff base condensation. In using this reagent, it is unlikely to observe the same nucleophilic attack of the thiolate instead of the imine due to its location in relation to the carbonyl group. Since the carbonyl carbon in this substrate is only 2 bonds away from the thiolate the product of a nucleophillic attack would be a highly strained 3 membered ring containing a thioether which would favor thiolate coordination to the ferrous ion.[21]

The Fe-N bond lengths of this complex are all above 2.1 Å and are consistent with a high spin ferrous complex (**Table 5.02**). The thioether has equivalent S-C bond lengths (1.859(6) Å and 1.848(5) Å) suggesting that a strongly covalent carbon-sulfur bond has been formed. The two chlorides have equivalent bond lengths (2.3035(16) and 2.3008(17)) and no counter ions are observed further supporting the assignment of a ferrous oxidation state. The strongly coordinating chlorides from the starting $FeCl_2$ could inhibit coordination of the thiolate and favor thiazolidine formation.

Due to the thiazolidine ring formation, this complex would be more similar to an α-(imino)pyridine instead of the targeted bis(imino)pyridine. Unlike the α-(imino)-*N*-heterocycles described in chapters 2-4, this complex shows no activation of the imine bond, with a C-N 1.283(6) Å (**Table 5.03**). This lack of activation would be expected with no strong donation from a coordinated thiolate or the strong backbonding from a low-spin ferrous metal center.

Table 5.02: Selected geometrical parameters for **16** and **17**. *indicates the bridging chloride.

16	Distance (Å)	17 Fe(1)	Distance (Å)	17 Fe(2)	Distance (Å)
Fe-N(1)	2.274(4)	**Fe(1)-N(1)**	2.237(4)	**Fe(2)-N(4)**	2.233(4)
Fe-N(2)	2.120(4)	**Fe(1)-N(2)**	2.088(4)	**Fe(2)-N(5)**	2.096(4)
Fe-N(3)	2.233(4)	**Fe(1)-N(3)**	2.199(4)	**Fe(2)-N(6)**	2.234(4)
Fe-Cl(1)	2.3035(16)	**Fe(1)-Cl(1)***	2.4066(13)	**Fe(2)-Cl(1)***	2.3617(16)
Fe-Cl(2)	2.3008(17)	**Fe(1)-Cl(2)**	2.2859(13)	**Fe(2)-Cl(3)**	2.2767(17)
S-C(3)	1.848(5)	**S(1)-C(3)**	1.835(5)	**S(2)-C(28)**	1.838(5)
S-C(5)	1.859(6)	**S(1)-C(5)**	1.861(5)	**S(2)-C(5)**	1.840(5)

16	Bond angle (deg)	17 Fe(1)	Bond angle (deg)	17 Fe(2)	Bond angle (deg)
N(1)-Fe-N(3)	144.70(15)	**N(2)-Fe(1)-Cl(2)**	150.59(11)	**N(4)-Fe(2)-N(6)**	145.95(15)
N(2)-Fe-Cl(1)	139.20(13)	**N(3)-Fe(1)-N(1)**	148.86(14)	**N(5)-Fe(2)Cl(1)**	133.88(11)
N(2)-Fe-Cl(2)	111.02(12)	**Cl(2)-Fe(1)-Cl(1)**	105.96(5)	**N(5)-Fe(2)-Cl(3)**	118.45(11)
τ=	0.092	**τ=**	**0.**0144	**τ=**	0.100

Table 5.03: Selected intra-ligand bond lengths for **16** and **17**.

Monomeric Complex	Distance (Å)	Dimeric Complex Fe(1)	Distance (Å)	Dimeric Complex Fe(2)	Distance (Å)
N(3)-C(12)	1.283(6)	**N(3)-C(12)**	1.286(6)	N(4)-C(37)	1.283(6)
C(11)-C(12)	1.474(7)	**C(11)-C(12)**	1.495(6)	C(36)-C(37)	1.484(7)
C(11)-N(2)	1.354(6)	**C(11)-N(2)**	1.348(6)	C(36)-N(5)	1.355(6)
N(1)-C(5)	1.473(6)	**N(1)-C(5)**	1.470(6)	N(6)-C(30)	1.480(6)
C(5)-C(7)	1.504(7)	**C(5)-C(7)**	1.521(6)	C(30)-C(32)	1.530(7)
C(7)-N(2)	1.333(6)	**C(7)-N(2)**	1.336(6)	C(32)-N(5)	1.322(6)

In an attempt to prevent the thiazolidine ring formation, and to isolate a monomeric thiolate ligated ferrous complex, $Fe(OTf)_2$ was used as the Fe source instead of $FeCl_2$. The loss of the two chlorides could provide easier coordination for the thiolate. However, the same cyclization and carbon-sulfur bond formation occurred (**Figure 5.03**) but this time yielded a bimetallic structure, **17**. Both Fe metal centers are coordinated by three nitrogens and two chlorides, one of which bridges the two centers. As with **16** both of the Fe's in **17** are contained in a distorted square pyramidal geometry, as evidenced by a τ-value of 0.014 for Fe(1) and 0.10 for Fe(2). While both irons are in a similar geometry, the orientation is slightly different between the two. The bridging chloride, Cl(1), is in the axial position around Fe(1) while but in the basal plane around Fe(2) with Cl(3) occupying in the axial position. The chlorides could originate from the starting 2-propanethiol,1-amino-2-methyl hydrochloride salt. The sterics of this bi-metalic structure may cause a slight disruption of the geometry of these two Fe metal

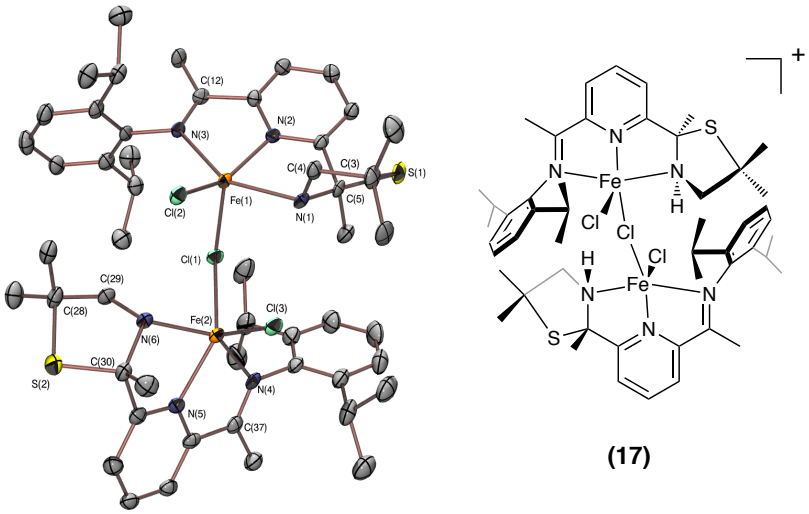

Figure 5.03: ORTEP of **17** showing 50% probability ellipsoid. All hydrogen atoms and counterions omitted for clarity. Corresponding structural representation of **17** (right).

centers. If the bridging chloride were to be in the axial position for both centers there may be a steric clash between the isopropyl groups of the phenyl ring or the bulky gem-*di*-methyl groups adjacent to the sulfur in the thiozolidine ring structure.

Similar to **16** the bond lengths in the solid state suggests that both Fe have a high spin state (**Table 5.02**). The bridging chloride has a much longer Fe-Cl bond lengths (2.4066(13) Å and 2.3617(13) Å) than the non-bridging chlorides (2.2859(13) Å and 2.2767(13) Å), which is to be expected. A single crystalized OTf counteranion along with the three coordinated chlorides suggest a ferrous oxidation state for both metal centers and is consistent with the bond lengths observed. The C-S bond lengths are consistent suggesting the formation of a carbon-sulfur sigma bond. It seems that the weaker coordinated bridging chloride does not effect the spin state or the ability of the Fe to backbond with the α-(imino)pyridine. The imine bond lengths of 1.286(6) and 1.283(6) Å are consistent with an unactivated ligand (**Table 5.03**).

The formation of a 5-membered thiazolidine ring was not predicted but similar to the ring formation in isopenicillin *N*-synthase.[22] One difference is Isopennicilin *N*-synthase forms a thiozolidine ring structure through reactivity with O_2.[12] High-valent Fe dioxygen species are responsible for activating C-H bonds and forming a C-S bond.[23,24] The C-S bond formed in these complexes seems to be formed through much different chemistry but the final product still has some structural similarities to this important substrate.

Thiozolidine ring structures are observed in other areas of bioinorganic chemistry such as those seen in the reactivity of siderophores.[25] Bacteria use siderophores to scavenge important metals from outside the cell.[26] These metals are then integrated into

important metalloenzymes that will help with DNA synthesis and electron transfer, among other important applications. The virulence of two bacteria *Yersinia pestis,* which causes the bubonic plague, and *Yersinia eterocolitica,* a food borne pathogen, both depend on the amount of Fe available in the environment. These bacteria, among others, scavange Fe ions through the siderophore yersiniabactin (**Figure 5.04**), which contains thiazoldine rings to bind Fe in the environment.[27] The upregulation in siderophores and the scavenging of metals will precede an increase in virulence factors of bacteria. Understanding how thiozolidines bind to transition metals would aid in understanding how to disrupt and minimize the effects of these toxic bacteria.

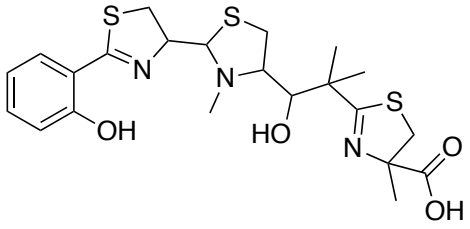

Figure 5.04: Structure of yersiniabactin indicating multiple thiazolidines within the substrate.

*Electronic Absorption Spectroscopy of **16** and **17***:

Similar to the ferrous α-(imino)-*N*-heterocycles described in chapters 2 and 3, these two complexes, **16** and **17**, contain charge transfer bands in the visible region. **16** has a charge transfer in MeOH at 638 nm. This charge transfer is much less intense than that observed for compounds **10-12** and has a molar absorptivity of 545 $M^{-1}cm^{-1}$ (**Figure 5.05**). The lower intensity is in line with molar absorptivities for other non thiolate ligated ferrous α-(imino)pyridines.[28,29]

This charge transfer is most likely a Fe to α-(imino)pyridine π^* transition as this ligand still has redox-active low lying empty orbitals. The decrease in molar absorptivity

compared to complexes **10-12** is most likely due to the fact that there is no mixing of the sulfur in this transition. **16** does have a solvent dependence on the charge transfer as in the λ_{max} is red shifted in THF to 681 nm while in CH_2Cl_2 and MeCN it is blue shifted to 620 nm and 559 nm respectively. The molar absorptivities are all relatively similar ranging between 419 $M^{-1}cm^{-1}$ to 545 $M^{-1}cm^{-1}$.

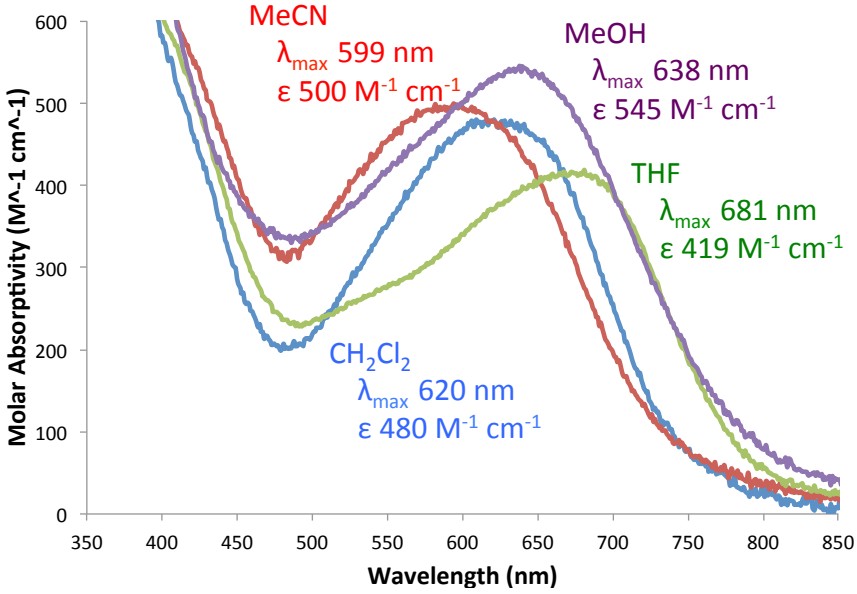

Figure 5.05: Electronic absorption spectrum of **16** in various organic solvents at RT.

The geometry and electronics of this complex could play a role in its solvent-dependent electronic absorption spectra. Since this complex is 5-coordinate and high spin there is a chance that in solution a solvent molecule could coordinate and slightly alter the electronic structure. The change of the *d*-orbital manifold would then impact the energy of the MLCT transition. One observation is that the highest energy charge transfer is observed in MeCN, which could behave more as an L-type or even a π-accepting ligand. This would then lower the metal *d*-orbitals that could backbond, have a transition to the ligand π^* orbital, and also raise the energy of this charge transfer transition. Conversely, if MeOH or THF coordinated they may behave more as a π-donating ligand and raise the

metal *d*-orbitals and lower the MLCT transition, as observed in the UV-Vis spectrum (**Figure 5.05**).

The λ_{max} of **17** (625 nm) is actually blue-shifted in THF compared to the monomeric structure. This could be due to the much weaker interaction of the bridging chloride compared to a singly coordinated chloride. The X-type π-donating chloride would have a much stronger interaction on the Fe *d*-orbitals when it is not bridging, raising the *d*-orbitals and lowering the energy of the MLCT transition observed for the monomeric chloride. If the metal template Schiff base condensation is heated, then the λ_{max} of the product in THF will shift to 689 nm, similar to the monomeric species. This would be consistent with the thermal splitting of the dimeric structure.

O_2 Reactivity:

There are examples of monomeric non-heme Fe(II) enzymes that react with O_2.[30,31] Although this complex is not a model for non-heme cysteinate ligated metalloenzyme, these coordinatively unsaturated complexes could still react with O_2. The reactivity with small molecule substrates can have significant differences in protic and aprotic solvents. In protic solvents such as MeOH and EtOH, all that is observed when **16** and **17** are treated with O_2 is the decay of the charge transfer transition. In contrast, there seems to be an intermediate observed when these reactions are performed in THF or CH_2Cl_2.

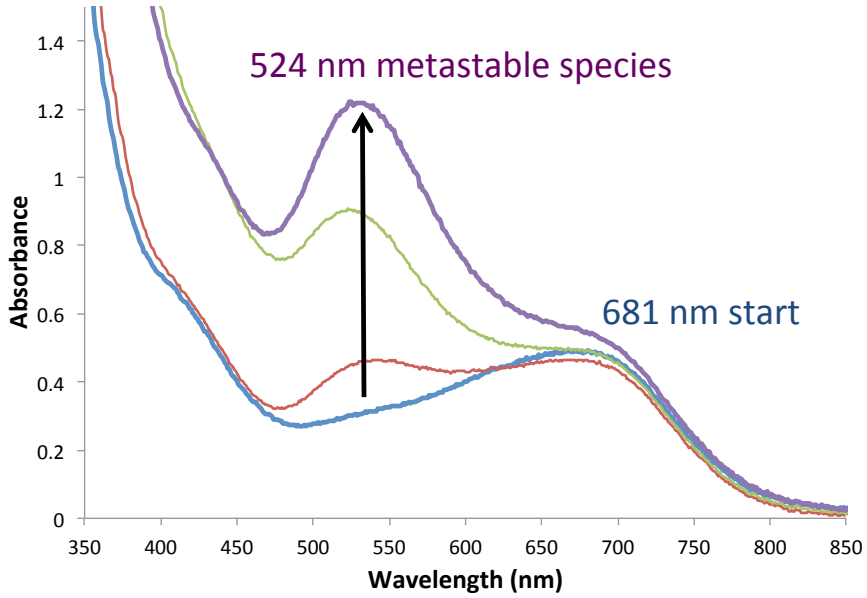

Figure 5.06: Reactivity of **16** with O_2. A metastable stable species is observed at 524 nm.

16 has a new charge transfer band when ambient pressure O_2 is added in THF. This peak has an intense λ_{max} at 524 nm (**Figure 5.06**). While this new peak grows in rapidly at room temperature, it maintains a shoulder at 681 nm suggesting that the starting complex may be still present. This intermediate will decay quickly resulting in a final spectrum very similar to the starting complex. The λ_{max} of the final spectrum is blue shifted by only 20 nm to 660 nm (**Figure 5.07**). Since the feature at 680 nm does not change with the addition of O_2 throughout the reaction it may mean an unidentified complex is responsible for reacting with O_2 and generating a metastable species at 524 nm.

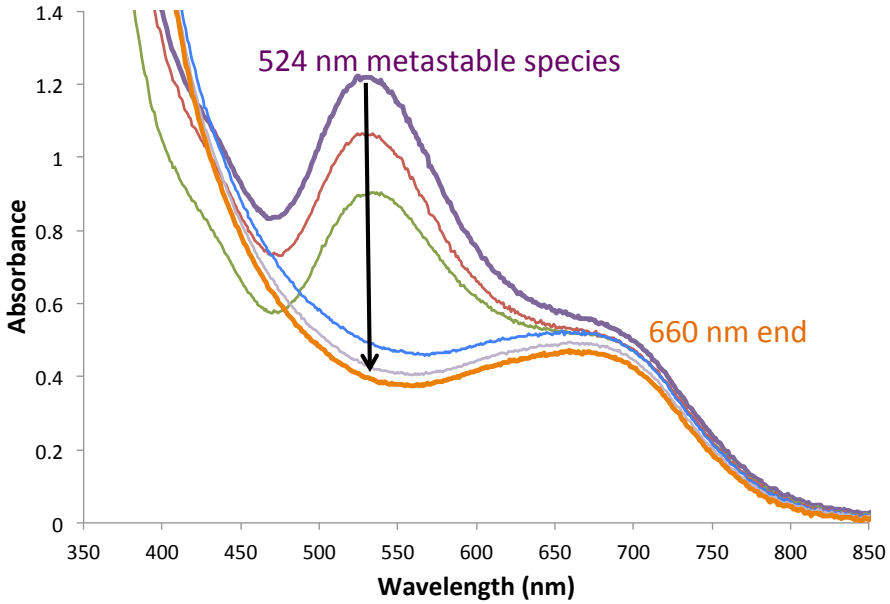

Figure 5.07: Decay of the metastable species at 524 nm.

While this metastable species is unstable at room temperature, it is much longer lived at low temperatures. At -40° C the peak at 524 nm is stable for hours suggesting a potential way for isolating this species. At low temperatures it is much easier to resolve the feature of the starting band at 680 nm while the intermediate is present suggesting that the species responsible for this band may not react with O_2. Similar to the room temperature reactivity, the peak at 524 nm will decay and the resulting spectrum will look similar to the starting spectrum with a peak at 660 nm.

17 will also react with O_2. Similar to **16** a band grows in around 520 nm however, it is not as defined (**Figure 5.08**). This new absorption band persists and does not convert back to a spectra similar to the starting material, as observed for **16**. Overall, O_2 will react with a product from both of these reactions however, the fact that the end and starting spectra are so similar suggests that the complex responsible for the main band at 680 nm may not react with O_2.

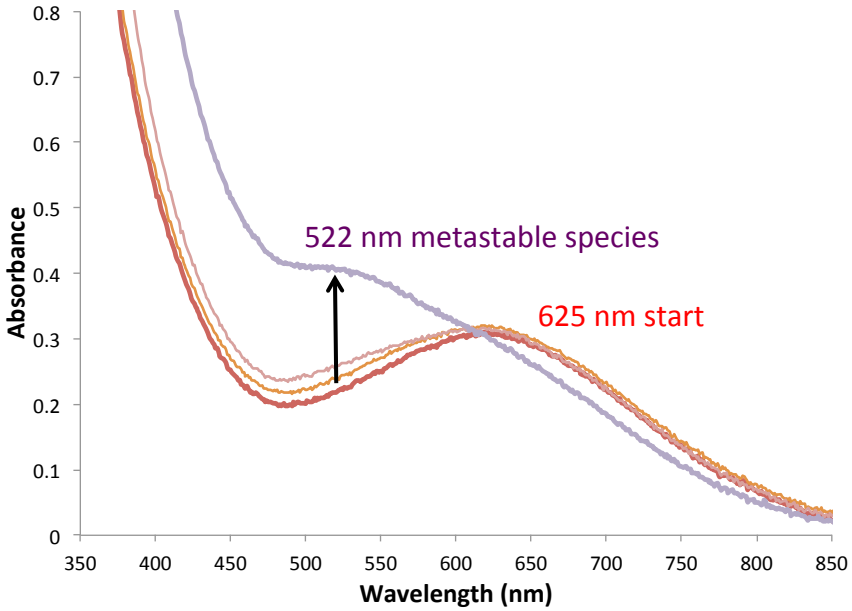

Figure 5.08: Reactivity of **17** with O_2 at RT.

Conclusions:

Two ferrous complexes have been structurally synthesized, each containing a five membered thiozolidine ring. This ring was formed during the Schiff base condensation and prevented the desired thiolate coordination to the ferrous metal center. These thiozolidine rings are similar to those observed in isopennicilin *N*-synthase and in certain siderophores. Although these complexes do not have a thiolate coordinated to the metal atom, some species seems to react with O_2 due to the observance of a metastable species. With the lack of a coordinated thiolate and the change in spin state, the imine bond in **16** and **17** seems to be much less activated than those observed in **10-12**.

Notes to Chapter 5

1. Wu, J. Y.; Moreau, B.; Ritter, T. *J. Am. Chem. Soc.* **2009**, *131*, 12915–12917.

2. Bouwkamp M. W.; Lobkovsky, E.; Chirik, P. J. *J. Am. Chem. Soc.* **2005**, *127*, 9660–9661.

3. Schaefer, B. A.; Margulieux, G. W.; Tiedemann, M. A.; Small, B. L.; Chirik, P. J. *Organometallics* **2015**, *34*, 5615–5623.

4. Chirik, P. J. *Acc. Chem. Res.* **2015**, *48*, 1687–1695.

5. Monfette, S.; Turner, Z. R.; Semproni, S. P.; Chirik, P. J. *J. Am. Chem. Soc.* **2012**, *134*, 4561–4564.

6. Bouwkamp; M. W.; Bowman A. C.; Lobkovsky, E.; Chirik, P. J. *J. Am. Chem. Soc.* **2006**, *128*, 13340-13341.

7. Hoyt, J. M.; Sylvester, K. T.; Semproni, S. P.; Chirik, P. J. *J. Am. Chem. Soc.* **2013**, *135*, 4862–4877.

8. Holm, R. H.; Kennepohl, P.; Solomon, E. I. *Chem. Rev.* **1996**, *96*, 2239-2314.

9. Jiang, Y.; Widger, L. R.; Kasper, G. D.; Siegler, M. A.; Goldberg, D. P. *J. Am. Chem. Soc.* **2010**, *132*, 12214–12215.

10. Badiei, Y. M.; Siegler, M. A.; Goldberg, D. P. *J. Am. Chem. Soc.* **2011**, *133*, 1274–1277.

11. Kumar, D.; Sastry, G. N.; Goldberg, D. P.; de Visser, S. P. *J. Phys. Chem. A* **2012**, *116*, 582–591.

12. Lundberg, M.; Siegbahn, P. E. M.; Morokuma, K. *Biochemistry* **2007**, *47*, 1031–1042.

13. Sheldrick, G. M. CELL_NOW, University of Göttingen, Germany, 2005.

14. Sheldrick, G. M. TWINABS, University of Göttingen, Germany, 1997.

15. Altomare, A.; Cascarano, G. L.; Giacovazzo, C.; Guagliardi, A. *J. Appl. Crystallogr.* **1993**, *26*, 343–350.

16. Altomare, A. Burla, C. Camalli, M., Cascarano, G. L., Giacovazzo, C. Guagliardi, A., Moliterni, A. G. G., Polidori, G., Spagna, R. *J. Appl. Crystallogr.* **1999**, *32*, 115–119.

17. Sheldrick, G. M. SHELXL-97: Program for the Refinement of Crystal Structures, University of Göttingen, Germany, 1997.

18. Mackay, S.; Edwards, C.; Henderson, A.; Gilmore, C.; Stewart, N.; Shankland, K.; Donald, A. University of Glasgow, Scotland 1997.

19. Waasmaier, D.; Kirfel, A. *Acta Crystallogr. A.* **1995**, *51*, 416–430.

20. Bianchini, C.; Mantovani, G.; Meli, A.; Migliacci, F.; Zanobini, F.; Laschi, F.; Sommazzi, A. *Eur. J. Inorg. Chem.* **2003**, *2003*, 1620–1631.

21. Shearer, J.; Scarrow, R. C.; Kovacs, J. A. *J. Am. Chem. Soc.* **2002**, No. 124, 11709-11717.

22. Baldwin, J. E.; Bradley, M. *Chem. Rev.* **1990**, *90*, 1079–1088.

23. Borovok, I.; Landman, O.; Kreisberg-Zakarin, R.; Aharonowitz, Y.; Cohen, G. *Biochemistry* **1996**, *35*, 1981–1987.

24. Tamanaha, E.; Zhang, B.; Guo, Y.; Chang, W.; Barr, E. W.; Xing, G.; St. Clair, J.; Ye, S.; Neese, F.; Bollinger, J. M.; Krebs, C. *J. Am. Chem. Soc.* **2016**, *138*, 8862–8874.

25. Miethke, M.; Marahiel, M. A. *Microbiol. Mol. Biol. Rev.* **2007**, *71*, 413–451.

26. Sandy, M.; Butler, A. *Chem. Rev.* **2009**, *109*, 4580–4595.

27. Gehring, A. M.; Mori, I.; Perry, R. D.; Walsh, C. T. *Biochemistry* **1998**, *37*, 11637-11650.

28. Vedder, C.; Schaper, F.; Brintzinger, H.-H.; Kettunen, M.; Babik, S.; Fink, G. *Eur. J. Inorg. Chem.* **2005**, *2005*, 1071–1080.

29. Shejwalkar, P.; Rath, N. P.; Bauer, E. B. *Dalton Trans.* **2011**, *40*, 7617-7631.

30. Nam, W. *Acc. Chem. Res.* **2007**, *40*, 465–465.

31. Kovaleva, E. G.; Neibergall, M. B.; Chakrabarty, S.; Lipscomb, J. D. *Acc. Chem. Res.* **2007**, *40*, 475–483.

Bibliography

Ahmad, S.; McCallum, J. D.; Shiemke, A. K.; Appelman, E. H.; Loehr, T. M.; Sanders-Loehr, J., Raman spectroscopic evidence for side-on binding of peroxide ion to (ethylenediaminetetraacetato)ferrate(1-). *Inorg. Chem.* **1988**, 27, 2230–2233.

Altomare, A. Burla, C. Camalli, M., Cascarano, G. L., Giacovazzo, C. Guagliardi, A., Moliterni, A. G. G., Polidori, G., Spagna, R., SIR97: a new tool for crystal structure determination and refinement. *J. Appl. Crystallogr.* **1999**, 32, 115–119.

Altomare, A.; Cascarano, G. L.; Giacovazzo, C.; Guagliardi, A., Completion and refinement of crystal structures with SIR 92. *J. Appl. Crystallogr.* **1993**, 26, 343–350.

Auchère, F.; Rusnak, F., What is the ultimate fate of superoxide anion in vivo? *JBIC J. Biol. Inorg. Chem.* **2002**, 7, 664–667.

Badiei, Y. M.; Siegler, M. A.; Goldberg, D. P., O_2 Activation by Bis(imino)pyridine Iron(II)−Thiolate Complexes. *J. Am. Chem. Soc.* **2011**, 133, 1274–1277.

Bailey, W. D. Late Transition-Metal Complexes Supported by Pincer Ligands: Applications in Partial Oxidation Catalysis. University of Washington, Seattle, 2016

Baldwin, J. E.; Bradley, M., Isopenicillin N synthase: mechanistic studies. *Chem. Rev.* **1990**, 90, 1079–1088.

Bart, S. C.; Chłopek, K.; Bill, E.; Bouwkamp, M. W.; Lobkovsky, E.; Neese, F.; Wieghardt, K.; Chirik, P. J., Electronic Structure of Bis(imino)pyridine Iron Dichloride, Monochloride, and Neutral Ligand Complexes: A Combined Structural, Spectroscopic, and Computational Study. *J. Am. Chem. Soc.* **2006**, 128, 13901–13912.

Bart, S. C.; Lobkovsky, E.; Chirik, P. J., Preparation and Molecular and Electronic Structures of Iron(0) Dinitrogen and Silane Complexes and Their Application to Catalytic Hydrogenation and Hydrosilation. *J. Am. Chem. Soc.* **2004**, 126, 13794–13807.

Becke, A. D., Density-functional exchange-energy approximation with correct asymptotic behavior. *Phys. Rev. A* **1988**, 38, 3098–3100.

Bernal, I.; Jensen, I. M.; Jensen, K. B.; McKenzie, C. J.; Toflund, H.; Tuchagues, J. P., Iron(II) complexes of polydentate aminopyridyl ligands and an exchangeable sixth ligand; reactions with peroxides. Crystal structure of $[FeL_1(H2O)][PF6]_2 \cdot H2O$ [L1=N,N′-bis-(6-methyl-2-pyridylmethyl)-N,N′-bis(2-pyridylmethyl)ethane-1,2-diamine]. *J. Chem. Soc. Dalt. Trans.* **1995**, 3667–3675.

Bianchini, C.; Mantovani, G.; Meli, A.; Migliacci, F.; Zanobini, F.; Laschi, F.; Sommazzi, A., Oligomerisation of Ethylene to Linear α-Olefins by new Cs- and C1-Symmetric [2,6-

Bis(imino)pyridyl]iron and -cobalt Dichloride Complexes. *Eur. J. Inorg. Chem.* **2003**, 1620–1631.

Borovok, I.; Landman, O.; Kreisberg-Zakarin, R.; Aharonowitz, Y.; Cohen, G., Ferrous Active Site of Isopenicillin N Synthase: Genetic and Sequence Analysis of the Endogenous Ligands. *Biochemistry* **1996**, 35, 1981–1987.

Bouwkamp M. W.; Bowman, A. C.; Lobkovsky, E.; Chirik, P. J., Iron-Catalyzed [2π+2π] Cycloaddition of α,ω-Dienes: The Importance of Redox-Active Supporting Ligands. *J. Am. Chem. Soc.* **2006**, 128, 13340–13341.

Bouwkamp, M. W.; Lobkovsky, E.; Chirik, P. J., Bis(imino)pyridine Iron(II) Alkyl Cations for Olefin Polymerization. *J. Am. Chem. Soc.* **2005**, *127*, 9660–9661.

Brines, L. M.; Shearer, J.; Fender, J. K.; Schweitzer, D.; Shoner, S. C.; Barnhart, D.; Kaminsky, W.; Lovell, S.; Kovacs, J. A., Periodic Trends within a Series of Five-Coordinate Thiolate-Ligated $[MII(SMe_2N_4(tren))]^+$ (M = Mn, Fe, Co, Ni, Cu, Zn) Complexes, Including a Rare Example of a Stable CuII−Thiolate. *Inorg. Chem.* **2007**, 46, 9267–9277.

Broering, E. P.; Dillon, S.; Gale, E. M.; Steiner, R. A.; Telser, J.; Brunold, T. C.; Harrop, T. C., Accessing Ni(III)-Thiolate Versus Ni(II)-Thiyl Bonding in a Family of $Ni–N_2S_2$ Synthetic Models of NiSOD. *Inorg. Chem.* **2015**, 54, 3815–3828.

Bruker (**2007**) APEX(Verson 2.1-4) SAINT (version 7.34A), SADABS (version 2007/4), BrukerAXS Inc, Madison, Wisconsin, USA.

Butschke, B.; Fillman, K. L.; Bendikov, T.; Shimon, L. J. W.; Diskin-Posner, Y.; Leitus, G.; Gorelsky, S. I.; Neidig, M. L.; Milstein, D., How Innocent are Potentially Redox Non-Innocent Ligands? Electronic Structure and Metal Oxidation States in Iron-PNN Complexes as a Representative Case Study. *Inorg. Chem.* **2015**, 54, 4909–4926.

Chirik, P. J., Iron- and Cobalt-Catalyzed Alkene Hydrogenation: Catalysis with Both Redox-Active and Strong Field Ligands. *Acc. Chem. Res.* **2015**, 48, 1687–1695.

Chirik, P. J.; Wieghardt, K., Radical Ligands Confer Nobility on Base-Metal Catalysts. *Science* **2010**, 327, 794–795.

Chłopek K.; Bill, E.; Weyhermüller, T.; Wieghardt, K., Molecular and Electronic Structure of Five-Coordinate Complexes of Iron(II/III) Containing o-Diiminobenzosemiquinonate(1−) π Radical Ligands. *Inorg. Chem.* **2005**, 44, 7087–7098.

Coggins, M. K.; Sun, X.; Kwak, Y.; Solomon, E. I.; Rybak-Akimova, E.; Kovacs, J. A., Characterization of Metastable Intermediates Formed in the Reaction between a Mn(II) Complex and Dioxygen, Including a Crystallographic Structure of a Binuclear Mn(III)–Peroxo Species. *J. Am. Chem. Soc.* **2013**, 135, 5631–5640.

Coggins, M. K.; Toledo, S.; Shaffer, E.; Kaminsky, W.; Shearer, J.; Kovacs, J. A., Characterization and Dioxygen Reactivity of a New Series of Coordinatively Unsaturated Thiolate-Ligated Manganese(II) Complexes. *Inorg. Chem.* **2012**, 51, 6633–6644.

Coulter, E. D.; Emerson, J. P.; Kurtz Jr., D. M.; Cabelli, D. E., Superoxide Reactivity of Rubredoxin Oxidoreductase (Desulfoferrodoxin) from Desulfovibrio vulgaris: A Pulse Radiolysis Study. *J. Am. Chem. Soc.* **2000**, 122, 11555–11556.

Cranshaw, T. E., Mössbauer spectroscopy. *J. Phys. E.* **1974**, 7, 497–505.

Dawson, J. H.; Sono, M., Cytochrome P-450 and chloroperoxidase: thiolate-ligated heme enzymes. Spectroscopic determination of their active-site structures and mechanistic implications of thiolate ligation. *Chem. Rev.* **1987**, 87, 1255–1276.

Denisov, I. G.; Mak, P. J.; Makris, T. M.; Sligar, S. G.; Kincaid, J. R., Resonance Raman Characterization of the Peroxo and Hydroperoxo Intermediates in Cytochrome P450. *J. Phys. Chem. A* **2008**, 112, 13172–13179.

Denisov, I. G.; Makris, T. M.; Sligar, S. G.; Schlichting, I., Structure and Chemistry of Cytochrome P450. *Chem. Rev.* **2005**, 105, 2253–2278.

Dey, A.; Jenney, F. E.; Adams, M. W. W.; Johnson, M. K.; Hodgson, K. O.; Hedman, B.; Solomon, E. I., Sulfur K-Edge X-ray Absorption Spectroscopy and Density Functional Theory Calculations on Superoxide Reductase: Role of the Axial Thiolate in Reactivity. *J. Am. Chem. Soc.* **2007**, 129, 12418–12431.

Dey, A.; Jiang, Y.; Ortiz de Montellano, P.; Hodgson, K. O.; Hedman, B.; Solomon, E. I., S K-edge XAS and DFT Calculations on Cytochrome P450: Covalent and Ionic Contributions to the Cysteine-Fe Bond and Their Contribution to Reactivity. *J. Am. Chem. Soc.* **2009**, 131, 7869–7878.

Dey, A.; Okamura, T.; Ueyama, N.; Hedman, B.; Hodgson, K. O.; Solomon, E. I., Sulfur K-Edge XAS and DFT Calculations on P450 Model Complexes: Effects of Hydrogen Bonding on Electronic Structure and Redox Potentials. *J. Am. Chem. Soc.* **2005**, 127, 12046–12053.

Dunlap, B. I.; Connolly, J. W. D.; Sabin, J. R., On some approximations in applications of $X\alpha$ theory. *J. Chem. Phys.* **1979**, 71, 3396–3402.

England, J.; Farquhar, E. R.; Guo, Y.; Cranswick, M. A.; Ray, K.; Münck, E.; Que, L., Characterization of a Tricationic Trigonal Bipyramidal Iron(IV) Cyanide Complex, with a Very High Reduction Potential, and Its Iron(II) and Iron(III) Congeners. *Inorg. Chem.* **2011**, 50, 2885–2896.

Feyereisen, M.; Fitzgerald, G.; Komornicki, A., Use of approximate integrals in ab initio theory. An application in MP2 energy calculations. *Chem. Phys. Lett.* **1993**, *208* (5–6), 359–363.

Fridovich, I., Superoxide radical and superoxide dismutase. *Acc. Chem. Res.* **1972**, 5, 321–326.

Gale, E. M.; Narendrapurapu, B. S.; Simmonett, A. C.; Schaefer, H. F.; Harrop, T. C., Exploring the Effects of H-Bonding in Synthetic Analogues of Nickel Superoxide Dismutase (Ni-SOD): Experimental and Theoretical Implications for Protection of the Ni−SCys Bond. *Inorg. Chem.* **2010**, 49, 7080–7096.

Gehring, A. M.; Mori, I.; Perry, R. D.; Walsh, C. T., The Nonribosomal Peptide Synthetase HMWP2 Forms a Thiazoline Ring during Biogenesis of Yersiniabactin, an Iron-Chelating Virulence Factor of Yersinia pestis. *Biochemistry* **1998**, 37, 11637–11650.

Ghosh, P.; Bill, E.; Weyhermüller, T.; Wieghardt, K., Molecular and Electronic Structures of Iron Complexes Containing N,S-Coordinated, Open-Shell o-Iminothionebenzosemiquinonate(1^-) π Radicals. *J. Am. Chem. Soc.* **2003**, 125, 3967–3979.

Glaser, T.; Hedman, B.; Hodgson, K. O.; Solomon, E. I. Ligand K-Edge X-ray Absorption Spectroscopy: A Direct Probe of Ligand−Metal Covalency. *Acc. Chem. Res.* **2000**, 33, 859–868.

Green, M. T., Evidence for Sulfur-Based Radicals in Thiolate Compound I Intermediates. *J. Am. Chem. Soc.* **1999**, 121, 7939–7940.

Green, M. T., Role of the Axial Ligand in Determining the Spin State of Resting Cytochrome P450. *J. Am. Chem. Soc.* **1998**, 120, 10772–10773.

Green, M. T.; Dawson, J. H.; Gray, H. B., Oxoiron(IV) in Chloroperoxidase Compound II Is Basic: Implications for P450 Chemistry. *Science* **2004**, 304, 1653–1656.

Grimme, S.; Antony, J.; Ehrlich, S.; Krieg, H., A consistent and accurate ab initio parametrization of density functional dispersion correction (DFT-D) for the 94 elements H-Pu. *J. Chem. Phys.* **2010**, 132, 154104–154117.

Grimme, S.; Ehrlich, S.; Goerigk, L., Effect of the damping function in dispersion corrected density functional theory. *J. Comput. Chem.* **2011**, 32, 1456–1465.

Harris, D.; Loew, G.; Waskell, L., Structure and Spectra of Ferrous Dioxygen and Reduced Ferrous Dioxygen Model Cytochrome P450. *J. Am. Chem. Soc.* **1998**, 120, 4308–4318.

Herebian, D.; Bothe, E.; Neese, F.; Weyhermüller, T.; Wieghardt, K., Molecular and Electronic Structures of Bis-(o-diiminobenzosemiquinonato)metal(II) Complexes (Ni, Pd, Pt), Their Monocations and -Anions, and of Dimeric Dications Containing Weak Metal−Metal Bonds. *J. Am. Chem. Soc.* **2003**, 125, 9116–9128.

Holm, R. H.; Kennepohl, P.; Solomon, E. I., Structural and Functional Aspects of Metal Sites in Biology. *Chem. Rev.* **1996**, 96, 2239–2314.

Hoyt, J. M.; Sylvester, K. T.; Semproni, S. P.; Chirik, P. Synthesis and Electronic Structure of Bis(imino)pyridine Iron Metallacyclic Intermediates in Iron-Catalyzed Cyclization Reactions. J. *J. Am. Chem. Soc.* **2013**, 135, 4862–4877.

Huang, Y.-P.; Kassner, R. J. Temperature-Dependent Spin-State Equilibrium in an Azide-Ferric Heme Octapeptide Complex. A Model System for the Spin Equilibria of Ferric Heme Proteins. *J. Am. Chem. Soc.* **1979**, *101*, 5807–5810.

Jackson H. L.; Shoner, S. C.; Rittenberg, D.; Cowen, J. A.; Lovell, S.; Barnhart, D.; Kovacs, J. A., Probing the Influence of Local Coordination Environment on the Properties of Fe-Type Nitrile Hydratase Model Complexes. *Inorg. Chem.* **2001**, 40, 1646–1653.

Jiang, Y.; Widger, L. R.; Kasper, G. D.; Siegler, M. A.; Goldberg, D. P., Iron(II)-Thiolate *S* -Oxygenation by O_2 : Synthetic Models of Cysteine Dioxygenase. *J. Am. Chem. Soc.* **2010**, 132, 12214–12215.

Katona, G.; Carpentier, P.; Nivière, V.; Amara, P.; Adam, V.; Ohana, J.; Tsanov, N.; Bourgeois, D., Raman-Assisted Crystallography Reveals End-On Peroxide Intermediates in a Nonheme Iron Enzyme. *Science* **2007**, 316, 449–453.

Kennepohl, P.; Neese, F.; Schweitzer, D.; Jackson, H. L.; Kovacs, J. A.; Solomon, E. I., Spectroscopy of Non-Heme Iron Thiolate Complexes: Insight into the Electronic Structure of the Low-Spin Active Site of Nitrile Hydratase. *Inorg. Chem.* **2005**, 44, 1826–1836.

Kitagawa, T.; Dey, A.; Lugo-Mas, P.; Benedict, J. B.; Kaminsky, W.; Solomon, E.; Kovacs, J. A., A Functional Model for the Cysteinate-Ligated Non-Heme Iron Enzyme Superoxide Reductase (SOR). *J. Am. Chem. Soc.* **2006**, 128, 14448–14449.

Kitajima, N.; Fujisawa, K.; Fujimoto, C.; Morooka, Y.; Hashimoto, S.; Kitagawa, T.; Toriumi, K.; Tatsumi, K.; Nakamura, A., A new model for dioxygen binding in hemocyanin. Synthesis, characterization, and molecular structure of the.mu.-.eta.2:.eta.2 peroxo dinuclear copper(II) complexes, $[Cu(HB(3,5\text{-}R2pz)_3)]_2(O_2)$ (R = isopropyl and Ph). *J. Am. Chem. Soc.* **1992**, 114, 1277–1291.

King, E. R.; Betley, T. A., Unusual Electronic Structure of First Row Transition Metal Complexes Featuring Redox-Active Dipyrromethane Ligands. *J. Am. Chem. Soc.* **2009**, 131, 14374–14380.

Klamt, A.; Schüürmann, G., COSMO: a new approach to dielectric screening in solvents with explicit expressions for the screening energy and its gradient. *J. Chem. Soc., Perkin Trans. 2* **1993**, 5, 799–805.

Kovacs, J. A., Synthetic Analogues of Cysteinate-Ligated Non-Heme Iron and Non-Corrinoid Cobalt Enzymes. *Chem. Rev.* **2004**, 104, 825–848.

Kovacs, J. A.; Brines, L. M., Understanding How the Thiolate Sulfur Contributes to the Function of the Non-Heme Iron Enzyme Superoxide Reductase. *Acc. Chem. Res.* **2007**, 40, 501–509.

Kovaleva, E. G.; Neibergall, M. B.; Chakrabarty, S.; Lipscomb, J. D., Finding Intermediates in the O_2 Activation Pathways of Non-Heme Iron Oxygenases. *Acc. Chem. Res.* **2007**, 40, 475–483.

Krishnamurthy, D.; Kasper, G. D.; Namuswe, F.; Kerber, W. D.; Narducci Sarjeant, A. A.; Moënne-Loccoz, P.; Goldberg, D. P., A Low-Spin Alkylperoxo−Iron(III) Complex with Weak Fe−O and O−O Bonds: Implications for the Mechanism of Superoxide Reductase. *J. Am. Chem. Soc.* **2006**, 128, 14222–14223.

Kung, I.; Schweitzer, D.; Shearer, J.; Taylor, W. D.; Jackson, H. L.; Lovell, S.; Kovacs, J. A., How Do Oxidized Thiolate Ligands Affect the Electronic and Reactivity Properties of a Nitrile Hydratase Model Compound? *J. Am. Chem. Soc.* **2000**, 122, 8299–8300.

Kumar, D.; Sastry, G. N.; Goldberg, D. P.; de Visser, S. P., Mechanism of S-Oxygenation by a Cysteine Dioxygenase Model Complex. *J. Phys. Chem. A* **2012**, 116, 582–591.

Kurtz Jr., D. M., Microbial Detoxification of Superoxide: The Non-Heme Iron Reductive Paradigm for Combating Oxidative Stress. *Acc. Chem. Res.* **2004**, 37, 902–908.

Kurtz, D. M.; Coulter, E. D., The mechanism(s) of superoxide reduction by superoxide reductases in vitro and in vivo. *J. Biol. Inorg. Chem.* **2002**, 7, 653–658.

Labinger, J. A., Tutorial on Oxidative Addition. *Organometallics* **2015**, 34, 4784–4795.

Leipzig, B. K.; Rees, J. A.; Nyrov, A.; Theisen, R.; Flowers, S. E.; Kaminsky, W.; DeBeer, S.; Kovacs, J. A. *In Preparation*.

Lippard, S. J.; Berg, J. M. *Principles of Bioinorganic Chemistry*. University Science Books: Mill Valley, Ca, 1994

Lu, C. C.; Bill, E.; Weyhermüller, T.; Bothe, E.; Wieghardt, K., The Monoanionic π-Radical Redox State of α-Iminoketones in Bis(ligand)metal Complexes of Nickel and Cobalt. *Inorg. Chem.* **2007**, 46, 7880–7889.

Lu, C. C.; Weyhermüller, T.; Bill, E.; Wieghardt, K., Accessing the Different Redox States of α-Iminopyridines within Cobalt Complexes. *Inorg. Chem.* **2009**, 48, 6055–6064.

Lu, C. C.; Bill, E.; Weyhermüller, T.; Bothe, E.; Wieghardt, K., Neutral Bis(α-iminopyridine)metal Complexes of the First-Row Transition Ions (Cr, Mn, Fe, Co, Ni, Zn) and Their Monocationic Analogues: Mixed Valency Involving a Redox Noninnocent Ligand System. *J. Am. Chem. Soc.* **2008**, 130, 3181–3197.

Lugo-Mas, P.; Dey, A.; Xu, L.; Davin, S. D.; Benedict, J.; Kaminsky, W; Hodgson, K. O.; Hedman, B.; Solomon, E. I.; Kovacs, J. A., How Does Single Oxygen Atom Addition Affect the

Properties of an Fe−Nitrile Hydratase Analogue? The Compensatory Role of the Unmodified Thiolate. *J. Am. Chem. Soc.* **2006**, 128, 11211–11221.

Lugo-Mas, P.; Taylor, W.; Schweitzer, D.; Theisen, R. M.; Xu, L.; Shearer, J.; Swartz, R. D.; Gleaves, M. C.; DiPasquale, A.; Kaminsky, W.; Kovacs, J. A., Properties of Square-Pyramidal Alkyl−Thiolate Fe ^{III} Complexes, Including an Analogue of the Unmodified Form of Nitrile Hydratase. *Inorg. Chem.* **2008**, 47, 11228–11236.

Lundberg, M.; Siegbahn, P. E. M.; Morokuma, K., The Mechanism for Isopenicillin N Synthase from Density-Functional Modeling Highlights the Similarities with Other Enzymes in the 2-His-1-carboxylate Family. *Biochemistry* **2007**, 47, 1031–1042.

Mackay, S.; Edwards, C.; Henderson, A.; Gilmore, C.; Stewart, N.; Shankland, K.; Donald, A., MaXus: a Computer Program for the Solution and Refinement of Crystal Structures from Diffraction Data. University of Glasgow, Scotland 1997.

Magnus, K. A.; Ton-That, H.; Carpenter, J. E., Recent Structural Work on the Oxygen Transport Protein Hemocyanin. *Chem. Rev.* **1994**, 94, 727–735.

Mak, P. J.; Denisov I. G.; Victoria, D.; Makris, T. M.; Deng, T.; Sligar, S. G.; Kincaid, J. R., Resonance Raman Detection of the Hydroperoxo Intermediate in the Cytochrome P450 Enzymatic Cycle. *J. Am. Chem. Soc.* **2007**, 129, 6382–6383.

Mathé, C.; Mattioli, T. A.; Horner, O.; Lombard, M.; Latour, J.; Fontecave, M.; Nivière, V., Identification of Iron(III) Peroxo Species in the Active Site of the Superoxide Reductase SOR from Desulfoarculus baarsii. *J. Am. Chem. Soc.* **2002**, 124, 4966–4967.

McQuilken, A. C.; Jiang, Y.; Siegler, M. A.; Goldberg, D. P., Addition of Dioxygen to an N_4S(thiolate) Iron(II) Cysteine Dioxygenase Model Gives a Structurally Characterized Sulfinato–Iron(II) Complex. *J. Am. Chem. Soc.* **2012**, 134, 8758–8761.

Miethke, M.; Marahiel, M. A., Siderophore-based iron acquisition and pathogen control. *Microbiol. Mol. Biol. Rev.* **2007**, 71, 413–451.

Monfette, S.; Turner, Z. R.; Semproni, S. P.; Chirik, P. J., Enantiopure C_1 -Symmetric Bis(imino)pyridine Cobalt Complexes for Asymmetric Alkene Hydrogenation. *J. Am. Chem. Soc.* **2012**, 134, 4561–4564.

Nam, W., Dioxygen Activation by Metalloenzymes and Models. *Acc. Chem. Res.* **2007**, 40, 465–465.

Namuswe, F.; Hayashi, T.; Jiang, Y.; Kasper, G. D.; Sarjeant, A. A. N.; Moënne-Loccoz, P.; Goldberg, D., Influence of the Nitrogen Donors on Nonheme Iron Models of Superoxide Reductase: High-Spin Fe^{III}−OOR Complexes. P. *J. Am. Chem. Soc.* **2010**, 132, 157–167.

Namuswe, F.; Kasper, G. D.; Sarjeant, A. A. N.; Hayashi, T.; Krest, C. M.; Green, M. T.; Moënne-Loccoz, P.; Goldberg, D. P., Rational Tuning of the Thiolate Donor in Model Complexes of Superoxide Reductase: Direct Evidence for a *trans* Influence in Fe^{III}–OOR Complexes. *J. Am. Chem. Soc.* **2008**, 130, 14189–14200.

Neese, F., The ORCA program system. *Wiley Interdiscip. Rev. Comput. Mol. Sci.* **2012**, *2* (1), 73–78.

Neese, F., Prediction of molecular properties and molecular spectroscopy with density functional theory: From fundamental theory to exchange-coupling. *Coord. Chem. Rev.* **2009**, 253, 526–563.

Neese, F.; Olbrich, G., Efficient use of the resolution of the identity approximation in time-dependent density functional calculations with hybrid density functionals. *Chem. Phys. Lett.* **2002**, 362, 170–178.

Neese, F.; Wennmohs, F.; Hansen, A.; Becker, U., Efficient, approximate and parallel Hartree–Fock and hybrid DFT calculations. A 'chain-of-spheres' algorithm for the Hartree–Fock exchange. *Chem. Phys.* **2009**, 356, 98–109.

Nienkemper, K.; Kotov, V. V.; Kehr, G.; Erker, G.; Fröhlich, R., Chelate [2-(Iminoethyl)pyridineN-oxide]metal Complexes-Synthesis and Structural Comparison with Their Chemically Related 2-(Iminoethyl)pyridine-Derived Systems. *Eur. J. Inorg. Chem.* **2006**, 2006, 366–379.

Ogliaro, F.; de Visser, S. P.; Shaik, S. The 'push' effect of the thiolate ligand in cytochrome P450: a theoretical gauging. *J. Inorg. Biochem.* **2002**, 91, 554–567.

Ortiz de Montellano, P. R., Hydrocarbon Hydroxylation by Cytochrome P450 Enzymes. *Chem. Rev.* **2010**, 110, 932–948.

Perdew, J. P., Density-functional approximation for the correlation energy of the inhomogeneous electron gas. *Phys. Rev. B* **1986**, 33, 8822–8824.

Pettersen, E. F.; Goddard, T. D.; Huang, C. C.; Couch, G. S.; Greenblatt, D. M.; Meng, E. C.; Ferrin, T. E., UCSF Chimera? A visualization system for exploratory research and analysis. *J. Comput. Chem.* **2004**, 25, 1605–1612.

Poulos, T. L.; Finzelsy, B. C.; Gunsalusll, I. C.; Wagner, G. C.; Kraut, J., he 2.6-A Crystal Structure of Pseudomonas putida Cytochrome P-450. *J. Biol. Chem.* **1985**, 260, 16122–16130.

Poulos, T. L.; Finzel, B. C.; Howard, A. J., High-resolution crystal structure of cytochrome P450cam. *J. Mol. Biol.* **1987**, 195, 687–700.

Que, L. *Physical Methods in Bioinorganic Chemistry*; University Science Books: Sausalito, CA, 2000.

Rittle, J.; Green, M. T., Cytochrome P450 Compound I: Capture, Characterization, and C-H Bond Activation Kinetics. *Science* **2010**, 330, 933–937.

Rodrigues, J. V.; Abreu, I. A.; Cabelli, D.; Teixeira, M., Superoxide Reduction Mechanism of Archaeoglobus fulgidus One-Iron Superoxide Reductase. *Biochemistry* **2006**, 45, 9266–9278.

Roelfes, G.; Vrajmasu, V.; Chen, K.; Ho, R. Y. N.; Rohde, J.; Zondervan, C.; la Crois, R. M.; Schudde, E. P.; Lutz, M.; Spek, A. L.; Hage, R.; Feringa, B. L.; Münck, E.; Que Jr. L., End-On and Side-On Peroxo Derivatives of Non-Heme Iron Complexes with Pentadentate Ligands: Models for Putative Intermediates in Biological Iron/Dioxygen Chemistry. *Inorg. Chem.* **2003**, 42, 2639–2653.

Römelt, M.; Ye, S.; Neese, F., Calibration of Modern Density Functional Theory Methods for the Prediction of ^{57}Fe Mössbauer Isomer Shifts: Meta-GGA and Double-Hybrid Functionals. *Inorg. Chem.* **2009**, 48, 784–785.

Rose, K.; Shadle, S. E.; Eidsness, M. K.; Kurtz Jr., D. M.; Scott, R. A.; Hedman, B.; Hodgson, K. O.; Solomon, E. I., Investigation of Iron−Sulfur Covalency in Rubredoxins and a Model System Using Sulfur K-Edge X-ray Absorption Spectroscopy. *J. Am. Chem. Soc.* **1998**, 120, 10743–10747.

Sandy, M.; Butler, A., Microbial Iron Acquisition: Marine and Terrestrial Siderophores. *Chem. Rev.* **2009**, 109, 4580–4595.

Sazama, G. T.; Betley, T. A., Ligand-Centered Redox Activity: Redox Properties of 3d Transition Metal Ions Ligated by the Weak-Field Tris(pyrrolyl)ethane Trianion. *Inorg. Chem.* **2010**, 49, 2512–2524.

Sazama, G. T.; Betley, T. A., Multiple, Disparate Redox Pathways Exhibited by a Tris(pyrrolido)ethane Iron Complex. *Inorg. Chem.* **2014**, 53, 269–281.

Schaefer, B. A.; Margulieux, G. W.; Tiedemann, M. A.; Small, B. L.; Chirik, P. J., Synthesis and Electronic Structure of Iron Borate Betaine Complexes as a Route to Single-Component Iron Ethylene Oligomerization and Polymerization Catalysts. *Organometallics* **2015**, 34, 5615–5623.

Schöneboom, J. C.; Lin, H.; Reuter, N.; Thiel, W.; Cohen, S.; Ogliaro, F.; Shaik, S., The Elusive Oxidant Species of Cytochrome P450 Enzymes: Characterization by Combined Quantum Mechanical/Molecular Mechanical (QM/MM) Calculations. *J. Am. Chem. Soc.* **2002**, 124, 8142–8151.

Shaik, S.; Cohen, S.; Wang, Y.; Chen, H.; Kumar, D.; Thiel, W., P450 Enzymes: Their Structure, Reactivity, and Selectivity—Modeled by QM/MM Calculations. *Chem. Rev.* **2010**, 110, 949–1017.

Shaik, S.; Kumar, D.; de Visser, S. P.; Altun, A.; Thiel W., Theoretical Perspective on the Structure and Mechanism of Cytochrome P450 Enzymes. *Chem. Rev.* **2005**, 105, 2279–2328.

Shearer, J.; Kung, I. Y.; Lovell, S.; Kovacs, J. A., A Co(III) Complex in a Mixed Sulfur/Nitrogen Ligand Environment: Modeling the Substrate- and Product-Bound Forms of the Metalloenzyme Thiocyanate Hydrolase. *Inorg. Chem.* **2000**, 39, 4998–4999.

Shearer, J.; Nehring, J.; Lovell, S.; Kaminsky, W.; Kovacs, J. A., Modeling the Reactivity of Superoxide Reducing Metalloenzymes with a Nitrogen and Sulfur Coordinated Iron Complex. *Inorg. Chem.* **2001**, 40, 5483–5484.

Shearer, J.; Scarrow, R. C.; Kovacs, J. A., Synthetic Models for the Cysteinate-Ligated Non-Heme Iron Enzyme Superoxide Reductase: Observation and Structural Characterization by XAS of an FeIII−OOH Intermediate. *J. Am. Chem. Soc.* **2002**, 124, 11709–11717.

Shejwalkar, P.; Rath, N. P.; Bauer, E. B., New iron(II) α-iminopyridine complexes and their catalytic activity in the oxidation of activated methylene groups and secondary alcohols to ketones. *Dalt. Trans.* **2011**, 40, 7617–7631.

Sheldrick, G. M. CELL_NOW, University of Göttingen, Germany, 2005.

Sheldrick, G. M. SHELXL-97: Program for the Refinement of Crystal Structures, University of Göttingen, Germany, 1997.

Sheldrick, G. M. TWINABS, University of Göttingen, Germany, 1997.

Simaan, A. J.; Döpner, S.; Banse, F.; Bourcier, S.; Bouchoux, G.; Boussac, A.; Hildebrandt, P.; Girerd, J.-J., FeIII-Hydroperoxo and Peroxo Complexes with Aminopyridyl Ligands and the Resonance Raman Spectroscopic Identification of the Fe−O and O−O Stretching Modes. *Eur. J. Inorg. Chem.* **2000**, 2000, 1627–1633.

Sivaramakrishnan, S.; Ouellet, H.; Matsumura, H.; Guan, S.; Moënne-Loccoz, P.; Burlingame, A. L.; Ortiz de Montellano, P. R., Proximal Ligand Electron Donation and Reactivity of the Cytochrome P450 Ferric–Peroxo Anion. *J. Am. Chem. Soc.* **2012**, 134, 6673–6684.

Solomon, E. I.; Szilagyi, R. K.; DeBeer George, S.; Basumallick, L., Electronic Structures of Metal Sites in Proteins and Models: Contributions to Function in Blue Copper Proteins. *Chem. Rev.* **2004**, 104, 419–458.

Stiefel, E. I.; Waters, J. H.; Billig, E.; Gray, H. B., The Myth of Nickel(III) and Nickel(IV) in Planar Complexes. *J. Am. Chem. Soc.* **1965**, 87, 3016–3017.

Stoll, S.; Schweiger, A. EasySpin, a comprehensive software package for spectral simulation and analysis in EPR. *J. Magn. Reson. Ser. A* **2006**, *178* (1), 42–55.

Storr, T.; Verma, P.; Pratt, R. C.; Wasinger, E. C.; Shimazaki, Y.; Stack, T. D. P., Defining the Electronic and Geometric Structure of One-Electron Oxidized Copper−Bis-phenoxide Complexes. *J. Am. Chem. Soc.* **2008**, 130, 15448–15459.

Tamanaha, E.; Zhang, B.; Guo, Y.; Chang, W.; Barr, E. W.; Xing, G.; St. Clair, J.; Ye, S.; Neese, F.; Bollinger, J. M.; Krebs, C., Spectroscopic Evidence for the Two C–H-Cleaving Intermediates of *Aspergillus nidulans* Isopenicillin *N* Synthase. *J. Am. Chem. Soc.* **2016**, 138, 8862–8874.

Theisen, R. M. Synthetic Models and Reactivity of Sulfur-Ligated Iron Metalloenzymes, University of Washington, 2005.

Toledo, S. A. Synthesis and Reactivity of an Expanded Family of Superoxide Reductase (SOR) Model Complexes Using N-Heterocyclic, Thiolate Containing Ligands: Towards a Better Understanding of Structural-Functional Relationships, University of Washington, 2009.

Vedder, C.; Schaper, F.; Brintzinger, H.-H.; Kettunen, M.; Babik, S.; Fink, G., Chiral Iron(II) and Cobalt(II) Complexes with Biphenyl-Bridged Bis(pyridylimine) Ligands-Syntheses, Structures and Reactivities. *Eur. J. Inorg. Chem.* **2005**, 2005, 1071–1080.

Waasmaier, D.; Kirfel, A., New Analytical Scattering Factor Functions for Free Atoms and Ions. *Acta Crystallogr. A.* **1995**, 51, 416–430.

Wada, A.; Ogo, S.; Nagatomo, S.; Kitagawa, T.; Watanabe, Y; Jitsukawa, K.; Masuda, H., Reactivity of Hydroperoxide Bound to a Mononuclear Non-Heme Iron Site. *Inorg. Chem.* **2002**, 41, 616–618.

Widger, L. R.; Davies, C. G.; Yang, T.; Siegler, M. A.; Troeppner, O.; Jameson, G. N. L.; Ivanović-Burmazović, I.; Goldberg, D. P., Dramatically Accelerated Selective Oxygen-Atom Transfer by a Nonheme Iron(IV)-Oxo Complex: Tuning of the First and Second Coordination Spheres. *J. Am. Chem. Soc.* **2014**, 136, 2699–2702.

Widger, L. R.; Jiang, Y.; Siegler, M. A.; Kumar, D.; Latifi, R.; de Visser, S. P.; Jameson, G. N. L.; Goldberg, D. P., Synthesis and Ligand Non-Innocence of Thiolate-Ligated (N_4S) Iron(II) and Nickel(II) Bis(imino)pyridine Complexes. *Inorg. Chem.* **2013**, 52, 10467–10480.

Wu, J. Y.; Moreau, B.; Ritter, T., Iron-Catalyzed 1,4-Hydroboration of 1,3-Dienes. *J. Am. Chem. Soc.* **2009**, 131, 12915–12917.

Wu, J. Y.; Stanzl, B. N.; Ritter, T., A Strategy for the Synthesis of Well-Defined Iron Catalysts and Application to Regioselective Diene Hydrosilylation. *J. Am. Chem. Soc.* **2010**, 132, 13214–13216.

Wüllen, C., Molecular density functional calculations in the regular relativistic approximation: Method, application to coinage metal diatomics, hydrides, fluorides and chlorides, and comparison with first-order relativistic calculations. *J. Chem. Phys.* **1998**, 109, 392–399.

Ye, S.; Bill, E.; Neese, F., Electronic Structures of the $[Fe(N_2)(SiP^{iPr}_3)]^{+1/0/-1}$ Electron Transfer Series: A Counterintuitive Correlation between Isomer Shifts and Oxidation States. *Inorg. Chem.* **2016**, 55, 3468–3474.

Yeh, A. P.; Hu, Y.; Jenney, F. E.; Adams, M. W. W.; Rees, D. C., Structures of the Superoxide Reductase from Pyrococcus furiosus in the Oxidized and Reduced States. *Biochemistry* **2000**, 39, 2499–2508.

Yoshioka, S.; Takahashi, S.; Ishimori, K.; Morishima, I., Roles of the axial push effect in cytochrome P450cam studied with the site-directed mutagenesis at the heme proximal site. *J. Inorg. Biochem.* **2000**, 81, 141–151.